Fall 2019

Characterization of a green electric solid propellant for electric propulsion

Matthew Scott Glascock

Department: Mechanical and Aerospace Engineering

Recommended Citation

Glascock, Matthew Scott, "Characterization of a green electric solid propellant for electric propulsion" (2019). *Doctoral Dissertations*. 2830.
https://scholarsmine.mst.edu/doctoral_dissertations/2830

CHARACTERIZATION OF A GREEN ELECTRIC SOLID PROPELLANT FOR ELECTRIC PROPULSION

by

MATTHEW SCOTT GLASCOCK

A DISSERTATION

Presented to the Faculty of the Graduate School of the

MISSOURI UNIVERSITY OF SCIENCE AND TECHNOLOGY

In Partial Fulfillment of the Requirements for the Degree

DOCTOR OF PHILOSOPHY

in

AEROSPACE ENGINEERING

2019

Approved by:

Dr. Henry Pernicka, Advisor
Dr. Joshua Rovey
Dr. Kurt Polzin
Dr. David Riggins
Dr. Carlos Castaño

PUBLICATION DISSERTATION OPTION

This dissertation consists of the following three articles, formatted in the style used by the Missouri University of Science and Technology:

Paper I: Pages 8-44 is published by the AIAA Journal of Propulsion and Power. Submitted 01/15/2019, revised 05/09/2019, accepted 05/18/2019, online 06/25/2019.

Paper II: Pages 45-72 have been submitted to the AIAA Journal of Thermophysics and Heat Transfer. Submitted 09/29/2019, in review.

Paper III: Pages 73-106 are intended for submission to the AIAA Journal of Propulsion and Power. In preparation.

Paper IV: Pages 107-131 are intended for submission to the AIAA Journal of Propulsion and Power. In preparation.

ABSTRACT

Electric solid propellants are advanced solid chemical rocket propellants that can be controlled (ignited, throttled and extinguished) through the application and removal of an electric current. These propellants are also being considered for use in ablative pulsed plasma thruster and multimode systems. In this work, the behavior and performance of a novel green electric solid propellant operating in an electrothermal ablation-fed pulsed plasma thruster was investigated. Using an inverted pendulum micro-Newton thrust stand, the impulse bit and specific impulse of the device using the electric solid propellant were measured for short-duration and long-duration runs to end-of-life, at energy levels of 5, 10, 15 and 20 J. Also, the device was operated using the current state-of-the-art ablation-fed pulsed plasma thruster propellant, polytetrafluoroethylene or PTFE. Impulse bit measurements for PTFE indicate 100 μN-s at an initial energy level of 5 J, which increases linearly by ~30 μN-s/J with initial energy. Measurements of the impulse bit for the electric solid propellant are on average lower than PTFE by about 5%. Further, it is shown that absorbed water in the hygroscopic electric solid propellant evaporates rapidly during early discharges of the device. This mass loss artificially decreased specific impulse relative to traditional propellant. Removing this evaporated mass from the ablation mass loss measurements, the corrected specific impulse of the propellant is 300 s compared to 450 s for PTFE. The electric solid propellant shows some promise for future multimode application but is currently limited in electric propulsion application by poor ablation efficiency and the absorption of atmospheric water.

ACKNOWLEDGMENTS

Dr. Pernicka, you have positively influenced and taught me in more ways than you know, many of which are not related to the academic world. I deeply appreciate your willingness to take over in the wake of Dr. Rovey's departure from the university. Yes, readers, my advisor left me in the middle of my research. Dr. Rovey, I am eternally grateful for the support you showed me in that time, and for making the process quite positive in the end. Drs. Riggins and Castaño, you taught me much in our time and courses together, fueled my passion for research, and greatly improved the quality of the final product. Kurt, I will forever appreciate our summers spent in the damp heat of Huntsville, and the many fruitful discussions we have shared, and will continue to share.

My eternal thanks are due to the NSTRF program, which funded me through most of my graduate career. Additionally, the folks at DSSP were especially helpful with my research, and I was lucky to spend a wonderful summer working there.

To my wife, Katie, I'm sorry I moved you from our hometown to the middle of the frozen plains of Illinois. Without you, I may never have had been able to surmount the pressure of this journey. To my mother, thank you for shamelessly bragging about me to anyone who will listen, and forever supporting me fully in all that I have done. Matt Gualdoni, our years as roomates will never be forgotten, and our friendship is eternal. Thanks are due to the friends made in college, and those who lingered from home; our annual St. Pat's release was much needed. My family, you collectively gave me the strength to shoulder all these years of hard work, and I love you all for it. I thank my colleagues in the AP and EP Labs, for enduring my ramblings and providing discussion.

TABLE OF CONTENTS

Page

PUBLICATION DISSERTATION OPTION iii

ABSTRACT... iv

ACKNOWLEDGMENTS v

LIST OF ILLUSTRATIONS...x

LIST OF TABLES xiii

NOMENCLATURE xiv

SECTION

1. INTRODUCTION.. 1

1.1. ELECTRIC SPACECRAFT PROPULSION 2

1.2. PULSED PLASMA THRUSTER 3

1.3. ELECTRIC SOLID PROPELLANTS.. 4

2. MOTIVATION 6

PAPER

I. ELECTRIC SOLID PROPELLANT ABLATION IN AN ARC DISCHARGE........ 8

ABSTRACT... 8

1. INTRODUCTION.. 9

2. EXPERIMENTAL 13

2.1. VACUUM FACILITY AND MASS BALANCE... 13

2.2. HIGH PERFORMANCE ELECTRIC PROPELLANT 14

2.3. PROPELLANT SAMPLE PREPARATION 16

2.4. TEST ARTICLE.. 18

2.5. ELECTRICAL SETUP 19

3. LCR CIRCUIT MODEL 21

4. RESULTS 23

4.1. HIPEP MOISTURE CONTENT 23

4.2. ABLATION MASS LOSS 25

4.3. DISCHARGE CURRENT 29

5. ANALYSIS AND DISCUSSION 31

5.1. LCR CIRCUIT MODEL 31

5.2. ABLATION ENERGY BALANCE 35

6. CONCLUSIONS 38

ACKNOWLEDGMENTS 40

REFERENCES 40

II. THERMODYNAMIC PROPERTIES OF HYDROXYLAMMONIUM NITRATE-BASED ELECTRIC SOLID PROPELLANT PLASMA 45

ABSTRACT 45

1. INTRODUCTION 46

2. MATHEMATICAL MODELS 48

2.1. EQUILIBRIUM COMPOSITION 49

2.2. THERMODYNAMIC PROPERTIES 52

2.3. PROPELLANT COMPOSITION 53

3. MODEL VALIDATION 55

3.1. THERMAL DEGRADATION TEMPERATURE 56

3.2. CHEMICAL COMPOSITION OF PTFE VAPOR 60

3.3. LOW TEMPERATURE HIPEP COMBUSTION 62

4. RESULTS AND DISCUSSION 63
    4.1. CHEMICAL COMPOSITION OF HIPEP VAPOR 63
    4.2. THERMODYNAMIC PROPERTIES 65
5. CONCLUSIONS 68
ACKNOWLEDGEMENTS 70
REFERENCES 70
III. IMPULSE MEASUREMENTS OF ELECTRIC SOLID PROPELLANT IN AN ELECTROTHERMAL ABLATION-FED PULSED PLASMA THRUSTER 73
ABSTRACT 73
1. INTRODUCTION 74
2. EXPERIMENTAL METHODS AND APPARATUS 79
    2.1. HIGH PERFORMANCE ELECTRIC PROPELLANT 79
    2.2. ELECTRIC PROPELLANT THRUSTER EXPERIMENT 80
    2.3. COMPACT THRUST STAND 82
3. RESULTS 87
    3.1. SHORT-DURATION TESTS 87
    3.2. LONG-DURATION TESTS 91
4. ANALYSIS AND DISCUSSION 95
    4.1. SPECIFIC IMPULSE 95
    4.2. PROPELLANT SAMPLE LIFETIME 98
    4.3. THRUST MODE 100
5. CONCLUSIONS 102
ACKNOWLEDGMENTS 103

REFERENCES 103

IV. SPECIFIC IMPULSE OF ELECTRIC SOLID PROPELLANT IN AN ELECTROTHERMAL ABLATION-FED PULSED PLASMA THRUSTER ... 107

ABSTRACT 107

1. INTRODUCTION 108

2. EXPERIMENTAL APPARATUS 113

2.1. HIGH PERFORMANCE ELECTRIC PROPELLANT 113

2.2. COMPACT THRUST STAND 114

2.3. ELECTRIC PROPELLANT THRUSTER EXPERIMENT 115

3. EXPERIMENTAL APPROACH 117

4. RESULTS 120

5. ANALYSIS AND DISCUSSION 122

6. CONCLUSION 126

ACKNOWLEDGMENTS 128

REFERENCES 128

SECTION

3. CONCLUSIONS AND RECOMMENDATIONS 132

3.1. CONCLUSIONS 132

3.2. RECOMMENDATIONS 133

BIBLIOGRAPHY 136

VITA 138

LIST OF ILLUSTRATIONS

PAPER I Page

Figure 1: Photograph of PTFE (left) and HIPEP (right) propellant samples used in the test article. 14

Figure 2: Diagram of the coaxial pulsed plasma discharge chamber test article. 18

Figure 3: Circuit diagram for the pulsed plasma discharge chamber test article. 20

Figure 4: Ideal inductance-capacitance-resistance series circuit. 21

Figure 5: a.) Sample mass evolution for three HIPEP samples and b.) percent mass lost during pre-test drying of six HIPEP samples. 24

Figure 6: Specific ablation of PTFE and HIPEP materials for 5, 10, 15, and 20 J nominal initial energy. 28

Figure 7: Discharge and LCR circuit model current for a.) PTFE and b.) HIPEP, both at a nominal 15 J initial energy. 30

PAPER II

Figure 1: Thermogravimetric analysis curves for samples of a.) PTFE and b.) HIPEP. .. 58

Figure 2: Equilibrium composition of PTFE vapor at 1 bar pressure as a function of temperature organized by a.) polyatomic and b.) atomic/ionic species 61

Figure 3: Equilibrium composition of HIPEP vapor at 1 bar pressure as a function of temperature organized by a.) polyatomic and b.) atomic/ionic species 64

Figure 4: Mixture enthalpy of HIPEP and PTFE vapors as a function of equilibrium temperature. 66

Figure 5: Specific heat at constant pressure of HIPEP and PTFE vapors as a function of equilibrium temperature. 67

PAPER III

Figure 1: Diagram of the electric propellant thruster experiment. 81

Figure 2: Diagram of the inverted-pendulum design UIUC Compact Thrust Stand. 84

Figure 3: Typical pre-test thrust stand response calibration data as a function of applied impulse bit (bottom) and corresponding standardized residuals for the response data (top). 85

Figure 4: Impulse bit measurements for short-duration tests with both propellants and for a.) 5 J, b.) 10 J, c.) 15 J, and d.) 20 J nominal initial energy. 89

Figure 5: Average impulse bit over all short-duration tests at each initial energy for each propellant (error bars are a 2-σ standard deviation). 90

Figure 6: Impulse measurements for long-duration tests with a.) PTFE and b.) HIPEP propellant. 92

Figure 7: Average impulse bit per joule from the long-duration testing plotted as a function of total pulses. 93

Figure 8: Specific impulse as a function of energy for each short-duration test for each propellant. 96

PAPER IV

Figure 1: Diagram of the electric propellant thruster experiment. 116

Figure 2: Summary of results from ref. [31]. 117

Figure 3: Specific impulse over short-duration trials, both raw and corrected for excess early mass loss. 124

Figure 4: Specific impulse as a function of test duration, both raw values and corrected values. 125

LIST OF TABLES

PAPER I Page

Table 1: Chemical composition of the High Performance Electric Propellant (HIPEP).. 16

Table 2: Ablation mass loss measurements for PTFE and HIPEP. 27

Table 3: Discharge current characteristics for PTFE and HIPEP. 30

Table 4: LCR circuit model analysis results. 34

PAPER II

Table 1: Selected model constituent species and mass fractions for each propellant....... 54

Table 2: Onset and degradation temperature from thermogravimetric analysis.............. 59

Table 3: Comparison of predicted HIPEP composition at 700 K for two thermochemical models. 62

PAPER IV

Table 1: Ablation mass loss for short- and very-short-duration tests trials. 121

NOMENCLATURE

Symbol	Description
V_0	Initial capacitor voltage
C	Capacitance
$I(t)$	Time-varying current
$L(t)$	Time-varying inductance
$R(t)$	Tim-varying resistance
L_0	Initial circuit inductance
R_0	Initial circuit resistance
Q	Time-varying charge
P	Period of circuit oscillation
E	Energy dissipated by arc discharge
$P(t)$	Time-varying instantaneous electrical power
$I_{EXP}(t)$	Time-varying experimentally measured current
$R_p(t)$	Time-varying plasma resistance
R_{elec}	Resistance of electrodes
R_1	Slope of linear resistance increase

1. INTRODUCTION

This dissertation presents work on the characterization of a novel electric solid propellant for applications to electric and multimode spacecraft propulsion. Electric solid propellants are unique solid chemical rocket propellants in that ignition and continued combustion arises only from applied electric power. Specifically, this work investigates the physical processes, behavior, and performance of this propellant during operation in a coaxial ablation-fed pulsed plasma thruster. In subsequent pages, the reader is first presented with a light review of the previous research and history of electric propulsion, the pulsed plasma thruster, and electric solid propellants. Then, the relevance of this work to those foundational concepts is covered.

In the main body of this dissertation, four papers accepted or intended for publication in peer-reviewed journals are presented. These papers describe in detail the investigative numerical study and experiments used to characterize the HIPEP material in an APPT. Paper I presents results of an experiment designed to better understand the fundamental process of HIPEP ablation in arc discharges. Measurements of the ablation mass loss are taken alongside PTFE using an identical setup to benchmark the HIPEP material. In Paper II a basic thermochemical model of HIPEP vapor is developed for the high temperatures expected in ablation-fed arc discharges. Paper III presents an important performance study comparing impulse measurements of both HIPEP and PTFE operating in an electrothermal APPT. During the impulse measurements a specific behavior was noted in early portions of test runs that led to the final experiment. In Paper IV, impulse and mass loss measurements from early pulses of the APPT are presented along with discussion of the impact on specific impulse calculations.

In the final section of this dissertation, the main conclusions from the body of work consisting of the previous papers will be summarized. Additionally, an evaluation of the overall state of research on the electric solid propellant will be presented. Finally, the reader will find some recommendations for future research efforts in this area.

1.1. ELECTRIC SPACECRAFT PROPULSION

Vehicles of all size and purpose rely on Newton’s Third Law to propel objects or people through their designed environment. Those vehicles confined to the free-fall vacuum environment of outer space, or spacecraft, have perhaps the most challenging path to this propulsion. With no surrounding solid surface or fluid to exert force on, spacecraft must carry their own mass for the sole purpose of later ejection and subsequent propulsion in the desired direction. Now, while simply dumping this propellant mass out of one end of the spacecraft would achieve the desired effect, in practice it is much more efficient to accelerate that mass to high velocities. This acceleration requires energy. Historically, spacecraft obtain this energy from one of two sources. Chemical propulsion technologies harness energy released from chemical reactions between atoms and molecules. Often this energy is thermally transferred to the propellant which is expelled at some velocity. Electric propulsion technologies utilize electrical energy stored or generated on-board the spacecraft. That energy may be used to thermally, statically, or electromagnetically add energy to the propellant. While chemical energy requires the consumption of the propellant mass, electric energy may be provided independently and in large quantities by solar panels or reactors. Further, the propellant exhaust velocities obtainable with electric propulsion are often much higher than possible with chemical propulsion.

1.2. PULSED PLASMA THRUSTER

One of the earliest electric propulsion technologies was the pulsed plasma thruster. In fact, six pulsed plasma thrusters were flown on-board the Soviet space probe Zond 2 in 1964, marking the first orbital spaceflight of an electric propulsion device [1]. The pulsed plasma thruster, or PPT, operates on one major principal: the arc discharge. Arc discharges are formed when the medium separating two conductors at a large voltage difference suddenly allows for current to flow between said conductors. Typically this current is extremely high, and the discharge is very short in duration, as seen in lightning strikes, a type of arc discharge. PPTs store electrical energy on high-voltage capacitors until an arc discharge is triggered at the desired location. Gas-fed PPTs incite this arc in gaseous propellant fed into an arc discharge region between high-voltage electrodes. More commonly, however, the arc discharge created between the electrodes is intentionally adjacent to solid propellant. During the arc discharge the propellant wall is heated to extreme temperatures, causing ablation of the solid into the arc. These ablation-fed PPTs, or APPTs, often use polytetraflouroethylene (PTFE), more commonly known by the trade name Teflon, as propellant. Solid PTFE is easily stored and launched on a spacecraft because no propellant tanks or lines are needed, and it is inert. Moreover, the performance of PTFE in APPTs is quite good, and it is held as the state-of-the-art. Because the stored energy is electrical in nature, PPTs offer higher propellant exhaust velocities than can be achieved using chemical propulsion, but typically only in short bursts of very small thrust. As such, PPTs fulfill secondary propulsion needs on spacecraft such as station-keeping and attitude control [2]. However, PPTs have been considered for main propulsion of small spacecraft due to their rise in popularity in recent years [3].

1.3. ELECTRIC SOLID PROPELLANTS

Electric solid propellants are advanced solid rocket propellants that are safe, throttleable, and green with on-demand on-off capability. These electric solid propellants (ESP's) ignite and decompose when electric power is applied at sufficient current and voltage [4]. This decomposition is a highly exothermic process that generates hot gas at a burn rate that can be throttled by varying the applied current. Removal of the voltage and current extinguishes the reaction, which may be restarted by reapplication of electric power [5]. Because this reaction is only induced by electric current, ESPs are not susceptible to accidental ignition by spark, impact or open flame. These characteristics are extremely beneficial compared to traditional solid rocket propellants which are not throttleable, toggleable, or insensitive to external ignition sources. The advent of ESPs expands the potential applications for solid propellants that were previously infeasible. Development of ESPs began in the 1990's with the design of an automobile air bag inflator propellant (ABIP) using materials safe for unprotected human contact (i.e., "green" materials). This ABIP was ammonium nitrate-based and was later repurposed for use in other areas, including rocket propulsion. Shortly thereafter, "ASPEN," the first digitally controlled extinguishable solid propellant, was developed [6]. This propellant featured additives with the ammonium nitrate base to lower melting point and increase electrical conductivity [5]. This material exhibited performance metrics comparable to that of previous solid rocket propellants, but major problems existed with the repeatability of ignition. Further development for gas-generation applications led to a special family of electrically controlled energetic materials which may be mixed as either solid, liquid or gel form propellants, all of which are electrically ignitable [7, 8]. Some mixtures are flame-sensitive and explosive, some insensitive to flame and sustainable, some are insensitive and extinguishable (these are ESPs). One particular formula which conducts electricity and exhibits high specific impulse is known as the high performance electric propellant, or HIPEP [4, 9], which is the main focus in this work. In this solid energetic material, the ionic liquid oxidizer hydroxyl-ammonium nitrate (HAN) is dissolved and cross-linked in polyvinyl alcohol (PVA), forming a gel that is hardened by baking. HIPEP exhibits a pyroelectric behavior unique to energetics. When direct current electric power is applied, the level of nitric acid rapidly rises in the material eventually triggering ignition.

2. MOTIVATION

Recently emerging in the spacecraft propulsion world is a method known as multimode propulsion. Multimode propulsion integrates two or more propulsive modes (e.g. chemical and electric) into a system while sharing a single propellant between these modes [10]. Multimode propulsion can potentially provide flexibility and adaptability to spacecraft of all sizes previously unachievable. In certain mission profiles, multimode propulsion can even provide propellant mass savings compared to previous, single-mode technologies.

HIPEP's unique pyroelectric behavior may facilitate a multimode propulsion system using the solid propellant. The first mode is a high thrust chemical mode where direct current electric power is applied to incite pyroelectric gas generation. This propellant is gas-dynamically accelerated through a nozzle to generate thrust like any typical solid rocket motor. The duration of each chemical mode fire is determined by the duration that electric power is supplied. The inventors of this propellant and collaborating groups have reported on this mode of operation previously, with some ongoing efforts [11-13]. Thrusters utilizing ESPs with similar formulations to HIPEP have been demonstrated in this solid rocket motor configuration, with maximum pulse duration 500 ms and specific impulse of 200 seconds [14]. This solid rocket motor may be paired with a second, high specific impulse (I_{sp}) electric mode in the same device using the same thruster hardware and solid propellant with a second electrical circuit configuration. A promising electric mode configuration for HIPEP is the coaxial APPT. Coaxial APPTs and solid rocket motors can be designed with similar tradeoffs with respect to propellant grain and nozzle geometry. Thus, this combination of modes favors multimode system design.

A multimode device utilizing HIPEP in a solid chemical rocket motor mode combined with an electric coaxial APPT mode remains conceptual. Research in the use of HIPEP and other ESPs for gas-generation and chemical mode applications with long (>1 ms) timescales is ongoing and separate from the present work. Because very little has been done in this area prior to the present work, a number of questions yet remain on the behavior of HIPEP in an APPT. As such, we arrive at the primary motivation for the present dissertation. This work focuses on understanding the physical phenomena and performance of the HIPEP material in the proposed APPT electric mode. Performance and ablation mass measurements for HIPEP in an APPT combined with thermochemical modeling of HIPEP vapor help elucidate the physical processes in the material. Once these processes are understood, the community may better assess future application of HIPEP in multimode or electric propulsion devices.

PAPER

I. ELECTRIC SOLID PROPELLANT ABLATION IN AN ARC DISCHARGE

Matthew S. Glascock

Missouri University of Science and Technology, Rolla, MO 65409

Joshua L. Rovey

University of Illinois Urbana-Champaign, Urbana, IL 61801

and

Kurt A. Polzin

NASA Marshall Space Flight Center, Huntsville, AL 35812

ABSTRACT

Electric solid propellants are advanced solid chemical rocket propellants that can be controlled (ignited, throttled and extinguished) through the application and removal of an electric current. Electric solid propellants are also being considered for pulsed arc ablation electric thrusters, such as the pulsed plasma thruster. The focus of this work is the electrical and ablation characteristics of electric solid propellant within an arc discharge. Arc discharges of 5-20 J per pulse were created within a cylindrical cavity and results for the electric solid propellant are compared with polytetrafluoroethylene (PTFE), which is a traditional propellant in ablative pulsed plasma thrusters. The data indicate that the electric solid propellant has higher specific ablation per pulse (14.8 μg/J) relative to PTFE (7.2 μg/J), which quantitatively agrees with an ablation energy balance model. For both propellants, the equivalent circuit resistance and inductance of the plasma arc are 50 mΩ

and 125 nH, respectively. Analyses are presented indicating that the physics of propellant ablation is similar for both propellants with the differences in the observed specific ablation owing to differences in the thermal transport properties between propellants.

1. INTRODUCTION

Recent innovations in the solid rocket propellant field have led to the development of a solid propellant that is safe, throttleable, and green with at-will on-off capability. These electric solid propellants (ESP's) ignite and decompose when electric power is applied at sufficient current and voltage [1]. This decomposition is a highly exothermic process that generates hot gas at a burn rate that can be throttled by varying the applied current. Removal of the voltage and current extinguishes the reaction, which may be restarted by reapplication of electric power [2]. Because this reaction is only induced by electric current, ESPs are not susceptible to accidental ignition by spark, impact or open flame. These characteristics are extremely beneficial compared to traditional solid rocket propellants which are not throttleable, toggleable, or insensitive to external ignition. The advent of ESPs expands the potential applications for solid propellants that were previously infeasible.

Development of ESPs began in the 1990's with the design of an automobile air bag inflator propellant (ABIP) using materials safe for unprotected human contact (i.e. "green" materials). This ABIP was ammonium nitrate-based and was later repurposed for use in other areas, including rocket propulsion. Shortly thereafter, "ASPEN," the first digitally controlled extinguishable solid propellant, was developed [3]. This propellant featured additives with the ammonium nitrate base to lower melting point and increase electrical conductivity [2]. This material exhibited performance metrics comparable to that of previous solid rocket propellants, but major problems existed with the repeatability of ignition. Further development for gas-generation applications led to a special family of electrically controlled energetic materials which may be mixed as either solid, liquid or gel form propellants, all of which are electrically ignitable [4, 5]. Some mixtures are flame-sensitive and explosive, some insensitive to flame and sustainable, some are insensitive and extinguishable (ESPs). One particular formula with high specific impulse and electrical conductivity is known as the high performance electric propellant, or HIPEP [1, 6], which is not sensitive to open flame, spark or impact and is extinguishable. In this solid energetic material, the ionic liquid oxidizer hydroxyl-ammonium nitrate (HAN) is dissolved and cross-linked in polyvinyl alcohol (PVA), forming a gel that is hardened by baking. The resulting rubbery solid HIPEP exhibits a pyroelectric behavior unique to energetics. When direct current electric power is applied, the proton transfer reaction between hydroxyl-ammonium and nitrate is promoted, and the level of nitric acid rapidly rises in the material eventually triggering ignition of the propellant. This exothermic, gas-generating reaction may be harnessed in a solid rocket motor to generate thrust on demand using electric power.

HIPEP's pyroelectric behavior may facilitate a dual-mode propulsion system using the solid propellant. The first mode is a high thrust chemical mode where direct current electric power is applied to incite pyroelectric gas generation. This gas is accelerated gas-dynamically through a nozzle to generate thrust like in a typical solid rocket motor. The duration of each chemical mode fire is determined by the duration that electric power is supplied and could be ~500 milliseconds. The inventors of this propellant and collaborating groups have reported on this mode of operation previously, with some ongoing efforts [7-9]. This solid rocket motor is then paired with a second, high specific impulse (I_{sp}) electric mode, in the same device using the same thruster and solid propellant with a second circuit configuration. One promising electric mode configuration for this concept is a pulsed electric propulsion device known as the coaxial ablation-fed pulsed plasma thruster (APPT).

Pulsed plasma thrusters [10] (PPTs) have been in use since the first orbital flight of an electric propulsion device in 1964. PPTs offer repeatable impulse bits with higher exhaust velocities than can be achieved using chemical thrusters. Ablating PTFE in the discharge to yield a working fluid, APPT's have the added benefit of inert propellant storage with no pressure vessel requirements. PPT's typically fulfill secondary propulsion needs on spacecraft such as station-keeping and attitude control, but have recently garnered more attention as main propulsion for small spacecraft [11, 12]. Broadly, PPT's may be classified as either rectangular or coaxial geometry [10]. Coaxial geometry APPT's, like that of the PPT-4 [13], electrothermal PPT [14-18], or ablative z-pinch PPT [19], begin with a central and a downstream electrode and may have a conical-shape between the electrodes. The central or upstream electrode is typically cylindrical and positively charged (anode) while the downstream electrode is ring-shaped. Solid propellant fills the space between electrodes and may be fed from the side through the conical dielectric. Most commonly this solid propellant is the inert polymer, PTFE, which is held as the state-of-the-art for APPTs. A capacitor or bank of capacitors is charged to a few kilovolts, with that voltage applied across the electrodes. The main arc discharge is initiated by an igniter, which is always located in or near the cathode in a PPT. The igniter generates a surface flashover discharge to create a seed plasma, initiating the main arc discharge. Radiation from this high temperature arc discharge heats the surface of the solid propellant, causing ablation of gaseous propellant species, further fueling the arc. The coaxial PPT is a device dominated by electrothermal acceleration mechanisms, with the energy of the arc heating the gas to yield high exit velocities through gas-dynamic acceleration. Ablation processes are at the core of APPT operation, and thus many studies on the ablation of PTFE exist in literature [20-25].

The aforementioned dual-mode device combining a solid chemical rocket motor mode with an electric coaxial APPT mode remains conceptual. Research in the use of HIPEP and other ESPs for gas-generation and chemical mode applications with long (>1 ms) timescales is ongoing and separate from the present work. Current efforts by the authors are focused on understanding the behavior of the HIPEP material in the proposed APPT electric mode. To date, HIPEP has not been used in a traditional APPT configuration, where propellant material is ablated during a high current, short duration (~10 μs) arc discharge. Another ESP, the ammonium nitrate-based ABIP, was previously tested in Aerojet's modular test unit (MTU) and reported impulse bits were roughly 50-80% of the polytetrafluoroethylene (PTFE) solid propellant typically used in this unit [1]. No performance (impulse/thrust, specific impulse) metrics are yet available for a PPT using HIPEP as propellant. Further, the nuances of HIPEP ablation in an APPT are not yet understood. Specifically, it is not known if the pyroelectric behavior of HIPEP plays a role in ablation of the propellant during the short duration pulse, or if the fundamental physics of propellant ablation from the solid surface remain similar to the inert propellant, PTFE. The objective of this work is to quantify the ablation mass and characterize the ablation process of the HIPEP material relative to that of PTFE in an ablation-fed arc discharge. A pulsed electric arc discharge device was designed to permit quantification of the propellant specific ablation and used with both PTFE and HIPEP. For each propellant, the device was operated for 100 pulses in vacuum, with the initial and final propellant masses recorded to calculate the average ablated mass loss per pulse. Further analysis of the ablation process using an electrical circuit and energy balance model provides comparison of the behavior of the two propellants in an arc discharge.

2. EXPERIMENTAL

We proceed with a discussion of the experimental hardware used in this work. Details are given on the vacuum facility where testing was conducted, the mass balance used for mass loss measurements, the chemical composition of the tested ESP, and the propellant preparation procedures. Finally, we describe the arc discharge test article and its associated electrical circuit.

2.1. VACUUM FACILITY AND MASS BALANCE

The space and high-altitude vacuum facility in the Aerospace Plasma Lab was used to conduct the tests in the present work. The facility has a cylindrical test volume measuring about 6 ft (1.8 m) in diameter and 10 ft (3 m) in length. Four 89-cm-diameter oil vapor diffusion pumps are the primary vacuum pumps and are backed by a Tokuda KP-7500BG rotary-vane pump and an Edwards EH 4200 roots blower. The diffusion pumps are operated independently and with a single pump running (as was done during this work) the nominal base pressure is 2.5×10^{-5} torr.

A Sartorius QUINTIX125D-1S dual range semi-micro balance was used to measure the mass of propellant samples before and after testing. In the selected range, this balance has a capacity of 60 g and can be read down to 0.01 mg. The factory reported repeatability of the balance is 0.02 mg. For measurements reported here the typical variation in measurement was ±0.03 mg. The balance was used inside a nitrogen-purged glovebox to maintain the relative humidity at less than 11% while performing mass measurements.

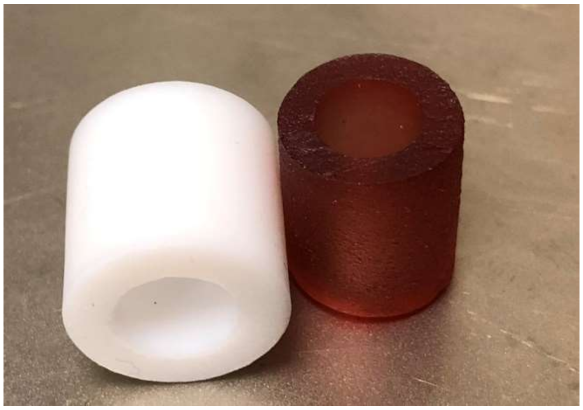

Figure 1: Photograph of PTFE (left) and HIPEP (right) propellant samples used in the test article.

2.2. HIGH PERFORMANCE ELECTRIC PROPELLANT

HIPEP is a HAN-based solution solid manufactured by Digital Solid State Propulsion (DSSP) using “green” ingredients and processes free of harmful fumes. It is mixed in standard chemical glassware, with only gloves and safety glasses needed for protection, and cured at room temperature (35°C/95°F). HIPEP has a chemical composition of primarily HAN oxidizer (an inorganic ionic liquid) and polyvinyl alcohol

(PVA) fuel binder, which comprise 95% of the propellant. It is initially a liquid and poured into a mold, curing to form a rubbery solid with density ~1.8 g/cm^3 and the appearance and texture of a soft pencil eraser.

There are some key differences between HIPEP and traditional PTFE PPT propellant. A photograph comparing the appearance of each propellant is shown in Figure 1. PTFE is an inert, fluorocarbon solid, while HIPEP is an energetic solid mixture with composition given in Table 1. In a typical PPT, the PTFE propellant is an electrical insulator between the electrodes. The conductivity of HIPEP (1-2 S/m) is comparable to highly conductive ionic liquids or saline water at room temperature. Solid PTFE does not conduct electricity (10^{-23} S/m) and when an arc discharge is initiated near the solid surface it ablates the propellant via heat transfer. A pulsed electric current near the surface of HIPEP could operate in much the same manner, but it could also potentially be conducted through the solid propellant, initiating pyroelectric decomposition and formation of intermediaries in the propellant. As of this writing, it is unclear if the pyroelectric nature of HIPEP plays a role in the evolution of vapor from the solid surface, or if the standard ablation-fed arc mechanisms are dominant like in PTFE fueled ablation-fed arcs. Further, it is unclear if or how these differences affect the operation and performance of an APPT fueled by HIPEP (or similar ESPs). More discussion of this topic related to the results presented here is found in Section 5.2.

Table 1: Chemical composition of the High Performance Electric Propellant (HIPEP).

Chemical Name	Chemical Formula	Percentage by mass	Molecular Mass, g/mol
Hydroxyl Ammonium Nitrate (HAN)	$(NH_3OH)^+ NO_3^-$	75%	96
Polyvinyl Alcohol (PVA)	$CH_2CH(OH)$	20%	44
Ammonium Nitrate (AN)	NH_4NO_3	5%	80

2.3. PROPELLANT SAMPLE PREPARATION

In the present work, the HIPEP was received from the manufacturer in the form of propellant slugs that were all cured from a single batch of mixed liquid propellant poured into shaped plastic molds. This process produced five slugs of annular shape measuring 40 mm in length, ~12 mm outer diameter, and ~6 mm inner diameter, which are designated slug 1, 2, etc. Each slug is then cut into three pieces of 12 mm length (further designated as 1a, 1b, etc.) as needed for the test article as described in Section 2.4. This process yielded 15 fresh pieces with approximate mass of 1 g, which were then tested in the ablation test article. Henceforth, these smaller pieces are referred to individually as simply propellant samples.

The primary constituent of HIPEP is HAN, which is known to by hygroscopic. This behavior is reflected in the HIPEP formulation. Solid HIPEP will gradually absorb moisture from the atmosphere until the material becomes completely liquid. This can be a concern for future spacecraft, which may be sitting at atmospheric conditions for long periods before launch. However, this propellant was flown with success on the SpinSat mission in 2014, where impermeable caps were put in place to prevent moisture absorption before deployment [26]. In our previous work it was found that at standard laboratory atmospheric conditions a ~1.2 g sample of HIPEP absorbs moisture from the atmosphere at a rate of 0.75 mg/min [27]. Further, samples of HIPEP contain some percentage of water (DSSP estimates 1-5%) when received from the manufacturer. In vacuum, this water evaporates from the sample, skewing mass loss measurements unless special preparation procedures are implemented. In the present work, HIPEP samples are only handled and measured while in a nitrogen-purged inert-atmosphere environment glovebox with less than 10% relative humidity and a pressure of ~2 psig. The samples are exposed to standard laboratory environment for ~5 min when being transferred to the test article in the vacuum facility. During this time, it is estimated the samples may absorb up to ~0.5% mass in water vapor, but that vapor is then subsequently evaporated during the facility pump-down procedure, where samples are at less than 10^{-3} torr for over 2 hours.

A special drying procedure is used for individual samples. First, the mass of a fresh sample is measured in the inert environment, where it is then loaded into a small sealable volume. This volume is then connected to a small vacuum facility and the system is kept at ~50 mtorr for at least 24 hours, allowing the moisture absorbed by the propellant to desorb and evaporate. This volume is then returned to the inert environment and vented allowing for measurement of the propellant “dry” mass. At this point, the propellant sample is loaded into the test article, installed in the vacuum chamber, and tested through exposure to an arc discharge for a targeted number of 100 times per test run. After testing, a post-test “wet” sample mass is measured before reinserting the sample in the sealable volume and drying at 50 mtorr for another 24 hours. Finally, the post-test dry mass is measured. The same drying process was conducted for the PTFE samples which exhibited minimal moisture absorption. Quantitative details showing the evolution of HIPEP and PTFE mass due to moisture content are presented in Section 4.1.

2.4. TEST ARTICLE

A coaxial geometry pulsed plasma discharge chamber was used for the ablation mass study. Figure 2 details the geometry of the discharge chamber. It should be noted that this device was designed primarily to study the mass ablation of the propellants and not as a thruster. A circular stainless steel rod serves as the anode (positive) and a stainless steel plate with a circular hole serves as the cathode (ground). The assembly is housed in a nonconductive PEEK body. The propellant tube sample has length 12 mm and inner diameter 6.35 mm. Because HIPEP is conductive, the propellant is isolated electrically from the two electrodes by thin PTFE washers with inner diameter ~7 mm. These washers have an approximate thickness of ~0.5 mm which is sufficient to hold off the maximum voltage (2.23 kV) used in the present work. The washers remain during PTFE testing to keep electrode spacing consistent between propellant samples.

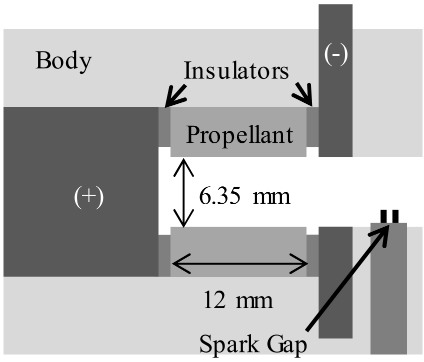

Figure 2: Diagram of the coaxial pulsed plasma discharge chamber test article.

The test article and the capacitor bank are co-located inside the vacuum test facility. It is intended that the arc discharge occurs in the cylindrical cavity formed by the inner propellant tube wall and the anode end, with current flowing between the anode and cathode. This current sheet does not propagate in the cavity, meaning the discharge has static impedance, and thus no electromagnetic thrust component. Because the test article is at vacuum, the capacitor can be charged to a large voltage (1-5 kV) across the anode/cathode-gap without initiating a Paschen breakdown. Breakdown of the gas is initiated by a surface discharge igniter constructed of two tungsten wires cemented in a two-bore alumina tube with ~2 mm exposed tip lengths. The wire tips are located in the exhaust channel just downstream of the cathode as shown in Figure 2. A capacitor discharge ignition (CDI) circuit creates a low energy spark across the tungsten wire tips, introducing a number of electrons into the cylindrical cavity of propellant. These electrons are accelerated to the positively charged anode and sputter particles from it and the nearby propellant, seeding the main arc discharge and allowing current to flow. The capacitor bank is then recharged and triggered again at a repetition rate of once per ~20 seconds, meaning the propellant cools to room temperature after each discharge.

2.5. ELECTRICAL SETUP

The electrical setup for the experiment is similar to that of a laboratory bench-top PPT and is presented in Figure 3. A high voltage power supply is set to the desired discharge voltage, V_0. The power supply is a Glassman HV FJ05R24 model with a maximum DC voltage output of 5 kV and maximum current output of 24 mA. This supply charges the capacitance C through a 500 Ω high power charging resistor, which also serves to prevent the pulsed current from back-flowing into the supply. The capacitance *C* is comprised of a bank of eight 1 μF capacitors each rated for 2.4 kV with metallized polypropylene dielectric material. This bank was measured to have a capacitance of 8.055 μF. In the present work, the bank was charged to voltages corresponding to stored nominal energy levels of E_0 = 5, 10, 15 and 20 J. During each discharge, an Ion Physics Corp. CM-1-MG pulse current monitor measures the current, *I(t)*, entering the anode. This device is a self-integrating ferrite-cored current with a maximum measurable peak current of 50 kA and outputs 0.1 Volts/Amp via coaxial connection. A Tektronix TDS2024B oscilloscope (up to 200 MHz, 10^9 samples/s) was used to capture the waveform output by the current monitor after 10x attenuation. Not shown in the circuit diagram is the CDI spark gap circuit. The spark gap circuit is a single cylinder ignition unit manufactured by CH Ignitions with capacitance 0.47 μF and stored energy of about 40 mJ which is negligible relative to that of the main capacitor bank. The low voltage pulse is transformed by an ignition coil to yield an output voltage of 30-35 kV. This ignition unit was triggered manually by a push-button via an electromechanical relay.

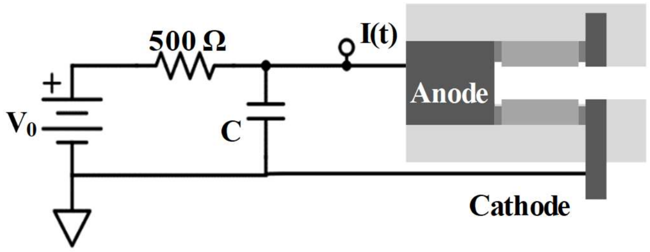

Figure 3: Circuit diagram for the pulsed plasma discharge chamber test article.

3. LCR CIRCUIT MODEL

Pulsed accelerators with a thin arc current layer (a current sheet) can be analytically represented as a switched lumped-element inductance-capacitance-resistance (LCR) series circuit [28], as shown in Figure 4. A capacitance C is initially charged to a voltage V_0. At time t=0, the voltage is switched across a time-varying inductance $L(t)$ and resistance $R(t)$. The initial inductance is a function of the circuit geometry and the internal inductance of the capacitor while the initial resistance is a combination of the external circuit resistance and the resistance presented to the circuit by the arc discharge.

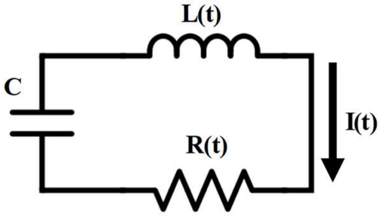

Figure 4: Ideal inductance-capacitance-resistance series circuit.

At time t=0, the circuit has an initial inductance L_0 and resistance R_0 and for the moment we will consider these as fixed values throughout the duration of the discharge. Examination of the time-varying charge stored on the capacitor and invoking current continuity yields a second-order ordinary differential equation with known initial conditions. For practical values of inductance, resistance and capacitance, the solution typically takes the underdamped oscillatory form given in Jahn [28]. The solution can be written in terms of the current $I(t)$ as

$$I(t) = -\frac{dQ}{dt} = \frac{V_0}{\omega_d L_0} \exp\left(-\frac{R_0 t}{2L_0}\right) \sin(\omega_d t) \tag{1}$$

where

$$\omega_d = \left(\frac{1}{L_0 C} - \frac{R_0^2}{4L_0}\right)^{1/2} \tag{2}$$

In the present work, Eq. (1) will be matched to the measured current waveform for a fixed V_0 test case. This is achieved by first matching the period of the sine function, $P = 2\pi/\omega_d$, to the numerically determined oscillatory period of the measured waveform from the test circuit. The period P is largely dominated by the value of L_0 such that it can be assumed R_0 is negligible, permitting the use of $P = 2\pi(L_0C)^{1/2}$ in determining the value of L_0. The current amplitude is then largely determined by the value of R_0. With a fixed value of L_0, the resistance value can be selected such that the model-predicted values of $I(t)$ best fit, in a least squares sense, the measured current waveform for the first full period. Specifically, we iterate upon R_0 until the sum of residuals squared is minimized between $I_{EXP}(t)$, the experimentally measured current waveform, and $I(t)$, the current predicted by the LCR circuit model for $t<P$. After the first full cycle (one-period), results show the measured current waveform has higher damping than the LCR model least-squares fit would predict (assuming constant R_0), indicating that the resistance of the circuit is not constant for the entire discharge. To account for this, we modify the simple LCR model with a linearly increasing resistance, $R(t)$, beginning after the end of the first period. This $R(t)$ replaces R_0 in the fixed-element solution for underdamped current in Eq. (1). The profile of the variable resistance is found by repeating the above residual-minimization process for the second period of oscillation. This process is repeated for a single discharge current waveform for a combination of each propellant and each initial capacitor energy

value. Because the variation in peak discharge current is less than 2% over the duration of each test, this current is representative of all the discharges for each combination of experimental variables.

4. RESULTS

Experimental results are presented in this section. The mass loss of HIPEP propellant samples during vacuum drying is first reported. Arc discharge ablation mass loss measurements for both propellants are then reported. This section concludes with a presentation of the measured arc discharge current.

4.1. HIPEP MOISTURE CONTENT

Using the propellant sample preparation procedures detailed in Section 2.0, the amount of water in a given propellant sample can be determined as a percentage of the sample mass. Details of mass measurements for six samples of HIPEP and three samples of PTFE are shown in Figure 5. These measurements were performed using the scale described in Section 2.1 with measurement error of $\pm 3\times10^{-5}$ g which is not visible on the scale of this figure.

Figure 5a details the mass of the first three HIPEP samples as a function of time. Time t=0 in this figure corresponds to the removal of the samples from the original packaging. Interim measurements are performed during the initial drying at 7 hours and 24 hours, with the final measurement recorded after 48 hours of drying. Ablation testing is performed after this, with the post-test wet mass recorded at 54 hours. Finally the post-test dry mass is recorded at 78 hours.

These data illustrate the need for the propellant sample preparation procedures outlined in Section 2.0, and the pre-test mass measurements were not made in multiple intervals for subsequent samples. Propellant samples absorb water from the atmosphere, which evaporates in vacuum. The mass of the three samples all decrease during pre-test drying at 5×10^{-2} torr. Between 24-48 hours of vacuum drying the sample mass is at a steady-state value; this is the pre-test mass. Samples then undergo ablation testing in the test article described previously. This testing typically lasts 6 hours. After testing, the facility is vented to atmospheric pressure during which time the sample is exposed to humid air and absorbs an unknown quantity of water. Samples then undergo the post-test drying process at 5×10^{-2} torr to obtain the post-test dry mass. The difference between the pre- and post-test dry masses is taken as the mass lost due to the ablation of propellant.

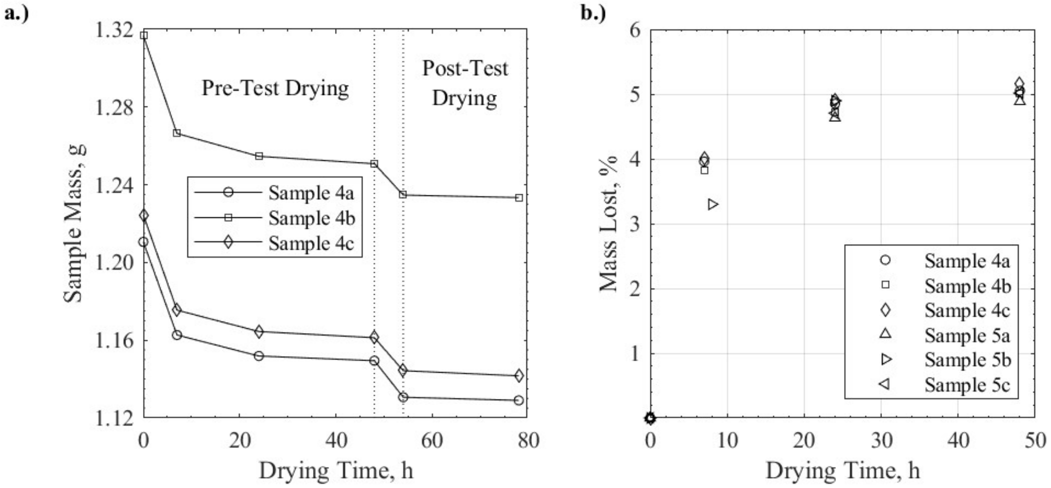

Figure 5: a.) Sample mass evolution for three HIPEP samples and b.) percent mass lost during pre-test drying of six HIPEP samples.

Figure 5b shows the mass lost during vacuum drying for six HIPEP samples and three PTFE samples as a percentage of initial sample mass. PTFE samples exhibit minimal water absorption, and less than 0.01% mass is lost over 48 hours of drying. The fresh samples of HIPEP have absorbed about 5% water by mass by the time they are removed from the original packaging received from the manufacturer. After 6-8 hours of vacuum drying, the sample mass has decreased by ~3-4%. After 24 hours of drying the samples have decreased by 4.5-5% in mass. Further mass lost after 48 hours of vacuum drying is minimal, and the mass of all six samples has decreased by an average of 5.0%. Thus, the standard vacuum drying time for sample preparation was selected as 24 hours, at which point the measured mass of the sample is within 0.26% of the initial 'dry' mass. Note that the samples discussed in Figure 5a were dried for longer than the standard drying time to illustrate that the mass was approaching steady-state.

4.2. ABLATION MASS LOSS

For each discharge energy level three samples of each propellant were tested and the mass loss was measured. Energy levels of 5, 10, 15, and 20 J were investigated. Each propellant sample was prepared as described in Section 2.0. Prior to testing, the initial dry mass was recorded to an accuracy of ±0.03 mg. During testing, the charge voltage was kept constant for 100 pulses of the test article, with ~20 s between successive discharges of the device. The post-test dry mass was then recorded immediately after, with the drying procedure again employed following testing. The mass loss is taken as the difference in the pre- and post-test dry mass measurements. The mass loss measurements are summarized in Table 2. Also presented are calculated values for the mass loss per pulse and mass loss per unit discharge energy (specific ablation). Note that two different test runs of HIPEP samples were unable to achieve the nominal test length of 100 pulses. Both runs were at the 15 J energy level and the failure was due to a short in the spark gap igniter. Those two test runs were successfully repeated with fresh samples for 100 pulses and the results of both the shortened and nominal-length test runs are presented. Note also that a fourth test run was conducted for the 5 J energy level for HIPEP due to one potential outlier trial.

Similar trends are observed between the two propellants in these results. In general, as the initial energy increases so too does the mass lost, but the specific ablation remains relatively constant from 5 to 20 J for both propellants. Consider the 1120 V testing case. The initial energy is 5.05 J and the specific ablation of PTFE was 7.5 µg/J on average for the three test runs conducted. The average mass loss per pulse for HIPEP at 5.05 J initial energy was 99 µg, which yields a specific ablation of 19.6 µg/J, much greater than that of PTFE. This is true for all the energy levels, with HIPEP specific ablation always greater than that of PTFE. For HIPEP, the estimated error in mass loss measurements is ±3.5 mg due to the 0.26% uncertainty in the initial mass measurement of each sample, leading to an error on the specific ablation calculation of ±3.5 µg/J.

The specific ablation for both propellants is presented in Figure 6 as a function of discharge energy. Typical measurement errors for PTFE and HIPEP, ϵ_P and ϵ_H, respectively, are also displayed. Note that the two failed test runs of HIPEP samples at 15 J (only 40 and 75 pulses instead of the intended 100) are reported here and marked with an “x” symbol although they do not deviate significantly from other tests at that energy. For the PTFE measurements, a specific ablation of 7.2 μg/J was measured on average over all pulses and energy levels.

Table 2: Ablation mass loss measurements for PTFE and HIPEP.

propellant	energy, J & (V_0)	mass loss, mg (±0.5 mg)	pulses	Δm/pulse, μg/pulse (±5 μg)	specific ablation, μg/J (±0.5 μg/J)
PTFE	5.05 (1120 V)	3.7	100	37	7.3
		3.8	100	38	7.6
		3.8	100	38	7.5
	10.18 (1590 V)	8.2	100	82	8.1
		7.7	100	77	7.5
		7.0	100	70	6.8
	15.00 (1930 V)	9.5	100	95	6.3
		10.9	100	109	7.2
		10.5	100	105	7.0
	20.03 (2230 V)	13.4	100	134	6.7
		14.0	100	140	7.0
		13.8	100	138	6.9

propellant	energy, J & (V_0)	mass loss, mg (±3.5 mg)	pulses	Δm/pulse, μg/pulse (±35 μg)	specific ablation, μg/J (±3.5 μg/J)
HIPEP	5.05 (1120 V)	7.1	100	71	14.1
		8.6	100	86	16.9
		7.7	100	77	15.3
		16.1	100	161	31.9
	10.18 (1590 V)	20.4	100	204	20.0
		19.6	100	196	19.3
		17.4	100	174	17.1
	15.00 (1930 V)	22.8	100	228	15.2
		10.9	100	109	7.3
		16.6	100	166	11.1
		6.7	40	166	11.1
		9.0	75	120	8.0
	20.03 (2230 V)	17.6	100	176	8.8
		23.9	100	239	11.9
		28.5	100	285	14.2

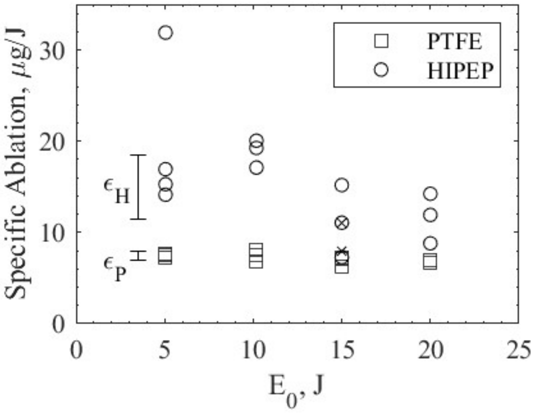

Figure 6: Specific ablation of PTFE and HIPEP materials for 5, 10, 15, and 20 J nominal initial energy. Typical measurement error bars shown for PTFE ($\boldsymbol{\epsilon_P}$) and HIPEP ($\boldsymbol{\epsilon_H}$).

In contrast, the average over all pulses and energies for HIPEP was calculated to be 14.8 μg/J, a factor of 2.1 greater than the specific ablation of PTFE. More discussion on this observation is presented in Section 5.2. The average specific ablation decreases from 19.6 μg/J at the 5.05 J energy level to 18.8 μg/J at 10.18 J, but this is skewed by an anomalously high measurement of 31.9 μg/J for one trial at 5.05 J compared to the average 15.5 μg/J for the other three trials. The exact cause of this outlier is undetermined, though it could be attributed inadvertent exposure to moisture or an unnoticed loss of a chunk of propellant. This decreasing trend continues to the two higher energy levels, but this is likely an artifact of the large variation in HIPEP specific ablation measurements rather than a real phenomenon. Within the error bars, the trend is generally constant as it was for PTFE. It is clearly observed that the variance in the specific ablation of HIPEP is much greater than that of PTFE. The standard deviation in specific ablation of PTFE is 0.47 μg/J which lies within the measurement error of 0.5 μg/J. However, the standard deviation for HIPEP is 6.1 μg/J which is nearly twice the measurement error of 3.5 μg/J. This variation is introduced by different samples tested at the same energy level. Similar behavior (e.g. shot-to-shot, across sample and across batch variation) has been previously observed in pulsed thrusters operating on HIPEP [29, 30].

4.3. DISCHARGE CURRENT

The discharge current is measured using an oscilloscope to capture the output of a high current transformer. This raw waveform was post-processed by first applying a 5-point moving average filter then reduced to ~540 points via linear interpolation, introducing <0.02% change in the calculated waveform area. The variance in this current waveform is minimal from pulse to pulse at each selected voltage, with a cumulative change in waveform peaks of ~2% over 100 pulses. Figure 7 presents a current measurement for both PTFE and HIPEP at a nominal initial energy of 15 J, which is representative of the discharge current for all pulses. At 15 J, the peak current typically varied less than 1% from pulse 1 to pulse 100, with the maximum variation over the current waveform less than 4%. The discharge current is similar between propellants. Peak current in Figure 7a (PTFE) is 8.89 kA, which compares to the peak current in Figure 7b (HIPEP) of 8.69 kA; a difference of only 2.3%. The first negative current peak has a difference of 6.3% between propellants and the second positive current peak is 19% different between the two propellants, with the current amplitude always greater for the PTFE discharge. The only major distinction between the qualitative form of two current waveforms is the lack of a third positive current maximum for the HIPEP discharge. These observations indicate that the circuit is more damped when using HIPEP.

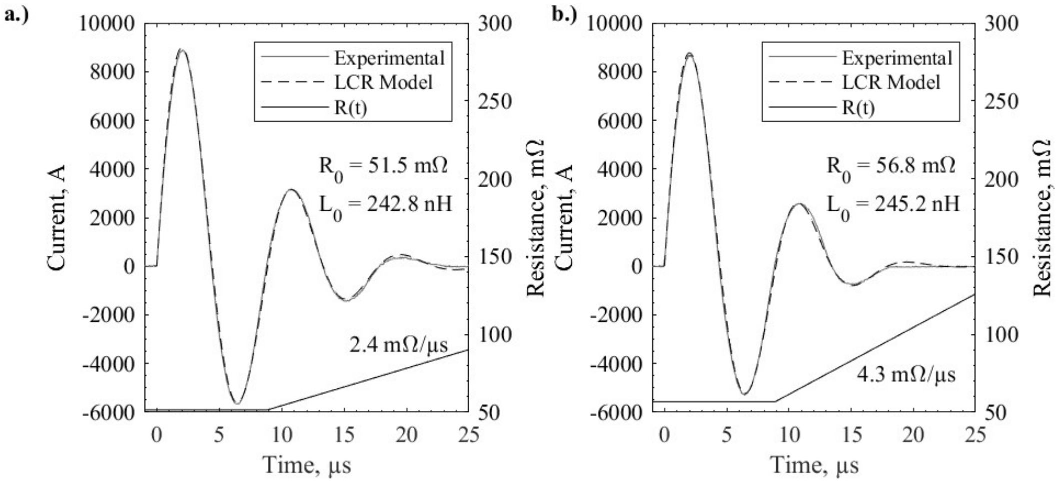

Figure 7: Discharge and LCR circuit model current for a.) PTFE and b.) HIPEP, both at a nominal 15 J initial energy.

Table 3: Discharge current characteristics for PTFE and HIPEP.

propellant	***E₀*** **(J)**	**peak *I(t)* (kA)**	***P* (µs)**
PTFE	5.05	4.98	8.97
	10.18	7.24	8.88
	15.00	8.89	8.79
	20.03	10.30	8.78
HIPEP	5.05	4.89	8.98
	10.18	7.07	8.98
	15.00	8.69	8.84
	20.03	10.26	8.74

The period of the waveform was calculated by extracting the times corresponding with the first and third roots of the experimental current data. For the PTFE current in Figure 7a, the period was calculated to be 8.79 µs while a period of 8.84 µs was calculated for HIPEP at the same energy. This difference of <0.5% indicates that the inductance of the circuit is essentially identical for both propellants. This observation holds at all other initial energy cases. The peak current and period of the waveforms are tabulated in Table 3. Overall the peak current for a HIPEP device is measured to be 0-2.5% less than the peak current for the PTFE device, and the calculated period has a difference of less than 2% for all cases.

5. ANALYSIS AND DISCUSSION

The following section presents an analysis of the reported results and discussion on their significance. Details from the LCR circuit model current fit method are first presented for both propellant configurations, followed by further investigation of the energy used for ablation of each propellant.

5.1. LCR CIRCUIT MODEL

An LCR circuit model is used to generate a theoretical current waveform with the given C, V_0 and matched to the measured discharge current, as described in Section 3. The model is used to estimate a constant inductance value and resistance profile for the complete circuit. Comparison of the raw current waveform with the fixed-element solution clearly indicates that the resistance is not constant for the duration of the discharge. We have elected to use a piecewise resistance profile with constant initial resistance, R_0, and linear increase after one period. The reader should not attribute physical significance to the linearity of the increase instead of a quadratic, or exponential one. An increase in the circuit resistance is apparent, and a simple linear model fits the data closely. Figure 7 presents the current measurement and the modeled current along with the calculated resistance and inductance for both PTFE and HIPEP at a nominal initial energy of 15 J.

The circuit model current for both propellants exhibits a best fit to the experimental data in Figure 7 for an inductance of ~240 nH. For PTFE, the initial resistance value for the fit is 51.5 mΩ while for HIPEP it is 56.8 mΩ, which produce the best fit to within 0.1 mΩ. After one period, the model current fits best with an increase in resistance of 2.4 mΩ/μs for PTFE and 4.3 mΩ/μs for HIPEP. The inductance is nearly identical between propellants resulting in very similar periods, which match to within 1%. The circuit is more damped when using HIPEP, as the initial resistance is ~10% greater than for PTFE, and after one period it increases at a linear rate that is 1.8 times greater for 15 J energy. Note that the calculated resistance and inductance of the circuit in the LCR model are equivalent values for the *entire* circuit. Both quantities represent contributions from three primary sources: the capacitor, the electrodes and the plasma [31]. At a frequency of 100 kHz, the dissipation factor of a single capacitor in the bank is rated less than 5×10^{-4} per the datasheet. Thus, the resistance of the capacitor bank at 100 kHz (i.e. same order of the discharge timescale in the present work) is estimated on the order of 0.1 mΩ which is comparable to the resistance of the wires and connections of the entire circuit and is negligible here. At room temperatures, the resistivity of stainless steel is ~7×10^{-7} Ω-m and at 100 kHz the skin depth is 1.3 mm, which suggests the resistance of the anode and cathode electrodes is a constant R_{elec} = 1.2 mΩ. Therefore, we conclude that the plasma resistance is dominant in the circuit, estimated to be 50-54 mΩ. From the datasheet, the equivalent series inductance for one of the 1 μF capacitors in the bank is ~115 nH. The inductance of the test article is then ~125 nH and is independent of the propellant used. The energy resistively dissipated in the arc discharge was computed using the integral of instantaneous power defined as

$$E = \int P(t)\,dt = \int I_{EXP}(t)^2 R_p(t)\,dt \tag{3}$$

where the plasma resistance is defined as the piecewise function

$$R_p(t) = \begin{cases} R_0 - R_{elec} & t \leq P \\ R_0 - R_{elec} + R_1 * (t - P) & t > P \end{cases} \tag{4}$$

For PTFE the energy resistively dissipated in the arc is 13.71 J, which is ~91.4% of the 15 J stored on the capacitor. For HIPEP, 13.63 J (90.9% of 15 J) is dissipated in the arc discharge. The remainder of the energy stored initially on the capacitor is dissipated resistively through the other circuit elements (capacitor, electrodes, wires, etc.) and other loss effects not captured by this simple model. Our circuit analysis was performed for each discharge energy and propellant combination, with the results summarized in Table 4. From Table 4, the equivalent circuit inductance is roughly constant for all propellants and discharge energy levels, indicating that the conductivity of the HIPEP material is not contributing to the inductance of the circuit. The inductance of coaxial conductors having an inner diameter *ID*, outer diameter *OD*, and length *l* is defined by

$$L_{coax} = \frac{\mu l}{2\pi} \ln\left(\frac{OD}{ID}\right) \tag{5}$$

where μ is the permeability of the medium separating the conductors. The results of Table 4 show that the total circuit inductance remains constant between propellants. Because the external circuit does not change with propellant, this result suggests that L_{coax} also remains constant between propellants. Because *OD, ID* and *l* are also constant between propellants, Eq. (5) combined with our results suggests that μ is constant and that the circuit inductance is only a function of the geometry.

The initial plasma resistance for the HIPEP propellant is greater than for the PTFE propellant by an average of about 7%, and the slope of increase after the first period is on average 1.5 times greater for HIPEP. The initial plasma resistance decreases with increasing energy for both propellants, reducing by -1.03 mΩ/J for PTFE and -1.32 mΩ/J for HIPEP. Similarly, the slope R_1 also decreases with increasing energy. The energy resistively dissipated in the arc is calculated as 90-91% of the initially stored energy for both propellants. It is reasonable to assume that the temperature of the arc would increase as a function of dissipated energy, which qualitatively agrees with Spitzer's relation for decreasing resistivity in plasma as a function of increasing temperature [32]. Approximating the arc as a fully ionized plasma of cylindrical volume with diameter 6.35 mm, length 12 mm, and total resistance of 50 mΩ, we calculated a resistivity of 13.2 mΩ-cm, which we assumed is uniform. Using Spitzer's relation for electron-ion collisions in this plasma taking Z=1 and the Coulomb logarithm as 10, the estimated temperature of the arc is ~2.5 eV (~29,000 K). This simple calculation for a fully ionized plasma is not strictly justified given the low density, partially ionized, mixed species gas that constitutes the arc discharge, but it provides a first order approximation. The plasma temperature is comparable with those measured in other PPTs using PTFE propellant [10, 13].

Table 4: LCR circuit model analysis results.

propellant	**E_0 (J)**	**L_0 (nH)**	**R_0 (mΩ)**	**R_1 (mΩ/μs)**	**E (J)**	**E / E_0**
PTFE	5.05	252.6	63.8	6.6	4.58	90.7%
	10.18	247.4	57.4	4.8	9.27	91.1%
	15.00	242.8	51.5	2.4	13.71	91.4%
	20.03	241.9	49.7	2.1	18.25	91.1%
HIPEP	5.05	252.9	70.5	9.9	4.55	90.1%
	10.18	253.1	59.8	6.0	9.22	90.6%
	15.00	245.2	56.8	4.3	13.63	90.9%
	20.03	240.1	51.3	3.6	18.13	90.5%

5.2. ABLATION ENERGY BALANCE

Table 2 and Figure 6 detail the ablation mass loss and specific ablation values measured in this work. The specific ablation of PTFE is a constant value of 7.2 μg/J on average. The measured values of specific ablation and its constancy as a function of discharge energy are typical of a PPT [33]. Further, the large variation in specific ablation between samples of HIPEP that should otherwise be identical has also been observed in previous experimental efforts with this material [29]. Burton and Turchi reported similar values in the range of 1.5-10 μg/J for a number of PPTs, including both coaxial and rectangular geometries operated at various energy levels [10]. These results indicate that the HIPEP material ablates more readily in an arc discharge than PTFE, with average specific ablation a factor of ~2 greater than PTFE. In a previous investigation by the authors [29] the specific ablation for HIPEP was found to be 5.4 μg/J. In this work, the specific ablation of HIPEP was measured to be 14.8 μg/J on average. Note that the present work features a radically different experimental configuration, both geometrically and electrically, compared to the previous investigation. Arc discharge temperatures are likely much greater in the present work which elicits increased ablation from the propellant surface.

For polymers like PTFE, the heat of vaporization, h_v, is comprised mainly of the energy for phase transition to gas h_f and the energy for depolymerization h_d, with a small portion attributed to transient heating of the propellant from room temperature, $C_p\Delta T$. It is known [10] that for PTFE the heat of vaporization to create pure C_2F_4 vapor is h_v = ~2×10^3 J/g. At temperatures common in PPTs (i.e., >1 eV, >11,600 K), PTFE vapor plasma is dominated by monatomic species and ions [34, 35]. The energy required to dissociate C_2F_4 into monatomic species C and F is identical to the heat of formation, ΔH_f^0, which is 8.3×10^3 J/g. For PTFE, an estimate of the fraction, ξ, of the total energy dissipated in the arc E, calculated using the LCR circuit model and reported in Table 4, that is directed into heating, vaporizing and dissociating the ablated propellant may be calculated by

$$\xi = \frac{m_1\left[\left(h_f + h_d + C_P\Delta T\right) + \Delta H_f^0\right]}{E} = \frac{m_1\left[h_v + \Delta H_f^0\right]}{E} \tag{6}$$

where m_1 is the mass of the ablated propellant. If we consider ξ known, for the moment, Eq. (6) may then be rewritten to calculate the "theoretical" ablated mass as

$$m_1 = \frac{\xi E}{h_v + \Delta H_f^0} \tag{7}$$

HIPEP does not undergo a vaporization process like PTFE. While the exact behavior of HIPEP at high temperatures is currently not known, it is known that the primary constituent of the material, HAN, undergoes a thermal decomposition process at a temperature of about 470 K. Lee and Litzinger [36] conducted a study of this process and found that the first reaction initiates the thermal decomposition process by producing hydroxylamine and nitric acid. Further, the timescale of this reaction was estimated on the order of 10^{-10} sec, which is much faster than the 10^{-6} sec timescale of the arc discharge. The activation energy h_a for this initiation reaction is 6.57×10^2 J/g, per Lee and Litzinger [36]. It is likely safe to assume that a HAN ($H_4N_2O_4$) vapor plasma at temperatures greater than 1 eV (11,600 K) will be mostly composed of monatomic species and ions, as is the case for PTFE. The heat of formation [37] of HAN is ΔH_f^0 = 3.78×10^3 J/g and its specific heat at constant pressure [38] is C_p = 2.29 J/(g-K). Following a similar approach to that described for PTFE, some fraction of the arc energy is assumed to be deposited into three primary modes; propellant heating from room temperature (298 K) to the decomposition temperature $C_P\Delta T$, the activation energy h_a for decomposition, and dissociation of $H_4N_2O_4$ into monatomic species (H, N, and O) equal to ΔH_f^0. It is again possible to account for losses by assuming a fraction ξ of the total arc energy E is consumed in these processes. The theoretical ablated mass of HIPEP, m_2, may be estimated using

$$m_2 = \frac{\xi E}{C_p\Delta T + h_a + \Delta H_f^0} \tag{8}$$

Writing the ratio of the two theoretical ablation masses and assuming for now that ξ is the same for both propellants, we find that m_2/m_1 = 2.14. This ratio is equivalent to ratio of theoretical specific ablation (i.e., $(m_1/E_0)/(m_2/E_0)$) since the initial energy is unchanged between propellants. The calculated specific ablation ratio of HIPEP to PTFE is nearly identical to the measured ratio of approximately 2.1 over the four energy levels, providing a measure of confidence in the ablation energy balance model used here. Further, comparing the measured average ablation mass of PTFE at the 15 J level, m_1 = 103 μg/pulse, to Eq. (7) we find that the fraction ξ = 7.7% of the 13.71 J dissipated in the arc per Table 4. Repeating this calculation for HIPEP at the 15 J level using Eq. (8) we find that ξ = 5.6%, though that is the largest difference in the calculated values of ξ between propellants for a given energy level. It is important to consider that the measured ablation mass also includes mass that evaporates from the hot propellant surface long after the high current discharge has ended, i.e. the late-time ablation mass. The late-time ablation of PTFE has been observed previously in literature [39, 40]. It is estimated that the late-time ablation could be in the range of 40% or more of the measured mass ablated per pulse. A previous investigation by the authors found similar trends for HIPEP, with an estimated late-time ablation fraction of ~45% or more [41]. If we assume that 60% of the measured mass loss is ablated during the discharge and accelerated to a typical APPT average velocity of 6 km/s, we can estimate that the kinetic energy of the gas accounts for ~8% of the energy dissipated in the arc. The heat transfer required to further heat the plume mass from the vaporization temperature of PTFE to 2.5 eV is ~64% of the arc energy, where the specific heat was taken to be 5.0 kJ/kg-K, a rough average over that temperature range [35]. Together, the ablation, heating and acceleration of the plume mass is estimated to require ~80% of the 13.71 J arc energy. The remaining 20% is likely radiated through the downstream orifice or transferred as heat conduction to the rest of the test article. The above values (exhaust velocity, vapor specific heat) are not yet known with any confidence for HIPEP, but given the results shown here it is reasonable to expect they will be similar. In the preceding discussion, only the ablated mass that is heated to high temperatures and accelerated by the arc discharge is considered. Thus, it is deemed unnecessary to consider any exothermic chemical component of this energy balance for HIPEP due to its pyroelectric nature. The timescales for the pyroelectric chemical reactions are much longer than the 10^{-6} s timescale of the discharge. This reaction may, however, incite the generation of heat after the arc discharge and lead to increased late-time ablation.

6. CONCLUSIONS

Polytetrafluoroethylene (PTFE) and an electric solid propellant known as HIPEP were studied in a pulsed electric arc discharge chamber similar to an electrothermal pulsed plasma thruster. The test apparatus was specifically designed to permit the quantification of mass ablated in a pulsed electrical arc discharge as a function of discharge energy and propellant type. The mass lost over 100 pulses of the arc discharge was recorded for samples of both propellants at nominal discharge energies of 5, 10, 15 and 20 J. The discharge current was measured and an LCR circuit model was fit to the measured current assuming a constant inductance and an initially-constant resistance that linearly increased after one period of the discharge.

Mass loss measurements indicate a specific ablation of 7.2 μg/J for PTFE and 14.8 μg/J for HIPEP. For both propellants, this value remains constant with increasing initial energy, which is typical in coaxial PTFE-fed PPTs. HIPEP has a specific ablation that is ~2.1 times that of PTFE. Examination of energy balance for the ablation process for both propellants suggests that ~8% of the arc energy is used to ablate propellant. This analysis also suggests that HIPEP should have a specific ablation that is ~2 times that of PTFE, agreeing with the experimental measurements.

A lumped-element circuit model is compared to the discharge current measurements and indicates that the arc discharge has a constant inductance of about 125 nH in all cases. The initial resistance is typically 50-60 mΩ for PTFE and 3-10% greater for HIPEP, depending on the discharge energy. These observations suggest the difference in conductivity of propellants does not significantly affect the circuit inductance. Further, the arc temperature is calculated to be comparable between the two propellants, and is ~2.5 eV. In the second period, the resistance increases at an increased rate for HIPEP, indicating that the HIPEP plasma cools more rapidly than the case of PTFE.

Results presented both in this work and in a previous work comparing PTFE and HIPEP in pulsed electric devices suggest that the physics of the high temperature arc ablation process is similar for both propellants. The short timescale ablation physics for each propellant appear to be set apart merely by thermal material and transport properties. The long timescale pyroelectric behavior of HIPEP does not play a role in arc ablation of the material. Thus, ablation models for PTFE may serve as the framework in development of new models for HIPEP and potentially other electric solid propellants. Key inputs to these models will need to be examined and adjusted for material property differences, and to quantify key chemical composition and thermodynamic properties.

ACKNOWLEDGMENTS

M. S. Glascock would like to graciously thank the NASA Space Technology Research Fellowship program, which has supported his Ph.D. research which includes this work through grant NNX15AP31H. The authors would also like to thank DSSP for not only providing custom made orders of the propellant samples, without which this work would not exist, but also allowing our group to work with their technology and intellectual property for academic purposes.

REFERENCES

[1] Sawka, W. N., and McPherson, M., "Electrical Solid Propellants: A Safe, Micro to Macro Propulsion Technology," *49th AIAA/ASME/SAE/ASEE Joint Propulsion Conference*, AIAA Paper 2013-4168, San Jose, CA, 2013.

[2] Sawka, W. N., U.S. Patent for a "Controllable Digital Solid State Cluster Thrusters for Rocket Propulsion and Gas Generation," No. 7958823 B2 and 8464640; June 14, 2011 and June 18, 2013.

[3] Dulligan, M., U.S. Patent for a "Electrically Controlled Extinguishable Solid Propellant Motors," No. 7788900B2; September 7, 2010.

[4] Chung, K., Rozumov, E., Kaminsky, D., Buescher, T., Manship, T., Valdivia, A., Cook, P., and Anderson, P., "Development of Electrically Controlled Energetic Materials," *ECS Transactions,* Vol. 50, No. 40, 2013, pp. 59-66.

[5] Grix, C., and Sawka, W. N., U.S. Patent for a "Family of Modifiable High Performance Electrically Controlled Propellants and Explosives," No. 8888935B2; November 18, 2011.

[6] Sawka, W. N., and Grix, C., U.S. Patent for a "Family of Metastable Intermolecular Composites Utilizing Energetic Liquid Oxidizers with Nanoparticle Fuels in Sol-Gel Polymer Network," No. 8317953B2; November 27, 2012.

[7] Baird, J. K., Lang, J. R., Hiatt, A. T., and Frederick, R. A., "Electrolytic Combustion in the Polyvinyl Alcohol Plus Hydroxylammonium Nitrate Solid Propellant," *Journal of Propulsion and Power,* Vol. 33, No. 6, 2017, pp. 1589-1590.

[8] Hiatt, A. T., and Frederick, R. A., "Laboratory Experimentation and Basic Research Investigation Electric Solid Propellant Electrolytic Characteristics," *52nd AIAA/SAE/ASEE Joint Propulsion Conference*, AIAA Paper 2016-4935, Salt Lake City, UT, 2016.

[9] Sawka, W. N., and Grix, C., U.S. Patent for a "Electrode Ignition and Control of Electrically Ignitable Materials," No. 8857338B2; October 14, 2014.

[10] Burton, R. L., and Turchi, P. J., "Pulsed Plasma Thruster," *Journal of Propulsion and Power,* Vol. 14, No. 5, 1998, pp. 716-735.

[11] Gatsonis, N. A., Lu, Y., Blandino, J., Demetriou, M. A., and Paschalidis, N., "Micropulsed Plasma Thrusters for Attitude Control of a Low-Earth-Orbiting CubeSat," *Journal of Spacecraft and Rockets,* Vol. 53, No. 1, 2016, pp. 57-73.

[12] Keidar, M., Zhuang, T., Shashurin, A., Teel, G., Chiu, D., Lukas, J., Haque, S., and Brieda, L., "Electric Propulsion for Small Satellites," *Plasma Physics and Controlled Fusion,* Vol. 57, No. 1, 2015, pp. 1-10.

[13] Bushman, S., and Burton, R. L., "Heating and Plasma Properties in a Coaxial Gasdynamic Pulsed Plasma Thruster," *Journal of Propulsion and Power,* Vol. 17, No. 5, 2001, pp. 959-966.

[14] Cheng, L., Wang, Y., Ding, W., Ge, C., Yan, J., Li, Y., Li, Z., and Sun, A., "Experimental Study on the Discharge Ignition in a Capillary Discharge Based Pulsed Plasma Thruster," *Physics of Plasmas,* Vol. 25, No. 9, 2018.

[15] Wang, Y., Ding, W., Cheng, L., Yan, J., Li, Z., Wang, J., and Wang, Y., "An Investigation of Discharge Characteristics of an Electrothermal Pulsed Plasma Thruster," *IEEE Transactions on Plasma Science,* Vol. 45, No. 10, 2017, pp. 2715-2724.

[16] Aoyagi, *et al.*, "Total Impulse Improvement of Coaxial Pulsed Plasma Thruster for Small Satellite," *Vacuum,* Vol. 83, No. 1, 2008, pp. 72-76.

[17] Edamitsu, T., and Tahara, H., "Experimental and Numerical Study of an Electrothermal Pulsed Plasma Thruster for Small Satellites," *Vacuum,* Vol. 80, No. 11, 2006, pp. 1223-1228.

[18] Miyasaka, T., Asato, K., Sakaguchi, N., and Ito, K., "Optical Measurements of Unsteady Phenomena on Coaxial Pulsed Plasma Thrusters," *Vacuum,* Vol. 88, 2013, pp. 52-57.

[19] Markusic, T. E., Polzin, K. A., Choueiri, E. Y., Keidar, M., Boyd, I. D., and Lepsetz, N., "Ablative Z-Pinch Pulsed Plasma Thruster," *Journal of Propulsion and Power,* Vol. 21, No. 3, 2005, pp. 392-400.

[20] Keidar, M., Boyd, I. D., and Beilis, I. I., "Electrical Discharge in the Teflon Cavity of a Coaxial Pulsed Plasma Thruster," *IEEE Transactions on Plasma Science,* Vol. 28, No. 2, 2000, pp. 376-385.

[21] Keidar, M., Boyd, I. D., and Beilis, I. I., "Model of an Electrothermal Pulsed Plasma Thruster," *Journal of Propulsion and Power,* Vol. 19, No. 3, 2003, pp. 424-430.

[22] Ruchti, C. B., and Niemeyer, L., "Ablation Controlled Arcs," *IEEE Transactions on Plasma Science,* Vol. PS-14, No. 4, 1986, pp. 423-434.

[23] Schönherr, T., Komurasaki, K., and Herdrich, G., "Propellant Utilization Efficiency in a Pulsed Plasma Thruster," *Journal of Propulsion and Power,* Vol. 29, No. 6, 2013, pp. 1478-1487.

[24] Seeger, M., Tepper, J., Christen, T., and Abrahamson, J., "Experimental Study on PTFE Ablation in High Voltage Circuit-Breakers," *Journal of Physics D: Applied Physics,* Vol. 39, No. 23, 2006, pp. 5016-5024.

[25] Wang, W., Kong, L., Geng, J., Wei, F., and Xia, G., "Wall Ablation of Heated Compound-Materials into Non-Equilibrium Discharge Plasmas," *Journal of Physics D: Applied Physics,* Vol. 50, No. 7, 2017.

[26] Nicholas, A., Finne, T., Galysh, I., Mai, A., Yen, J., Sawka, W. N., Ransdell, J., and Williams, S., "SpinSat Mission Overview," *27th Annual AIAA/USU Conference on Small Satellites*, AIAA Paper SSC13-I-3, Logan, UT, 2013.

[27] Glascock, M. S., and Rovey, J. L., "Electric Solid Propellant in a Pulsed Plasma Thruster," *35th International Electric Propulsion Conference*, ERPS Paper IEPC-2017-376, Atlanta, GA, 2017.

[28] Jahn, R. G., *Physics of Electric Propulsion*, New York: McGraw-Hill, 1968.

[29] Glascock, M. S., Rovey, J. L., Williams, S., and Thrasher, J., "Plume Characterization of Electric Solid Propellant Pulsed Microthrusters," *Journal of Propulsion and Power,* Vol. 33, No. 4, 2017, pp. 870-880.

[30] Glascock, M. S., "Characterization of Electric Solid Propellant Pulsed Microthrusters," M.S. Thesis, Missouri University of Science and Technology, 2016.

[31] Shaw, P., "Pulsed Plasma Thrusters for Small Satellites," Ph.D. Thesis, University of Surrey, 2011.

[32] Spitzer, L., *Physics of Fully Ionized Gases*, New York: John Wiley & Sons, 1962.

[33] Rysanek, F., and Burton, R. L., "Effects of Geometry and Energy on a Coaxial Teflon Pulsed Plasma Thruster," *36th AIAA/ASME/SAE/ASEE Joint Propulsion Conference and Exhibit*, AIAA Paper 2000-3429, Huntsville, AL, 2000.

[34] Kovitya, P., "Thermodynamic and Transport Properties of Ablated Vapors of PTFE, Alumina, Perspex, and PVC," *IEEE Transactions on Plasma Science,* Vol. 12, No. 1, 1984, pp. 38-42.

[35] Wang, H., Wang, W., Yan, J. D., Qi, H., Geng, J., and Wu, Y., "Thermodynamic Properties and Transport Coefficients of a Two-Temperature PTFE Vapor Plasma," *Journal of Physics D: Applied Physics,* Vol. 50, No. 39, 2017.

[36] Lee, H., and Litzinger, T. A., "Chemical Kinetic Study of HAN Decompostion," *Combustion and Flame,* Vol. 135, No. 2, 2003, pp. 151-169.

[37] Ashcraft, R. W., Raman, S., and Green, W. H., "Ab Initio Aqueous Thermochemistry: Application to the Oxidation of Hydroxylamine in Nitric Acid Solution," *Journal of Physical Chemistry B,* Vol. 111, 2007, pp. 11968-11983.

[38] Decker, M. M., Klein, N., Freedman, E., Leveritt, C. S., and Wojciechowski, J. Q., "HAN-Based Liquid Gun Propellants: Physical Properties," *US Army Technical Report BRL-TR-2864*, 1987.

[39] Spanjers, G. G., Lotspeich, J. S., McFall, K. A., and Spores, R. A., "Propellant Losses Because of Particulate Emission in a Pulsed Plasma Thruster," *Journal of Propulsion and Power,* Vol. 14, No. 4, 1998, pp. 554-559.

[40] Antonsen, E. L., Burton, R. L., Reed, G. A., and Spanjers, G. G., "Effects of Postpulse Surface Temperature on Micropulsed Plasma Thruster Operation," *Journal of Propulsion and Power,* Vol. 21, No. 5, 2005, pp. 877-883.

[41] Glascock, M. S., Rovey, J. L., Williams, S., and Thrasher, J., "Observation of Late-Time Ablation in Electric Solid Propellant Pulsed Microthrusters," *52nd AIAA/SAE/ASEE Joint Propulsion Conference*, AIAA Paper 2016-4845, Salt Lake City, UT, 2016.

II. THERMODYNAMIC PROPERTIES OF HYDROXYLAMMONIUM NITRATE-BASED ELECTRIC SOLID PROPELLANT PLASMA

Matthew S. Glascock,

Missouri University of Science and Technology, Rolla, MO 65409

Patrick D. Drew, Joshua L. Rovey,

University of Illinois at Urbana-Champaign, Urbana IL 61801

and

Kurt A. Polzin

NASA Marshall Space Flight Center, Huntsville, AL

ABSTRACT

Electric solid propellants are advanced solid chemical rocket propellants controlled by electric current. An electric solid propellant may also be used in an electric propulsion system, specifically, an ablative pulsed plasma thruster. Previous experiments with the electric solid propellant HIPEP suggest its ablation processes are similar to traditional propellant polytetrafluoroethylene (C_2F_4). Better understanding of the ablation and resulting propulsion performance of HIPEP requires a model of its vapor composition, bulk plasma quantities, and thermodynamic properties. This paper reports on the development of such a model. The model was validated by comparing results for C_2F_4 with literature, which showed agreement with multiple previous model predictions. The electric solid propellant vapor composition was predicted in the temperature range of 500-40,000 Kelvin at 1 bar pressure. Low temperatures (<2,000 K) are dominated by H_2O, CO_2 and N_2; results at 700 K match within 10% of previous combustion model predictions. At high

temperatures (>25,000 K) the vapor is strongly ionized and dominated by C^{2+}, O^{2+}, N^{2+}, and H^+ ions. Calculated enthalpy and specific heat is higher for HIPEP vapor than C_2F_4, suggesting increased thermal losses in ablation-controlled discharges fueled by the HIPEP material.

1. INTRODUCTION

Discharge plasmas induced and fed by vaporization and particle ejection from adjacent solid material are used in a number of technological applications including electric circuit protection [1-3], soft x-ray generation [4], laser ablation [5], and pulsed plasma thrusters [6-9]. These ablation-controlled plasmas dissipate energy into the wall of the solid material which ablates and vaporizes. The ablated vapor is then the primary component of the plasma and therefore strongly influences the thermodynamic and plasma properties of the discharge. Thus, the study of ablation-controlled discharges often focuses on the thermodynamic properties of the solid material used in such applications [10-12]. Polymeric materials in particular have been used for many of these applications, especially polytetrafluoroethylene, or PTFE. As a result, many studies are available in the literature today which detail experimental results, computational studies, and physics-based models for ablation-controlled arcs fed by PTFE [2, 12-14]. One such application of ablation-controlled arcs is known as the ablation-fed pulsed plasma thruster, or APPT [8]. A high-current, short duration arc discharge is initiated near the surface of the solid propellant material. Radiation from the high temperature arc heats the surface of the propellant, causing ablation of gaseous propellant species. The energy of the arc heats the gas and can provide high exit velocities via gas-dynamic acceleration, generating thrust. Ablation-controlled plasma physics are at the core of APPT operation, and thus several studies on the ablation of PTFE in APPTs exist in literature [15-18].

A new class of energetic solid materials called electric solid propellants (ESPs) have garnered attention for application in the APPT [19-21]. Initially developed for chemical rockets, ESPs are safe, throttleable, and green (non-toxic) with at-will on-off capability. In chemical rockets, ESPs ignite and pyroelectrically exothermically decompose only when steady electric power is applied at sufficient current and voltage [22]. One particular promising ESP is known as the high performance electric propellant, or HIPEP [23]. The inventors of this propellant and collaborating groups have previously reported on the steady pyroelectric deomposition of this propellant, with some ongoing efforts [24-26]. Recent work has compared HIPEP with traditional PTFE experimentally in ablation-controlled arc discharge test articles [19-21]. One test apparatus was specifically designed to permit the quantification of mass ablated in a pulsed electrical arc discharge as a function of discharge energy and propellant type [21]. The mass loss of HIPEP was roughly twice that of PTFE for a given energy level. This difference in ablation mass between the two propellants was attributed to differences in the material thermal and chemical properties. Previous measurements of HIPEP indicate electron temperatures (1-2 eV) and densities (10^{11}-10^{14} cm^{-3}) of the weakly ionized plume plasma comparable to that of PTFE fueled arcs [19]. High-speed imagery from a pulsed HIPEP arc discharge suggest that the fraction of late-time ablation mass (~50%) is similar between propellants [20]. The short timescale ablation physics for each propellant appear to be quite similar and set apart merely by thermal material properties; the long timescale pyroelectric behavior of HIPEP does not play a role.

The previous experimental results comparing HIPEP and PTFE suggest that ablation models for PTFE (e.g., [6, 15]) may serve as the framework in development of new models for HIPEP and potentially other ESPs, so long as the differences in material properties are accounted for. Among the key inputs to these models, and into bulk plasma models describing density and temperature, are the equilibrium chemical composition and thermodynamic properties of the propellant vapor that constitutes the ablation-controlled plasma. While these properties are quite well-documented for PTFE, none yet exist for HIPEP. Future HIPEP characterization and ablation modeling requires a thermochemical model for the HIPEP as a high temperature vapor plasma. The objective of this work is to develop such a model. We use Gibbs free energy minimization method to determine the equilibrium chemical composition of HIPEP vapor at 1 bar pressure over a temperature range of 500-40,000 K. Classical statistical mechanics are then used to determine thermodynamic properties of the propellant vapor at these conditions. Our model is validated by computing these quantities for PTFE vapor, and then comparing our results with literature. Thermogravimetric analysis is used to examine the vaporization temperature for each material, yielding appropriate low temperature bounds. Predicted HIPEP vapor composition is compared to other work for a low temperature case. Observed differences in the composition and thermodynamic property predictions for PTFE versus HIPEP are highlighted and discussed.

2. MATHEMATICAL MODELS

Thermochemical models are typically obtained via one of two methods. First, examination of the equilibrium constants of a set of reactions can account for two-temperature effects and condensed phases readily, but requires knowledge of the specific elementary and reduction reactions for all species. Second, a Gibbs free energy minimization method for the system of individual species is less complex for increased numbers of species as the species may be treated individually without knowledge of the reactions. Both methods have been applied to PTFE (pure C_2F_4 monomer gas) in the range of 1,000-40,000 K [1, 12]. The specific set of reactions for the constituents of the HIPEP material are not currently known, thus we have elected to apply the Gibbs free energy method. First, the theory of the Gibbs free energy minimization method for determining the chemical composition of a gas at equilibrium is reviewed. Second, a brief discussion of the statistical mechanics approach to approximate thermodynamic properties using the vapor composition is described. Finally, details concerning the chemical makeup and component gas species for each propellant material are presented.

2.1. EQUILIBRIUM COMPOSITION

The method of minimizing the Gibbs free energy of a chemical system to determine its equilibrium state is a commonly used approach. In 1994, Gordon and McBride published a NASA report detailing the methods used in the Chemical Equilibrium with Application (CEA) computer program [27]. This method was followed in the current work to obtain the chemical composition of the given gaseous mixture at local thermal and chemical equilibrium using a modified form of the NASA CEA program available online [28]. The Gibbs free energy per kilogram of a mixture of N species is defined as

$$G = \sum_{j=1}^{N} \mu_j n_j \tag{1}$$

Here μ_j is the chemical potential per kg-mol and n_j is the number of moles of the j^{th} species, respectively. Using a descent Newton-Rhapson method, Eq. (1) is minimized, subject to mass and charge balance constraints. The chemical potential of species j is given by

$$\mu_j = H_j^o(T) - TS_j^o(T) + RT\ln\left(\frac{n_j}{n}\right) + RT\ln\left(\frac{p}{p^o}\right) \tag{2}$$

In Eq. (2), *R* is the universal gas constant, *T* is the equilibrium temperature of the gas mixture in Kelvin, and p/p^o is the ratio of the mixture pressure to the reference pressure. Finally, $H_j^o(T)$ is the standard enthalpy and $S_j^o(T)$ is the standard entropy of species j at temperature *T*, respectively. Thermochemical properties of many individual species are available in the JANNAF tables for temperatures up to 6,000 K. Data from the fourth edition of the JANNAF tables [29] are included in the CEA program in the form of least squares fits, and were used in the present work. In this edition, the reference pressure is stated as 1 bar for all species and we choose to use 1 bar as the assigned mixture pressure, eliminating the final term in equation (2). These fits are provided in seven coefficients (a_{1-7}) and two integration constants ($b_{1,2}$) of the form

$$\frac{H_j^o}{RT} = -a_1T^{-2} + a_2T^{-1}\ln(T) + a_3 + \frac{a_4}{2}T + \frac{a_5}{3}T^2 + \frac{a_6}{4}T^3 + \frac{a_7}{5}T^4 + \frac{b_1}{T} \tag{3a}$$

$$\frac{S_j^o}{R} = -\frac{a_1}{2}T^{-2} - a_2T^{-1} + a_3\ln(T) + a_4T + \frac{a_5}{2}T^2 + \frac{a_6}{3}T^3 + \frac{a_7}{4}T^4 + b_2 \tag{3b}$$

For most species, fits were provided for two temperature intervals, 200-1,000 K and 1,000-6,000 K. The higher temperature fit was extrapolated for use in the present work. The data fits were used directly for all available species in these temperature intervals. The monatomic species also had fits provided for the 6,000-20,000 K interval, which were used directly in that temperature interval, and linearly extrapolated to 40,000 K. Data from a separate model were included in the program for the doubly-ionized species, which are not included in the JANNAF tables. For ideal ions the thermochemical properties can be related to the partition function Q by [10]

$$\frac{H_j^o}{RT} = T\frac{d(\ln Q)}{dT} + \frac{5}{2} + \frac{H_0^o}{RT} \tag{4a}$$

$$\frac{S_j^o}{R} = T\frac{d(\ln Q)}{dT} + \ln Q + \frac{3}{2}\ln M + \frac{5}{2}\ln T + \frac{5}{2} + \ln\left[k\left(\frac{2\pi k}{N_A h^2}\right)^{\frac{3}{2}}\right] \tag{4b}$$

where the partition function can be written as the sum of the translational and electronic contributions as [30]

$$Q = Q_{tr} + Q_{el} = V\left(\frac{2\pi mkT}{h^2}\right)^{\frac{3}{2}} + \sum_{i=0}^{2} g_i \exp\left(-\frac{\Theta_i}{kT}\right) \tag{5}$$

Here, the electronic state degeneracies (g_i) and ionization energies (Θ_i) were obtained from the NIST atomic spectra database [31]. Equations (4) and (5) were used to generate date in the same form as presented in the JANNAF tables. A reduced form of equation (3) with all coefficients set equal to zero except a_3, b_1, and b_2 is then fit to the thermodynamic data for only these doubly ionized species. The resulting fit is similar in shape to the provided fit for electron gas and singly-ionized species. This fitting process is achieved by use of a multiple non-linear regression algorithm to generate values for the three least-squares coefficients.

2.2. THERMODYNAMIC PROPERTIES

Thermodynamic properties such as density, enthalpy and specific heat of a vapor mixture are typically calculated using statistical mechanics. Knowledge of the mixture temperature and pressure is combined with thermochemical properties of the component species to calculate these properties. The details of this method may be found in numerous publications. In the present work, the method detailed in Gordon et al. [32] and integrated within the NASA CEA program is used to calculate the mixture enthalpy and specific heat. We summarize the process used in the following paragraphs. The enthalpy h of a mixture of N gases may be written as

$$h = \sum_{j=1}^{N} \chi_j H_j^o \tag{6}$$

Here χ_j are the mole fractions of each species and are multiplied by the species enthalpy at a given temperature. Again, the source of the calculated species enthalpy at a given temperature depends upon the type of species. Polyatomic species data are obtained from fits in Eq. (3a) for up to 6,000 K; monatomic species are fit to 20,000 K. For ideal ions the enthalpy is approximated by Eq. (4a).

Calculation of the specific heat is split into two calculations for the frozen and chemical reaction contributions. The mixture frozen specific heat $C_{p,fr}$ is determined similarly to enthalpy by

$$C_{p,fr} = \frac{1}{M} \sum_{j=1}^{N} \chi_j C_{p,j}^o \tag{7}$$

Here M is the mixture molar mass and $C_{p,j}^o$ are each species specific heats which may be determined with a seven term least squares fit of the form

$$\frac{C_{p,j}^{o}}{R} = a_1T^{-2} + a_2T^{-1} + a_3 + a_4T + a_5T^2 + a_6T^3 + a_7T^4 \tag{8}$$

which are included in the CEA program using the same terms as in Eq. (3). The specific heat of each species is largely dependent on the species temperature and number density, and the fit differs between monatomic and polyatomic species due to vibrational and rotational modes. The reaction contribution to the mixture specific heat, $C_{p,re}$, is dependent on the heat of reaction for each dissociation or ionization reaction within the mixture. This quantity may be calculated similar the frozen contribution like so

$$C_{p,re} = \frac{R}{M}\sum_{j=1}^{N}\chi_j\left(\frac{\Delta H_j^r}{RT}\right) \tag{9}$$

In Eq. (9), the ΔH_j^r terms are the change in enthalpy for each of the included dissociation and ionization reactions. Finally, the desired total specific heat, C_p, of the gas mixture at constant pressure may be calculated by summing the results of equations (7) and (9). The above calculations are carried out numerically as detailed by Gordon et al. [32].

2.3. PROPELLANT COMPOSITION

Accurate prediction of the chemical composition requires careful consideration of the constituent species used to model each of the propellants. Here the selected species and relative weights input to the thermochemical model are described. The PTFE samples in this work are purely polytetrafluoroethylene, a non-conductive polymer. Thermal degradation of this polymer is characterized by the “unzipping” of the chain into the monomer, in this case C_2F_4. Using thermogravimetric analysis (TGA) coupled with

Fourier-transform infrared spectroscopy (FTIR), Schild [33] observed almost exclusive production of C_2F_4 during thermal degradation of PTFE. For our thermochemical model, we have selected to define the constituent species of PTFE vapor as 100% C_2F_4 by weight, as shown in Table 1.

Table 1: Selected model constituent species and mass fractions for each propellant.

Material	Constituent Species Name	Chemical Formula	Relative Weights	Molar Mass, g/mol
PTFE	Tetrafluoroethylene	C_2F_4	1.0000	100.02
HIPEP	Nitric Acid	HNO_3	0.4921	63.01
	Hydroxylamine	NH_2OH	0.2579	33.03
	Acetaldehyde	CH_3CHO	0.2000	44.05
	Ammonium Nitrate	NH_4NO_3	0.0500	80.04

HIPEP is a mixture of more complex species and care must be taken when selecting the constituent species used in the model. HIPEP is a HAN-based solution solid manufactured by Digital Solid State Propulsion (DSSP) using green ingredients and processes free of harmful fumes. It is mixed in liquid form in standard chemical glassware, with only gloves and safety glasses needed for protection. The mixture then cures at warm room temperature (35°C/95°F), forming a soft solid with the appearance and texture of a red or pink fruit gum candy. HIPEP has a chemical composition of 75% HAN oxidizer (an inorganic ionic liquid), 20% polyvinyl alcohol (PVA) fuel/binder, and 5% ammonium nitrate additive [19]. The thermodynamic properties of the primary constituent, HAN, in vapor form are not well known because the material does not evaporate like PTFE and many other materials. What is known, however, is that solid and aqueous HAN undergoes a thermal decomposition process at temperatures above 400 K. Lee and Litzinger [34] conducted a thermal degradation experiment with aqueous solutions of HAN and found that a proton transfer reaction producing hydroxylamine (NH_2OH) and nitric acid (HNO_3) initiates thermal decomposition. The timescale for this initiation reaction was estimated to be on the order of 10^{-10} seconds, while the subsequent reaction between nitric acid and hydroxylamine was much slower ($>10^{-5}$ s). A typical arc ablation current pulse has a period on the order of 10^{-6} seconds, which means the initiation reaction occurs on a timescale short enough for these species to dominate the plume composition. Because the propellant undergoes this decomposition to transition to the vapor phase in which we are interested, these two species were chosen (in relative weights equivalent to 75% HAN) to model the main constituent of the HIPEP material. The fuel binder, PVA (CH_2CHOH), is a synthetic polymer and water-soluble. Like HAN, the thermochemical properties of PVA vapor are not well known, as the material is typically in solid or aqueous form. At room temperature, acetaldehyde (or "ethanal") is a more stable form of the molecule with a mobile proton and has the idealized formula of CH_3CHO. We have selected to use this material to model the PVA constituent. The final 5% of the ammonium nitrate in the HIPEP material is modeled using the known properties of ammonium nitrate, NH_4NO_3. The chosen constituent species and their relative weights for the HIPEP material model are shown in Table 1.

3. MODEL VALIDATION

First, the thermal degradation temperature for PTFE and HIPEP are examined using experimental data. Second, the results obtained using the described thermochemical model for polytetrafluoroethylene are compared to the works of other researchers using similar methods. Third, results for HIPEP at a single low temperature are compared to other researchers' results at that temperature using similar methods. These comparisons illustrate the accuracy of the model presented here relative to other models presented in the literature.

3.1. THERMAL DEGRADATION TEMPERATURE

The upper bound of the temperature range in the thermochemical model in the present work was chosen as the upper end of electron temperatures typically measured in PPT plumes, i.e. 1-3 eV [8]. Selection of the lower bound requires more careful consideration. If the lower bound is chosen below the vaporization temperature of the material, the Gibbs minimization method may not converge. In cases where it will converge, the theoretical results obtained would be meaningless in the consideration of a real vapor. The present work thus included a brief study of the thermal degradation temperature (i.e. the temperature that incites vapor production) for the materials considered using thermogravimetric analysis.

Thermogravimetric analysis (TGA) is a material science technique wherein the weight of a small material sample is measured during heating of the sample. In our tests, the heating rate (K/min) is held at a predetermined constant rate for the duration of the test, and sample weight is measured over time. Results are typically presented in terms of measured weight percent with respect to temperature and/or the derivative of sample weight versus temperature. In the present work, the Q50-TGA model from TA Instruments was employed, which has a maximum mass balance capacity of 1000 mg and sensitivity of 0.1 μg. PTFE and HIPEP were tested in the apparatus with sample sizes varying between 10 and 20 mg. These samples were cut into 3-10 thin pieces 2 or 3 mg in mass to maximize the surface area-to-mass ratio, allowing even heating and evaporation. After a system tare with a platinum platter and 90 μL alumina crucible was complete, a sample was loaded into the crucible. Nitrogen gas was delivered by a separate gas inlet tube such that the sample was contained in an inert environment at atmospheric pressure for the duration of the test. After each experiment and data collection, the sample cup was removed from the system and remaining sample was collected. All PTFE tests resulted in complete decomposition and no remaining sample. HIPEP tests produced a black solid of 10%-20% the original sample weight. The exact composition of the residual solid is currently unconfirmed, but is suspected to be largely carbon.

Figure a presents the TGA curves for two samples of PTFE tested in the present work. Also plotted are results from Hondred et al.[35] for two samples of PTFE analyzed using TGA. There is a clear separation between onset temperature (where sample weight begins to decrease) and full thermal degradation (sample weight is zero) for PTFE TGA curves, indicating a rapid, single-step degradation. Further, the TGA curve is shifted to higher temperatures for increased heating rate. Comparison of our results with that in literature shows agreement within 3% for both heating rates.

Figure b shows the TGA curves for three samples of HIPEP. While there are no TGA data available for the HIPEP material in literature, data for aqueous HAN (called HAN N, 75% HAN, 25% H_2O) from Hoyani et al. [36] are also plotted here. The HAN N solution has a lower onset temperature than the HIPEP samples, but the main stage of thermal degradation for both materials occurs at a similar temperature of about 470 K. Both HIPEP and the HAN N solution of Hoyani et al. [36] exhibit a decrease in weight with increasing temperature for temperatures less than 470 K. This is due to the presence of and evaporation of water from the samples. HIPEP is known to be hygroscopic, absorbing 1-5% by mass of water from the atmosphere at typical laboratory humidity levels (~50%) [21], and the weight of HIPEP has decreased by about 5% when degradation begins at 470 K. The HAN N solution is 25% water and its weight has decreased by about 25% when degradation begins at 470 K. The final weight of HIPEP samples is greater than zero (~18%), indicating the samples do not completely degrade. A multiple-step degradation model is suggested by the TGA curve shape below 60%. This is marked by an endothermic reaction causing a decrease in temperature during the final stages of thermal degradation of HIPEP, between 450 and 500 K. This endothermic reaction is also observed in the same temperature range in the HAN data of Hoyani et al. [36]. The degradation curve of PTFE is smooth indicating a single-step degradation, whereas the degradation region of the curve for HIPEP has non-constant slope, indicating multiple steps in the degradation process.

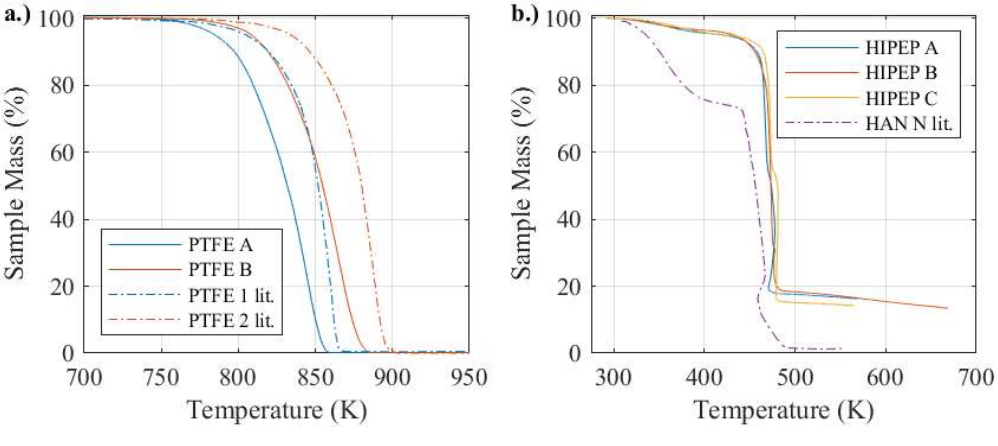

Figure 1: Thermogravimetric analysis curves for samples of a.) PTFE and b.) HIPEP.

The derivative of sample weight with respect to temperature was also examined to determine thermal degradation temperature. Specifically, we report the temperature of the inflection point at the maximum change in sample weight per unit change in temperature (i.e. the temperature at which sample mass is changing fastest). This temperature will be referred to as the degradation temperature. Table 2 presents the degradation temperature for each of the five samples tested using TGA along with results from literature.

Table 2: Onset and degradation temperature from thermogravimetric analysis.

Sample	**Initial mass, mg**	**Heating rate, K/min**	**Onset Temp., K**	**Degradation Temp., K**
PTFE A	22.78	10	758	844
PTFE 1 lit. [35]	25.00	10	763	858
PTFE B	21.76	20	777	864
PTFE 2 lit. [35]	25.00	20	783	888
HIPEP A	21.54	10	430	468
HIPEP B	9.79	10	419	473
HIPEP C	20.15	20	438	473
HAN N lit. [36]	10.00	10	445	471

Despite the observation of a multi-step degradation of HIPEP, the variation in degradation temperature is less than 5 K for the three samples tested. The degradation temperature of HIPEP is about 473 K, compared to the 850 K degradation temperature of PTFE. Onset and thermal degradation temperatures increase with heating rate for PTFE as seen in our results as well as in literature. This is not true for HIPEP. The results of the PTFE testing are consistent with existing literature, and deviations of less than 3% in temperature could be attributed to the use of air as background gas in the literature results, instead of the inert nitrogen environment used in the present work. Our measurement of degradation temperature for HIPEP is only 2 K different from an aqueous HAN sample tested in literature. However, HIPEP samples do exhibit an onset temperature of up to 26 K lower than the HAN. Based on these measurements, the low temperature bounds for PTFE and HIPEP were chosen as 900 K and 500 K, respectively.

3.2. CHEMICAL COMPOSITION OF PTFE VAPOR

Using the described thermochemical modeling approach, the mole fractions of 19 gaseous chemical species were determined as a function of the equilibrium vapor temperature. One mole of propellant vapor was assumed in this analysis to be comprised entirely of the C_2F_4 molecule as shown in Table 2, and the mole fractions were then converted to number densities and are displayed in Figure 2 for the temperature range of 900-40,000 K.

From Figure 2, at low temperatures less than 2,000 K, the vapor is dominated by CF_4 and C_2F_2 species. Dissociation of the monomers into C_x, CF_x, F_2, and then subsequently into atomic C and F species, is rapid in the 2,000-4,000 K regime. Above 4,000 K these atomic neutrals are dominant, and the vapor is nearly fully dissociated. The ionization energy of the Carbon atom is 11.26 eV compared to 17.42 eV for Fluorine. Thus, the onset of C^+ occurs around 8,000 K and peaks at 13,000 K compared to the higher onset at 10,000 K and peak at 17,500 K for F^+. With the increase in ionized species, the electron density predictably increases to a value of $\sim 4\times10^{23}$ m^{-3} at around 21,000 K and increases only marginally with increased temperature. At high temperatures above 21,000 K (~2 eV) the vapor is a strongly ionized plasma dominated by charged species C-II, F-II, C-III, F-III and electrons. Further increase in temperature to 40,000 K results in increased densities of the doubly ionized species and electrons, corresponding to decreased singly ionized species densities.

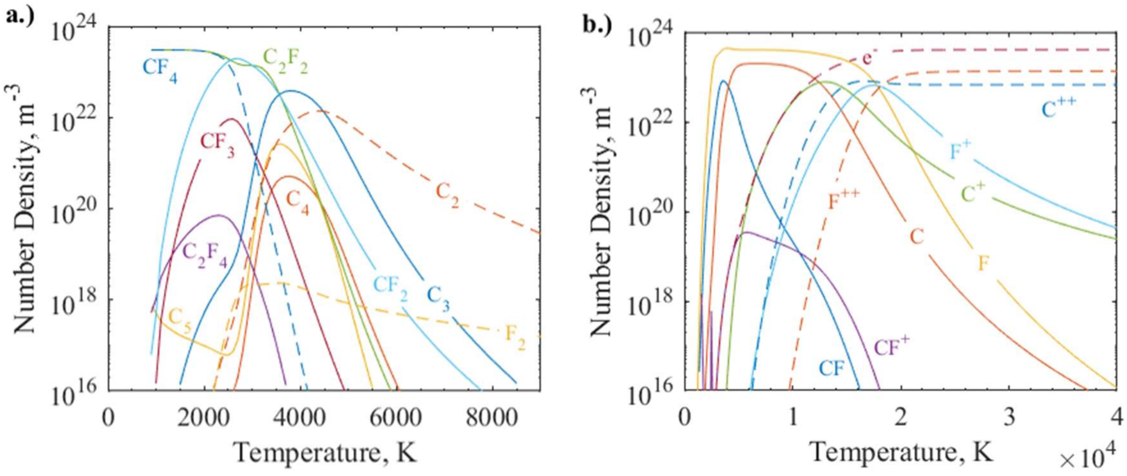

Figure 2: Equilibrium composition of PTFE vapor at 1 bar pressure as a function temperature organized by a.) polyatomic and b.) atomic/ionic species.

To verify the regimes observed in the results from our model, we have compared to those presented in literature. The low temperature regime (<2,000 K) was shown to be dominated by CF_4 and C_5 by two other models [1, 12]. In our model, C_5 is replaced by C_2F_2 but the vapor is also dominated by CF_4. Both models then show that dissociation leads to rapid increases in CF_2, CF, and atomic F above 2,200 K. Zhang et al. [1] shows F as the dominant species between ~3,500 K to the 7,000 K maximum temperature examined, with CF and C prevalent within this regime. The present work shows a dissociation regime very similar to this for PTFE vapor. H. Wang et al. [12] states that atomic fluorine is the most dominant species between 3,200 and 16,000 K, which is also observed in Figure 2. Further agreement with H. Wang et al. is observed for temperatures of 20,000 to 40,000 K where electrons are the most abundant species, followed by singly- and doubly-ionized carbon and fluorine. Kovitya [10] also reported predictions of ionization of C and F occurring at ~15,000 K with electrons and these ions dominating the vapor up to 30,000 K. In summary, the model presented here agrees well with the reported literature on the thermochemical composition of PTFE vapor.

3.3. LOW TEMPERATURE HIPEP COMBUSTION

Previously, a thermochemical model was developed and used to predict the equilibrium combustion temperature and product species of a variant of the HIPEP material [22]. As this is the only other known application of such a model to this material, it is prudent to compare with those results. The predicted mass fractions of the five most prevalent species are compared between the previous model [22] and the model presented here. The previous model results are only available for 700 K and are presented in Table 3. Qualitative agreement within 10% is observed, the five most abundant species are identical, and the relative order of abundance is nearly identical.

Table 3: Comparison of predicted HIPEP composition at 700 K for two thermochemical models.

Species	**Sawka & McPherson [22] Mass Fraction**	**This Work Mass Fraction**
H_2O	43.62%	37.84%
CO_2	29.30%	36.32%
N_2	24.22%	23.62%
CO	1.07%	0.42%
H_2	0.11%	0.72%

The model presented here matches within 1% for N_2, CO, and H_2, though the order of abundance for CO and H_2 is reversed. While both models predict H_2O and CO_2 as the most and second-most abundant species, our model predicts ~7% more CO_2 by mass, and is the largest discrepancy between the two results. Our model also predicts 5.8% less H_2O than the previous model. It is noted that our lower predicted mass fraction of H_2O may be attributed to the hygroscopic nature of the propellant, which we have ignored in the present work. Samples of HIPEP are known to absorb 1-5% mass of water from the atmosphere if the relative humidity is at typical laboratory levels (~50%) [21]. It is unknown if Sawka and McPherson included this absorbed moisture in their analysis.

4. RESULTS AND DISCUSSION

Results from the model are presented with discussion of the significance. First, the chemical composition of the electric solid propellant vapor is detailed. Discussion of the predicted thermodynamic properties follows. Finally, a brief discussion of the observed trends in results is presented.

4.1. CHEMICAL COMPOSITION OF HIPEP VAPOR

Using the propellant makeup model detailed in Table 1, the thermochemical model was applied to determine the equilibrium mole fractions of 22 gas species comprising HIPEP vapor for a range of temperatures. The results of this prediction were converted to number density for one mole of vapor, and are shown in Figure 3 for the temperature range of 500-40,000 K.

The general trends observed for PTFE hold for the predicted species in HIPEP vapor. At low temperatures below 3,000 K the vapor is dominated by the polyatomic species of H_2O, N_2, CO_2, and H_2. Above 3,500 K the dissociation of CO_2 incites an increase in the fraction of CO molecules, and H_2 is dissociated into atomic hydrogen. In the 5,000 to 10,000 K regime the vapor is largely comprised CO, N_2, N, H, and O. Further dissociation of CO and N_2 occurs in the 10,000 to 15,000 K regime in addition to ionization of H^+ and the coinciding increase in electron density. Above 18,000 K the HIPEP vapor is entirely dissociated and made up entirely of monatomic and ionic species. Ionization (and electron density) increases with further increase in temperature. At high temperatures of 25,000 K or more, the HIPEP vapor is strongly ionized and comprised of mainly single protons and electrons in addition to large populations of O-III, N-III, and C-III.

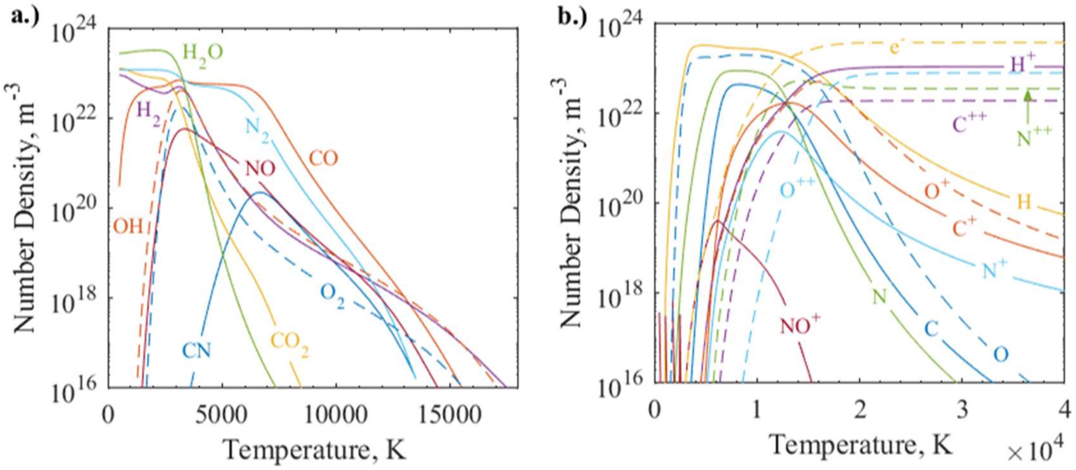

Figure 3: Equilibrium composition of HIPEP vapor at 1 bar pressure as a function of temperature organized by a.) polyatomic and b.) atomic/ionic species.

4.2. THERMODYNAMIC PROPERTIES

Using the approach detailed by Gordon et al. [32] and included in the NASA CEA program, the mixture enthalpy and specific heat at constant pressure of both HIPEP and PTFE vapor were determined. The calculation of the mixture enthalpy is entirely dependent on individual species enthalpy and is further influenced by chemical reactions. All species possess a translational energy component of enthalpy which is proportional to kT. Thus, a monotonic increase in enthalpy is observed in Figure 4 for both material vapors. Additionally, a large positive gradient is observed in the 12,000 to 20,000 K regime for both material vapors. In this region, ionization reactions are prominent. Increasing electron population greatly increases the translational energy contribution to enthalpy, and large gradients in electronic partition functions yield increased enthalpy for the forming ionic species. Above 20,000 K, these reactions reduce in abundance, electron and ion densities remain largely constant, reducing the enthalpy profile to a nearly linear proportionality with temperature. Some other thermochemical models show an additional gradient in enthalpy for PTFE vapor with further increase in temperature [12]. The present work differs in that we do not consider the third ionization reactions for C and F, which begin at about 28,000 and 35,000 K, respectively. These reactions increase enthalpy non-linearly in this regime. As a result, our calculation increasingly underestimates enthalpy (up to 20% at 40,000 K) when compared with literature results for PTFE at temperatures above 30,000 K. Further, our calculation overestimates enthalpy in the range of 18,000 to 28,000 K by a maximum of 40% at 20,000 K. This is attributed to increased contribution of additional vibrational and rotational energy modes in the singly and doubly ionized species. Excellent agreement with Zhang et al. [1], Kovitya [10], and Wang et al. [12], is found at temperatures below 18,000 K for PTFE vapor.

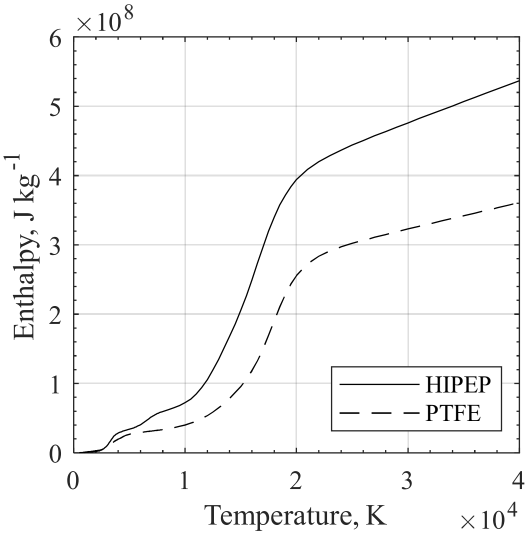

Figure 4: Mixture enthalpy of HIPEP and PTFE vapors as a function of equilibrium temperature.

The specific heat at constant pressure of HIPEP and PTFE vapors are shown in Figure 5. As the specific heat of each species is defined as the derivative of enthalpy with respect to temperature, the features of the total specific heat profile follow the mixture enthalpy. Chemical reactions also contribute to rapid changes in specific heat with temperature. The peaks in specific heat between 2,000 K and 10,000 K for both vapors are the result of the numerous dissociation reactions that take place in this regime. Specific heat fluctuates from 10^3-10^4 J/kg/K for both vapors in this regime with multiple minimums and maximums. These extrema correspond with rapid changes observed in the mixture enthalpy in this regime which are observed in Figure 4. A tall and broad peak exists for both material vapors in the region between 12,000 K and 20,000 K in Figure 5. This peak corresponds to the rapid increase in mixture enthalpy as a result of rapid ionization. For our calculation temperature range, the absolute maximum for both material vapors is observed in this region. In the high temperature regime (>25,000 K) minimal change with temperature is observed in our calculation of specific heat for each material vapor. This is due to the near linear increase of enthalpy with temperature here and is a major difference in our results compared with literature for PTFE. Again, this is a direct result of our exclusion of C^{3+} and F^{3+}. Comparison with Kovitya [10] shows agreement within 10% up to 12,000 K for PTFE vapor, and a nearly identical maximum location (18,000 K), but a peak value a factor of about 2 greater. Figure 5 also matches closely with that of Zhang et al. [1] for temperatures less than 12,000 K, but the height of the primary peak is a factor of 4 greater. The large discrepancy in the 12,000-20,000 K regime is due to the present model's overprediction of enthalpy resulting from exclusion of triply ionized C and F as discussed with the mixture enthalpy.

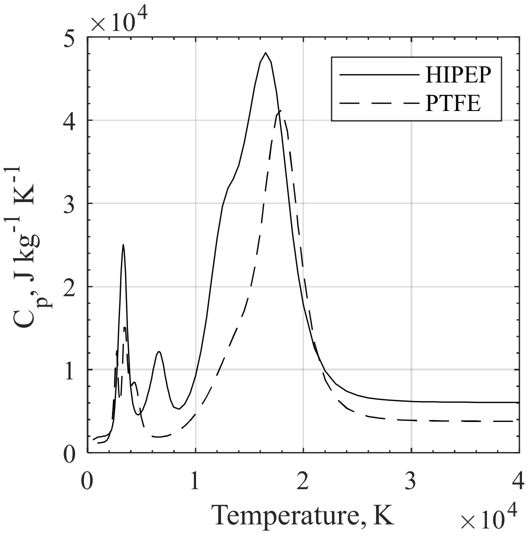

Figure 5: Specific heat at constant pressure of HIPEP and PTFE vapors as a function of equilibrium temperature.

Previous experimental work with the HIPEP material has focused on its differences from PTFE when used as propellant in pulsed plasma thrusters. Figure 4 and Figure 5 show similar trends in the thermodynamic properties between the materials, but clear differences in magnitude are observed. Enthalpy of the materials are within ~10% for temperatures less than 5,000 K, but differ increasingly with temperature up to a factor of ~1.5 at 40,000 K, with HIPEP enthalpy always greater. The increased enthalpy of HIPEP can be attributed to the additional species available for ionization (e.g. H, N, O) compared to PTFE (e.g. only C and F). As a result, the peaks of HIPEP vapor specific heat are greater in magnitude than PTFE. Specifically, the primary peak of HIPEP specific heat is 16% greater than the absolute maximum for PTFE. This peak is located at 16,500 K for HIPEP vs. 18,000 K for PTFE. The shift to lower temperature is due to the ionization of H, N, and O, all of which ionize at lower temperature than F.

5. CONCLUSIONS

A thermochemical model was developed describing the composition and thermodynamic properties of an electric solid propellant vapor under equilibrium conditions. This model used the minimization of Gibbs free energy method to yield mole fractions of 22 individual gaseous species as a function of the equilibrium temperature. Statistical mechanics were employed to calculate the enthalpy and specific heat at constant pressure of the predicted gas mixture. This approach was also employed for PTFE vapor, and results were compared to those available in published literature. Results agree with multiple literature sources in terms of the dominant equilibrium species with respect to temperature. Thermodynamic property results also were found to agree closely for temperatures up to 12,000 K, and similar trends observed at higher temperatures.

In the low temperature regime, the vapor of the electric solid propellant HIPEP is dominated by polyatomic species H_2O, N_2, CO_2, CO, and H_2. The mass fractions of these species predicted by the model match within 10% to another researcher's predictions for an earlier formulation of the material at 700 K. Dissociation dominates between 3,500 K and 10,000 K, above which protons and electrons are formed from ionization of atomic hydrogen. Above 18,000 K HIPEP vapor is fully dissociated and weakly ionized. Strong ionization occurs above 25,000 K, with C, N, and O ions in the second ionization state mixed with free protons and electrons.

Thermodynamic property calculations indicate that HIPEP vapor has similar enthalpy to PTFE vapor at low temperature (<5,000 K), but much greater enthalpy at higher temperatures where ionized species are prominent. Previous experimental results suggest that for a given energy in an ablation-controlled arc discharge, HIPEP ablates more material than PTFE due to lower vaporization temperature and solid material specific heat. The results here indicate HIPEP vapor requires greater energy to raise to 1-2 eV (11,600-23,200 K) in temperature than PTFE vapor. In the case of application to pulsed plasma thruster performance, this is an indicator of reduced efficiency regarding stored energy. In the case of limited arc energy, HIPEP vapor will be heated to a lower plasma temperature than PTFE vapor. Reduction of temperature in the electrothermal device leads to reduction in the plume velocity and thus the efficiency of the device.

ACKNOWLEDGEMENTS

M.S. Glascock is extremely grateful for the NASA Space Technology Research Fellows program, which funded this research under grant number NNX15AP31H. The authors thank Dr. John Yim at NASA Glenn Research Center for assistance with the CEA program and fruitful discussion on the work. The authors thank Digital Solid State Propulsion, LLC for HIPEP samples for TGA, as well as previous thermochemical modeling work on the material. Thermogravimetric analysis of propellant samples was carried out in the Materials Research Laboratory Central Research Facilities, University of Illinois. In particular, the authors wish to thank Lou Ann Miller and Tim Spila at this lab for their assistance with this analysis.

REFERENCES

[1] Zhang J. L., Yan J. D., Murphy A. B., Hall W. and Fang M. T. C. 2002 *IEEE Trans. Plasma Sci.* **30** 706

[2] Seeger M., Tepper J., Christen T. and Abrahamson J. 2006 *J. Phys. D: Appl. Phys.* **39** 5016

[3] Kovitya P. and Lowke J. J. 1984 *J. Phys. D: Appl. Phys.* **17** 1197

[4] Hong D. e. a. 2000 *Rev. Sci. Instrum.* **71** 15

[5] Wang Z. B., Hong M. H., Lu Y. F., Wu D. J., Lan B. and Chong T. C. 2003 *J. Appl. Phys.* **93** 6375

[6] Keidar M., Boyd I. D. and Beilis I. I. 2000 *IEEE Trans. Plasma Sci.* **28** 376

[7] Wang Y., Ding W., Cheng L., Yan J., Li Z., Wang J. and Wang Y. 2017 *IEEE Trans. Plasma Sci.* **45** 2715

[8] Burton R. L. and Turchi P. J. 1998 *J. Propul. Power* **14** 716

[9] Zhang Z., Ling W. Y. L., Tang H., Cao J., Liu X. and Wang N. 2019 *Rev. Mod. Plasma Phys.* **3** 5

[10] Kovitya P. 1984 *IEEE Trans. Plasma Sci.* **12** 38

[11] Keidar M., Fan J. and Boyd I. D. 2001 *J. Appl. Phys.* **89** 3095

[12] Wang H., Wang W., Yan J. D., Qi H., Geng J. and Wu Y. 2017 *J. Phys. D: Appl. Phys.* **50** 395204

[13] Zaghloul M. R. 2004 *J. Appl. Phys.* **95** 3339

[14] Keidar M., Boyd I. D. and Beilis I. I. 2001 *J. Phys. D: Appl. Phys.* **34** 1675

[15] Keidar M., Boyd I. D. and Beilis I. I. 2003 *J. Propul. Power* **19** 424

[16] Schönherr T., Komurasaki K. and Herdrich G. 2013 *J. Propul. Power* **29** 1478

[17] Antonsen E. L., Burton R. L., Reed G. A. and Spanjers G. G. 2005 *J. Propul. Power* **21** 877

[18] Keidar M., Boyd I. D., Antonsen E. L., Gulczinski III F. S. and Spanjers G. G. 2004 *J. Propul. Power* **20** 978

[19] Glascock M. S., Rovey J. L., Williams S. and Thrasher J. 2017 *J. Propul. Power* **33** 870

[20] Glascock M. S. 2016 *M.S. Thesis* Missouri University of Science and Technology

[21] Glascock M. S., Rovey J. L. and Polzin K. A. 2019 *J. Propul. Power* 1 Online July 2019

[22] Sawka W. N. and McPherson M. 2013 *49th Joint Propulsion Conference* AIAA Paper 2013-4168

[23] Sawka W. N. and Grix C., US Patent No. 8317953B2 (November 27, 2012).

[24] Baird J. K., Lang J. R., Hiatt A. T. and Frederick R. A. 2017 *J. Propul. Power* **33** 1589

[25] Hiatt A. T. and Frederick R. A. 2016 *52nd AIAA/SAE/ASEE Joint Propulsion Conference* AIAA Paper 2016-4935

[26] Sawka W. N. and Grix C., US Patent No. 8857338B2 (October 14, 2014).

[27] Gordon S. and McBride B. J. 1994 *NASA Reference Publication 1311*

[28] McBride B. J. and Gordon S. https://www.grc.nasa.gov/www/CEAWeb/

[29] Chase M. W. 1998 *Physical and Chemical Reference Data*

[30] Vincenti W. G. and Kruger C. H. 1965 *Introduction to Physical Gas Dynamics* (Malabar, FL: Krieger Publishing Co.) pp. 122-131

[31] Kramida A., Ralchenko Y. and Reader J. 2018 *NIST Atomic Spectra Database (ver. 5.5.6)*

[32] Gordon S., McBride B. J. and Zeleznik F. J. 1984 *NASA TM-86885*

[33] Schild H. G. 1993 *J. Polym. Sci., Part A: Polym. Chem.* **31** 1629

[34] Lee H. and Litzinger T. A. 2003 *Combust. Flame* **135** 151

[35] Hondred P. R., Yoon S., Bowler N. and Kessler M. R. 2013 *High Perform. Polym.* **25** 535

[36] Hoyani S., Patel R., Oommen C. and Rajeev R. 2017 *J. Therm. Anal. Calorim.* **129** 1083

III. IMPULSE MEASUREMENTS OF ELECTRIC SOLID PROPELLANT IN AN ELECTROTHERMAL ABLATION-FED PULSED PLASMA THRUSTER

Matthew S. Glascock,

Missouri University of Science and Technology, Rolla, MO 65409

Joshua L. Rovey,

University of Illinois at Urbana-Champaign, Urbana IL 61801

and

Kurt A. Polzin

NASA Marshall Space Flight Center, Huntsville, AL

ABSTRACT

Electric solid propellants are advanced solid chemical rocket propellants that can be controlled (ignited, throttled and extinguished) through the application and removal of an electric current. These propellants are also being considered for use in the ablative pulsed plasma thruster. In this paper, the performance of an electric solid propellant operating in an electrothermal ablation-fed pulsed plasma thruster was investigated using an inverted pendulum micro-Newton thrust stand. The impulse bit and specific impulse of the device using the electric solid propellant were measured for short-duration test runs of 100 pulses and longer-duration runs to end-of-life, at energy levels of 5, 10, 15 and 20 J. Also, the device was operated using the current state-of-the-art ablation-fed pulsed plasma thruster propellant, polytetrafluoroethylene or PTFE. Impulse bit measurements for PTFE indicate 100±20 μN-s at an initial energy level of 5 J, which increases linearly by ~30 μN-s/J with increased initial energy. Measurements of the impulse bit for the electric solid

propellant are on average lower than PTFE by 10% or less. Specific impulse for when operating on PTFE is calculated to be about 450 s compared to 225 s for the electric solid propellant. The 50% reduction in specific impulse is due to increased mass ablated during operation with the electric solid propellant relative to PTFE.

1. INTRODUCTION

Recent innovations in the solid rocket propellant field have led to the development of a solid propellant that is safe, throttleable, and green with on-demand on-off capability. These electric solid propellants (ESP's) ignite and decompose when electric power is applied at sufficient current and voltage [1]. This decomposition is a highly exothermic process that generates hot gas at a burn rate that can be throttled by varying the applied current. Removal of the voltage and current extinguishes the reaction, which may be restarted by reapplication of electric power [2]. Because this reaction is only induced by electric current, ESPs are not susceptible to accidental ignition by spark, impact or open flame. These characteristics are extremely beneficial compared to traditional solid rocket propellants which are not throttleable, toggleable, or insensitive to external ignition sources. The advent of ESPs expands the potential applications for solid propellants that were previously infeasible.

Development of ESPs began in the 1990's with the design of an automobile air bag inflator propellant (ABIP) using materials safe for unprotected human contact (i.e., "green" materials). This ABIP was ammonium nitrate-based and was later repurposed for use in other areas, including rocket propulsion. Shortly thereafter, "ASPEN," the first digitally controlled extinguishable solid propellant, was developed [3]. This propellant featured additives with the ammonium nitrate base to lower melting point and increase electrical conductivity [2]. This material exhibited performance metrics comparable to that of previous solid rocket propellants, but major problems existed with the repeatability of ignition. Further development for gas-generation applications led to a special family of electrically controlled energetic materials which may be mixed as either solid, liquid or gel form propellants, all of which are electrically ignitable [4, 5]. Some mixtures are flame-sensitive and explosive, some insensitive to flame and sustainable, some are insensitive and extinguishable (like ESPs). One particular formula which conducts electricity and exhibits high specific impulse is known as the high performance electric propellant, or HIPEP [1, 6], which is not sensitive to open flame, spark, or impact and is extinguishable. In this solid energetic material, the ionic liquid oxidizer hydroxyl-ammonium nitrate (HAN) is dissolved and cross-linked in polyvinyl alcohol (PVA), forming a gel that is hardened by baking. The resulting rubbery solid HIPEP exhibits a pyroelectric behavior unique to energetics. When direct current electric power is applied, the proton transfer reaction between hydroxyl-ammonium and nitrate is promoted, and the level of nitric acid rapidly rises in the material eventually triggering ignition of the propellant. This exothermic, gas-generating reaction may be harnessed in a solid rocket motor to generate thrust on demand using electric power.

HIPEP's pyroelectric behavior may facilitate a dual mode propulsion system using the solid propellant. The first mode is a high thrust chemical mode where direct current electric power is applied to incite pyroelectric gas generation. This propellant is gas-dynamically accelerated through a nozzle to generate thrust like any typical solid rocket motor. The duration of each chemical mode fire is determined by the duration that electric power is supplied and could be ~500 ms. The inventors of this propellant and collaborating groups have reported on this mode of operation previously, with some ongoing efforts [7-9]. This solid rocket motor may be paired with a second, high specific impulse (I_{sp}) electric mode in the same device using the same thruster and solid propellant with a second electrical circuit configuration. One promising electric configuration for a high I_{sp} mode is a pulsed electric propulsion device known as the coaxial ablation-fed pulsed plasma thruster (APPT).

Pulsed plasma thrusters [10] (PPTs) have been in use since the first orbital flight of an electric propulsion device in 1964. PPTs offer repeatable impulse bits with higher exhaust velocities than can be achieved using chemical thrusters. Ablating polytetrafluoroethylene (PTFE) in a discharge to yield a working fluid, APPT's have the added benefit of inert propellant storage with no pressure vessel requirements. PPT's typically fulfill secondary propulsion needs on spacecraft such as station-keeping and attitude control, but have recently garnered more attention as main propulsion for small spacecraft [11, 12]. Broadly, APPT's may be classified as either rectangular or coaxial geometry [10]. Coaxial geometry APPTs, like that of the PPT-4 [13], electrothermal PPTs [14-18], or ablative z-pinch PPTs [19], begin with a central and a downstream electrode and may have a conical-shaped dielectric between the electrodes. The central or upstream electrode is typically cylindrical and positively charged (anode) while the downstream electrode is ring-shaped. Solid propellant fills the space between electrodes and may be fed from the side through the conical dielectric. Most commonly this propellant is the inert polymer, PTFE, which is the state-of-the-art propellant for APPTs. A capacitor or bank of capacitors is charged to a few kilovolts, with that voltage applied across the electrodes.

The main arc discharge is initiated by an igniter, which is always located in or near the cathode in a PPT. The igniter generates a surface flashover discharge to create a seed plasma, initiating the main arc discharge. Radiation from this high temperature arc discharge heats the surface of the solid propellant, yielding gaseous propellant through ablation, which further fuels the arc. The coaxial PPT is a device dominated by electrothermal acceleration mechanisms, with the energy of the arc heating the gas to yield high exit velocities through gas-dynamic acceleration. Ablation processes are at the core of APPT operation, with many PTFE ablation studies in the literature [20-25].

The aforementioned dual mode device combining a solid chemical rocket motor mode with an electric coaxial APPT mode remains conceptual. Research in the use of HIPEP and other ESPs for gas-generation and chemical mode applications with long (>1 ms) timescales is ongoing and separate from the present work. Current efforts by the authors are focused on understanding the behavior of the HIPEP material in the proposed APPT pulsed electric mode. Our recent work has compared ablation of HIPEP with traditional PTFE in ablation-fed arc discharge devices [26-28]. At high temperatures and over long (~ms) time-scales, it is known that HIPEP undergoes a thermal decomposition process, while PTFE evaporates after depolymerization. However, ablation-controlled arc discharges occur on much shorter timescales, as the discharge current has a period of less than 10 μs. The specific ablation (μg/J) of HIPEP was measured to be roughly twice that of PTFE, and this difference was attributed to differences in the material thermal and chemical properties [26]. Plume measurements of HIPEP-fueled pulsed microthrusters [27] indicate electron temperatures (1-2 eV) and densities (10^{11}-10^{14} cm^{-3}) of the weakly ionized plasma comparable to that of PTFE fueled APPTs. Exhaust velocity measurements indicate similar performance of HIPEP relative to PTFE in the microthrusters. Further, it has been shown that the fraction of late-time ablation mass is similar for both propellants. Estimates from high-speed imagery of a pulsed HIPEP microthruster suggest that up to 50% of the ablated mass may be attributed to low-speed macroparticles ejected after the main current pulse [28].

To date, HIPEP has not been used in a traditional APPT configuration, where propellant material is ablated during a high current, short duration (~10 μs) arc discharge. Another ESP, the ammonium nitrate-based ABIP, was previously tested in Aerojet's modular test unit (MTU) and reported impulse bits were roughly 50-80% of the polytetrafluoroethylene (PTFE) solid propellant typically used in this unit [1]. No performance (impulse/thrust, specific impulse) metrics are yet published for a PPT using HIPEP as propellant. The objective of this work is to investigate the performance of the HAN-based HIPEP material relative to that of PTFE in an electrothermal APPT. The device is a coaxial geometry electrothermal APPT and a modified version of it was used previously to quantify the propellant specific ablation [26]. Both PTFE and HIPEP are used as propellants in this work and the impulse bit and specific impulse are measured using an inverted pendulum thrust stand. For each propellant, the device was operated for 100 or more pulses in vacuum, with the impulse bit measured throughout the test and the average propellant mass loss per pulse found by massing the propellant before and after a test. These measurements are the first reported one-to-one performance comparisons between the HIPEP and PTFE materials in an ablative pulsed plasma device. Results from these experiments, when combined with previous observations on the ablation of the

HIPEP material, can now be correlated to draw conclusions about the propulsive performance.

2. EXPERIMENTAL METHODS AND APPARATUS

We begin with a discussion of the methods and equipment used in the test trials in this work. First, details on the chemical composition and behavior of the HIPEP material are discussed. Next, we describe the geometry and basic operation of the electrothermal APPT device. Finally, a description of the thrust stand and associated calibration and data collection methods are reviewed.

2.1. HIGH PERFORMANCE ELECTRIC PROPELLANT

HIPEP is a HAN-based solution solid manufactured by Digital Solid State Propulsion (DSSP) using “green” ingredients and processes free of harmful fumes. HIPEP has a chemical composition of 75% HAN oxidizer (an inorganic ionic liquid), 20% polyvinyl alcohol (PVA) fuel binder, and 5% ammonium nitrate. It is mixed in standard chemical glassware, with only gloves and safety glasses needed for protection, and cured at 35°C/95°F. It is initially a liquid and poured into a mold, curing to form a rubbery solid with density ~1.8 g/cm^3 and the appearance and texture of a soft pencil eraser. In a typical PPT, the PTFE is an electrical insulator between the electrodes. The conductivity of HIPEP (1-2 S/m) is comparable to highly conductive ionic liquids. However, our previous work has shown that the conductivity of the HIPEP has a negligible effect on the measured current in the arc discharge. Further, it has been observed that the HIPEP material ablates more readily than PTFE in an ablation-fed arc, which may be attributed to thermodynamic properties of the solid propellant. It is currently unclear how the additional ablation mass contributes to the thrust produced by the material in an ablation-fed thruster.

The solid HIPEP material is hygroscopic and gradually absorbs moisture from a typical laboratory atmosphere (~50% rel. hum.), eventually causing the propellant to become completely liquid. To mitigate absorption of moisture in this work, HIPEP samples are handled and measured only in a dry-air glovebox kept at 5% relative humidity. Further, these samples undergo a vacuum drying process wherein samples were kept at $<5\times10^{-2}$ torr for at least 24 h. After this time, samples have reached steady state and the measured mass is within 0.26% of the dry mass [26].

2.2. ELECTRIC PROPELLANT THRUSTER EXPERIMENT

The electric propellant thruster experiment (EPTX) has geometry similar to that of a coaxial electrothermal APPT. Figure 2 details the geometry of the device. It should be noted that this device was originally used primarily to study the mass ablation of the propellants and not as a thruster [26]. The device was designed to facilitate removal and replacement of small propellant tube samples and is not optimized for performance. A circular stainless steel rod serves as the anode (positive) and a stainless steel ring with a 15° conical nozzle bore serves as the cathode (ground). The assembly is housed in a nonconductive PEEK body. The propellant tube sample has length 12 mm and inner diameter 6.35 mm. Because HIPEP is conductive, the propellant is isolated electrically from the two electrodes by thin PTFE washers with inner diameter ~7 mm which are not shown in Figure 2. These washers have an approximate thickness of <0.5 mm which is sufficient to hold off the maximum voltage (2.23 kV) used in the present work. The washers remain during PTFE testing to keep electrode spacing consistent between propellant samples. The test article and the capacitor bank are co-located inside the vacuum test facility. It is intended that the arc discharge occurs in the cylindrical cavity (6.35 mm dia.) formed by the inner propellant tube wall and the anode end. Because the test article is at vacuum, the capacitor can be charged to a high voltage (1-5 kV) across the anode/cathode-gap without initiating a Paschen breakdown. Breakdown of the gas is initiated by a surface discharge igniter constructed of two tungsten wires cemented in a two-bore alumina tube with ~2 mm exposed tip lengths. The wire tips are embedded in the nozzle of the cathode as shown in Figure 2. A capacitor discharge ignition (CDI) circuit creates a low energy surface discharge between the tungsten wire tips. Electrons from this discharge are accelerated to the positively charged anode and sputter particles from it and the nearby propellant, triggering the main arc discharge.

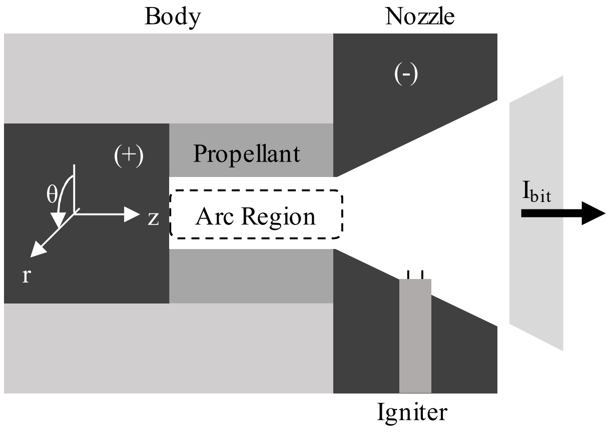

Figure 1: Diagram of the electric propellant thruster experiment.

During the main arc discharge current flows in the z-direction through the arc region from the anode and attaches at the cathode/nozzle electrode. This current oscillates between high positive and negative currents over a few microseconds. Because the magnetic field induced by this rapidly changing current is in the θ-direction and follows the sign of the current, the Lorentz force is always directed in the negative radial direction (pinching toward the *z*-axis) in the arc region labeled in Figure 2. Thus, the current sheet does not propagate along the *z*-axis in the cavity. In the conical nozzle region there is a radial component of current that may give rise to a small electromagnetic thrust component. The high current flowing through the resistance of the arc discharge in the cavity dissipates the energy that was initially stored on the capacitors. This energy transiently heats the walls of the propellant cavity to well above the vaporization temperature and causes ablation of propellant mass of ~30-300 μg/pulse. The gas generated by ablation is then further heated by the arc discharge to high temperatures on the order of a few eV. This mass of high temperature charged particles and neutrals are accelerated gas-dynamically via the nozzle and impart an impulse per pulse or impulse bit (I_{bit}). The capacitor bank must be recharged after each discharge and is triggered again at a repetition rate of once per ~20 seconds in this work. This low repetition rate means the propellant cools to room temperature after each discharge. Further details on operation, propellant sample preparation, and the ablation mass of PTFE and HIPEP in the precursor to this device may be found in our previous publication [26]. The only change in the device between that work and the present work is the change to a conical nozzle shape cathode.

2.3. COMPACT THRUST STAND

This work was conducted in Electric Propulsion Facility 1 at the University of Illinois Electric Propulsion Lab. This vacuum facility is approximately 1000 L in volume and achieves a nominal base pressure of ~2×10^{-5} torr. Housed in this facility is the UIUC Compact Thrust Stand designed for accurate measurement of thrust and impulse bit in the micro- and milli-Newton range [29]. This stand is of an inverted-pendulum design as shown in Figure 2 with a footprint of only 20x39 cm and 50 kg thruster mass capacity. Two modes of stand operation allow for constant thrust force measurement in the range of 1-10 mN and impulse bit measurement in the range of 0.1-3 mN-s. In this work, the stand is operated in impulsive measurement mode to determine the impulse bit of the electrothermal APPT device. In Figure 2, the thruster and hardware are mounted on top of the long stand platform which is mounted to the fixed frame by stainless steel arms with torsional flexures. These flexures allow the stand to stabilize at a neutral position with completely vertical arms which would otherwise be an unstable position. Further, any motion of the stand platform in the x-direction causes deflection of the stand arms and is opposed by the spring force of the torsional flexures. This assembly allows for oscillatory motion of the stand platform in the x-direction about the neutral position. Thrust stand calibration is performed using a method similar to the one described in Polk, *et al*. [30] for impulsive measurement using an inverted-pendulum thrust stand. A small impact hammer constructed of aluminum body and soft plastic head is mounted to a hinge and actuated by a solenoid. The solenoid is triggered remotely with a circuit that includes a potentiometer allowing for adjustment of plunger speed. When triggered, the head of the hammer strikes the center of a piezoelectric force transducer at the impact location shown in Figure 2. This strike delivers an impulsive force to the stand platform and generates motion in the x-direction. The output signal from the transducer is delivered to an oscilloscope providing a measurement of the force imparted over time. The impulse delivered to the stand may be calculated by integration of the transducer signal. In this work, the hammer delivers a calibration impulse bit in the range of roughly 100-1400 μN-s, with adjustment in this range facilitated by remote adjustment of the potentiometer.

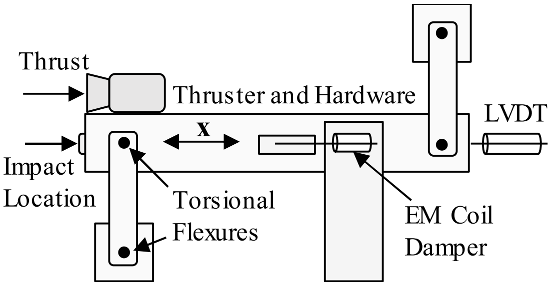

Figure 2: Diagram of the inverted-pendulum design UIUC Compact Thrust Stand.

For each strike of the hammer, the voltage waveform output by the force transducer is saved via the oscilloscope and later converted to force and integrated numerically. The measurement error for each hammer strike is ±6 μN-s due to bit noise and trapezoidal integration error. The motion of the thrust stand is monitored over time by a linear variable differential transformer (LVDT) affixed to the rear of the stand platform. This device outputs an analog voltage signal indicating the linear position of the stand platform that is digitized and monitored by a lab computer. Typical noise levels for this analog signal are on the order of 10^{-4} V, peak-to-peak. The output of the LVDT is used in two important ways during thrust stand operation. First, the digitized output is differentiated and fed through an amplifier to the electro-magnetic coil damper affixed between the stand platform and the fixed frame. This circuit uses magnetic eddy currents which increase in strength with voltage and interact with a metal shaft to retard movement of the stand platform towards zero velocity. Second, the output is logged to a file every 125 ms and later processed numerically to determine the response of the stand to an applied impulse bit. Specifically, the differential between successive position measurements (i.e., the velocity of the stand platform) is examined. For each strike of the impact hammer during calibration, a distinct peak in the differential voltage waveform is detected. The value of this peak in Volts is known as the response of the stand to the applied impulse bit.

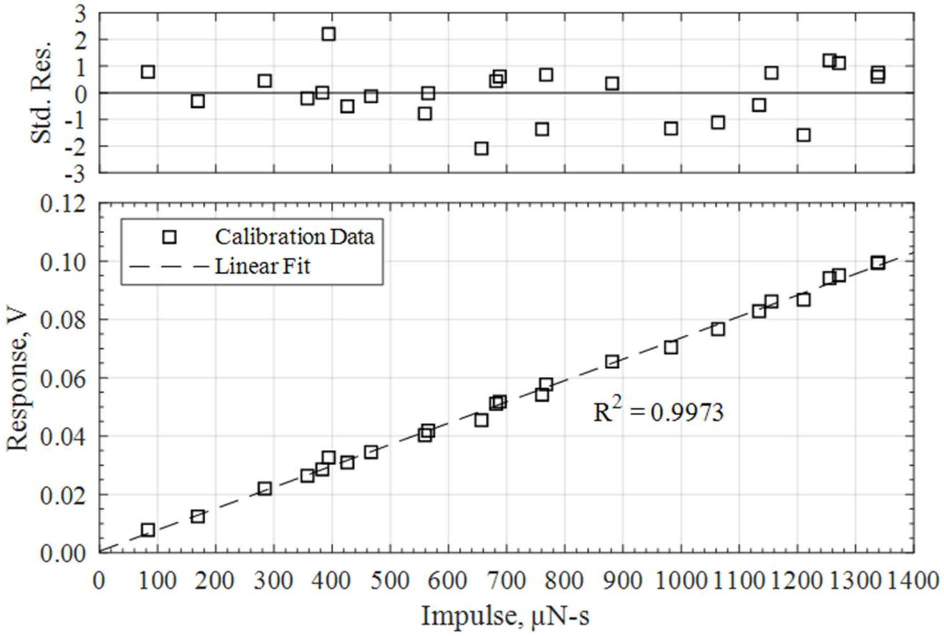

Figure 3: Typical pre-test thrust stand response calibration data as a function of applied impulse bit (bottom) and corresponding standardized residuals for the response data (top).

In this work, calibration was performed immediately prior to and following each testing session. Typically, 20-25 impulsive pulses are delivered to the stand and both transducer and LVDT output signals stored to memory for each. The response of the stand is plotted on the *y*-axis, the applied calibration impulse bits are plotted on the *x*-axis, and a linear fit to the data is established as the calibration curve. Figure 3 presents such a calibration curve for a typical pre-test calibration in the range of ~100-1400 μN-s. A standard least-squares regression method as described in Polk, *et al.*, [30] is used to determine the best linear fit to the calibration data. Also shown in Figure 3 are the standard residuals shown relative to the average standard residual indicated by the solid black line. A standard residual is the difference between the y-value predicted by the linear fit and the value measured in calibration (the residual) normalized by the standard deviation of the residuals. Standard residuals falling uniformly between -2 and +2 and randomly distributed around zero are indicative of a correctly assumed form of fit for the calibration curve. In Figure 3, the mean standard residual is $<10^{-12}$, which is typical in this work, and indicated by the solid black line. The value of the square of the correlation coefficient, or R^2, indicates the percentage of variation captured by the fit, and typical values for this work are 0.95 or greater, as indicated in Figure 3. After each calibration, a testing session was conducted wherein the EPTX device was pulsed once every ~20 seconds, imparting an impulse on the stand. For each pulse of the device, the thrust stand response was obtained from the LVDT measurement. The calibration curve in Figure 3 was then used to determine the impulse bit of each pulse based upon the measured thrust stand response. In the present work, the impulse bits measured are in the range of roughly 100-800 μN-s, which is fully contained in the linear region of the established calibration curve. A typical standard deviation of residuals in calibration is 1.5 mV. Using the linear fit in Figure 3, this suggests the error in a single impulse bit measurement is ±20 μN-s, equivalent to one standard deviation of response residual in either direction.

3. RESULTS

The EPTX was operated in the facility described and tested using PTFE and HIPEP as propellants for comparative purposes. Using the compact thrust stand, the impulse bit of each propellant was recorded for four nominal stored energy values of 5, 10, 15, and 20 J. Two test durations were conducted in this work: a short-duration test consisting of 100 pulses and a long-duration test to end-of-life. In this section, we present the results of these tests. First, short-duration test results are presented for each propellant operating at a single initial energy value, and then the average impulse bit over the short-duration tests at each energy level for both propellants are presented. Finally, the trend of impulse bit over the long-duration tests and the average impulse bit-per-joule of initial stored energy over the test duration is presented.

3.1. SHORT-DURATION TESTS

In our previous work, PTFE and HIPEP were tested in a similar device specifically designed to quantify the ablated mass per pulse [26]. The nominal test duration for that work was 100 pulses, which was initially selected as the test length for the short-duration test in this work. Each test begins with a ~20 point calibration at the nominal base pressure of 2×10^{-5} torr. The high voltage power supply is then set to the voltage corresponding to the desired energy level and impulse testing begins. Each pulse is triggered remotely via a surface discharge igniter and imparts an impulse to the thrust stand which is recorded and post processed to yield the impulse bit by the method described in Section 2.3. Figure 4 presents results from short-duration tests subdivided for each energy level. Six separate 100 pulse test trials are shown at each energy level, three for PTFE and three for HIPEP.

The estimated error for a single impulse bit measurement (±20 μN-s) is shown by black error bars.

It is observed in the Figure 4b 10 J measurements that the impulse bit between pulses 10-100 varies in the range of 250-300 μN-s for both propellants. However, it is noted that the measured impulse bit for the first pulses of all six trials is >350 μN-s which is 30% greater than the average impulse bit. Subsequent pulses 2-10 decrease in all trials until a rough steady state is achieved in the 250-300 μN-s range. This phenomenon of initially high and then decreasing impulse bits as the propellant surface is conditioned over the first few pulses has previously been observed in the literature [16, 19]. The impulse bit then varies about the mean and remains roughly constant, within the error bars, through pulse 100. The average impulse bit for all 3 tests (300 total pulses) shown for PTFE at the 10 J energy level is 278 μN-s, and for HIPEP is 271 μN-s. The standard deviation for all measurements in Figure 4b is ~22 μN-s. This is largely attributed to the measurement error resulting from the variation of stand response around the linear calibration curve. For each other energy level (5, 15, 20 J), three separate test trials were performed for each propellant and are shown in Figure 4a c, and d, respectively. This yields 24 one-hundred pulses trials, 12 trials for each propellant. All of these trials yielded impulse bit measurement results of the same form as Figure 4b, except one, Figure 4d, HIPEP-20-2. That is, all 23 of 24 trials show a first impulse bit measurement >30% above the average, decreasing between pulses 2-10, and variation around the mean with a constant trend for pulses 10-100. Further, all six trials at each energy level show similar mean values. The only major difference in results for other energy levels are the magnitude of the impulse bit measurements, which are shifted proportionally and discretely with energy level. HIPEP-20-2 shown in Figure

4d exhibited differing and unique behavior. In this trial, the impulse bit for pulses 1-10 were near the mean value of 608 μN-s, rather than 30% greater. An increasing trend over pulses 10-40 is observed, peaking at a value of ~700 μN-s, before decreasing again to end near the mean of the other trials. While this trial deviated significantly from the typical trend observed in the other subfigures of Figure 4, the mean impulse bit of this trial is still similar to the other five trials at 20 J.

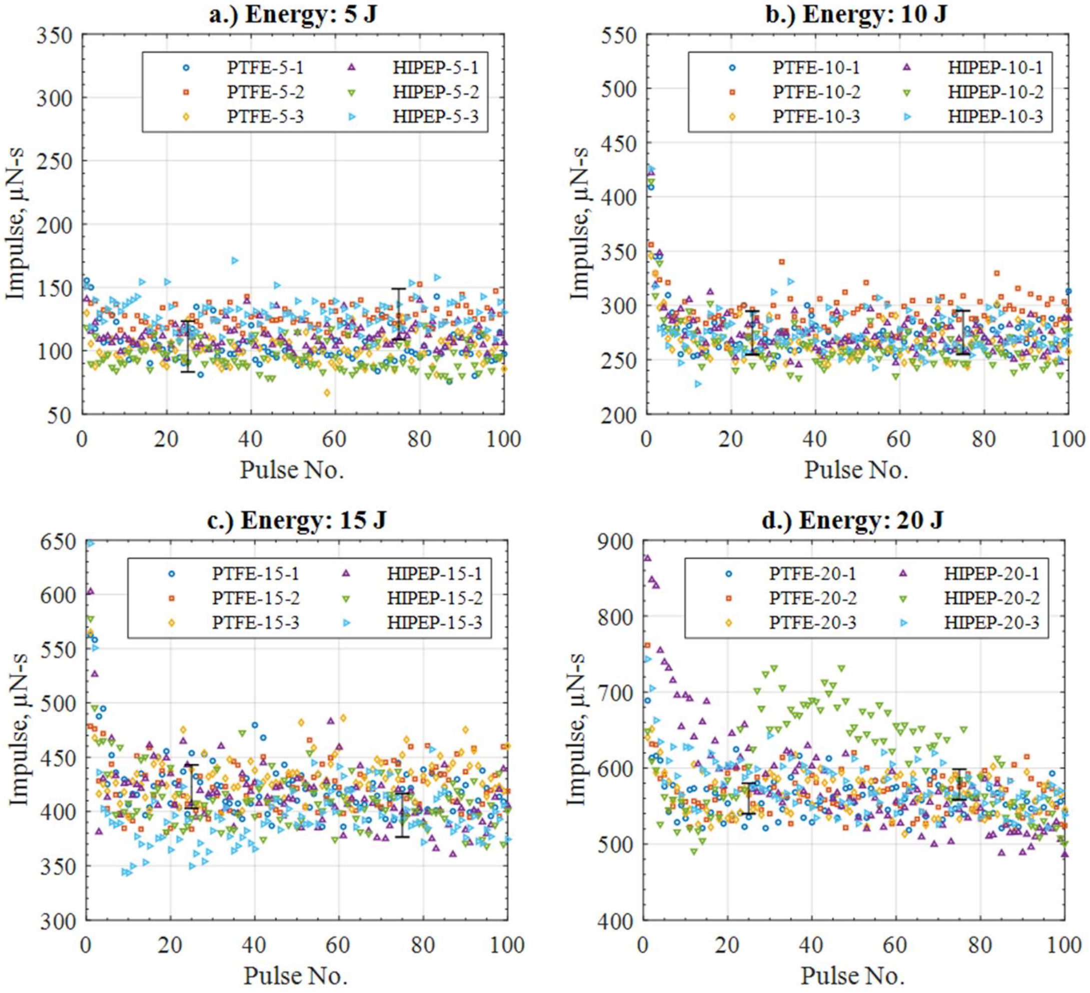

Figure 4: Impulse bit measurements for short-duration tests with both propellants and for a.) 5 J, b.) 10 J, c.) 15 J, and d.) 20 J nominal initial energy. Note the *y*-axis scales are adjusted for each plot.

Figure 5 presents the impulse bits averaged over 300 pulses (3 propellant samples at 100 pulses each) at each energy level for each propellant, with error bars indicating two standard deviations above and below the average. Also shown in Figure 5 is a linear fit and coefficients to the results for both propellants. From the average impulse bit results in Figure 5, it is observed that impulse bit increases linearly with initially stored energy with a slope of ~30 μN-s/J for both propellants. Impulse bit values at each energy level are nearly identical between propellants. At the 20 J energy level, HIPEP exhibits an average impulse bit of 590 μN-s compared to 565 μN-s for PTFE, a difference of 25 μN-s, or about 5%. This is the largest discrepancy between propellants at any energy, and 20 J is the only energy level where a larger impulse bit is measured for HIPEP. Standard deviation in impulse bit also increases with energy level for both propellants, but not at the same rate. The standard deviation for PTFE has a value of 16 μN-s at 5 J and 29 μN-s at 20 J, with a roughly linear slope between the two. At 5 J, HIPEP impulse bit standard deviation is 17 μN-s, similar to PTFE, but increases to 62 μN-s at the 20 J level.

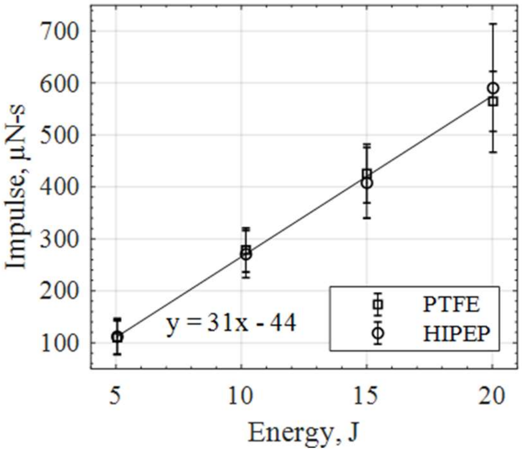

Figure 5: Average impulse bit over all short-duration tests at each initial energy for each propellant (error bars are a 2-σ standard deviation).

The standard deviation for HIPEP at 20 J was largely affected by the one anomalous short-duration trial previously discussed (see Figure 4d HIPEP-20-2). As a result of this trial's unique trend, the standard deviation for HIPEP measurements at 20 J is significantly increased compared to other energy levels and PTFE. Otherwise, the mean impulse bit at a given energy for HIPEP is typically ~95% of the mean impulse bit for PTFE, with increased variation (~10% larger standard deviation) about the mean.

3.2. LONG-DURATION TESTS

Also of interest in the present work is the trend of impulse bit over the entire lifetime of a propellant sample. Long-duration test trials were conducted using the same EPTX device and both HIPEP and PTFE propellant samples. In these trials, the device is pulsed at the same repetition rate, and impulse bit measured using the compact thrust stand as in the short-duration trials, but over a greater time period (>24 h). Automated pulsing of the EPTX device is achieved by use of a battery-powered timer circuit which remotely triggers the surface discharge igniter once every 22 seconds. At beginning of life, the inner diameter of a propellant sample is at the nominal dimension (6.35 mm) and the main arc discharge is easily triggered by the igniter. Each discharge ablates propellant material from the inner wall of the sample and gradually increases the diameter of the cavity in which the arc forms. As this diameter increases, ignition of the arc discharge becomes more difficult, and the time between successive pulses increases to two or more multiples of 22 s. That is, the first trigger event may not initiate arc formation, and a second or third trigger event is required. End-of-test in this work is defined as the pulse number where the time between pulses is in excess of 1 h, which means 160 trigger events do not initiate arc formation.

The long-duration test trials begin with fresh samples of nominal inner diameter and end at the sample end-of-life as just previously defined. Figure 6 presents the measurements of impulse bit over these long duration tests for the four nominal energy levels and for each propellant. Error bars here show the estimated measurement error for a single impulse bit measurement (±20 µN-s).

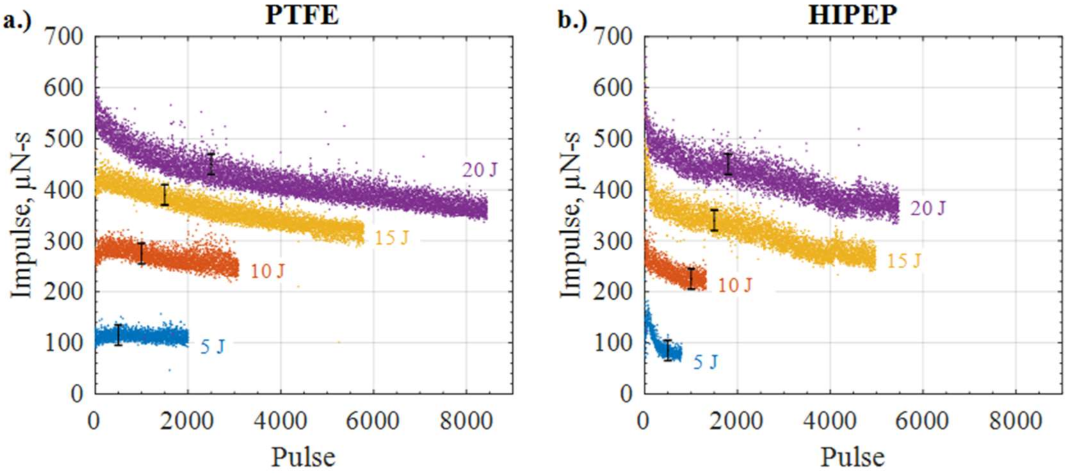

Figure 6: Impulse measurements for long-duration tests with a.) PTFE and b.) HIPEP propellant.

In Figure 6, it should first be noted that for each long-duration trial, comparison of pulses 1-100 shows close agreement with the trends observed in short-duration testing (Figure 4). For example, pulse 1 at 5 J using PTFE was measured to produce 130 µN-s and the impulse bit decreased to a mean value of about 115 µN-s over the first 100 pulses. Beyond pulse 100, PTFE impulse bit measurements at 5 J in Figure 6a are largely constant, and the mean over the full lifetime is 114 µN-s. At increased discharge energy, over the duration of the test a decreasing trend in impulse bit is observed. At 10 J, PTFE impulse bit measurements average ~274 µN-s through 100 pulses, but ~268 µN-s at end-of-life (3,083 pulses). A rough linear fit indicates the impulse bit decreases by about 1.1 µN-s per 100 pulses for PTFE at 10 J. At 15 J, this decrease is slightly greater in magnitude (1.8 µN-s per 100 pulses) but still nearly linear, and the average over the 5,783 pulses is 361 µN-s. At 20 J, the average over the full 8,445 pulses is 418 µN-s and a decreasing trend is still observed, but the profile deviates from a linear shape. Further, it is noted in Figure 6a that the lifetime of the test trial increases with energy level. Lifetime for PTFE is 8,445 pulses at 20 J compared to 2,000 pulses at 5 J. In Figure 6b for HIPEP testing, a similar trend of increasing lifetime with discharge energy is observed for HIPEP. This increase is most apparent between the 10 and 15 J energy levels, where pulse lifetime increases from 1,323 to 4,974 pulses. From beginning to end-of-life, however, slightly different trends are observed for HIPEP compared to PTFE. At 5 J, the decrease in impulse bit for HIPEP is much greater than for PTFE, decreasing by 19 µN-s per 100 pulses.

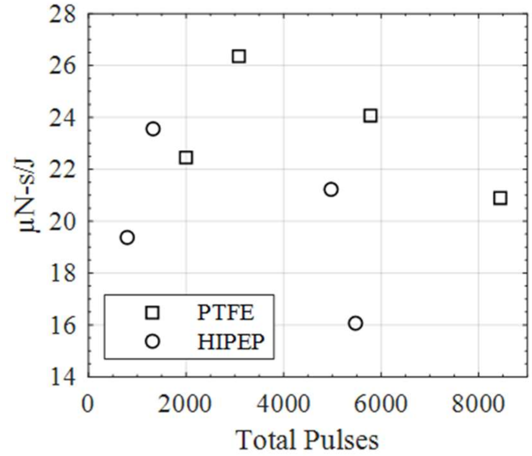

Figure 7: Average impulse bit per joule from the long-duration testing plotted as a function of total pulses.

Average impulse bit through pulse 100 is 120 μN-s but a decreasing trend is observed through the final pulse, and the lifetime is much shorter than 5 J for PTFE (793 vs. 2,000 pulses). These comparison trends continue at the higher energy levels, with HIPEP impulse bit typically decreasing more than PTFE over a shorter lifetime at a given energy. More discussion on the comparison of PTFE and HIPEP sample lifetimes may be found in Section 4.2.

Figure 7 presents the average impulse bit-per-Joule at end-of-life as a function of total pulses. Each point corresponds to the mean values for each test trial shown in Figure 6 over the full length of each test individually. For both propellants, the leftmost point (shortest lifetime) corresponds to the 5 J energy level trial, and the longest lifetime is for the 20 J energy level, as noted in Figure 6. Apart from the shortest lifetime points, both propellants generally exhibit a decrease in average impulse bit-per-Joule with lifetime. The short lifetime (low energy) point is noticeably decreased compared to the subsequent trend of the other points. This observation is combined with another to indicate a unique mode of operation for the low energy level in Section 4.1. Excluding the first data points in each series of Fig. 7, PTFE exhibits an approximately linear decrease in impulse bit per Joule of ~1 μN-s/J per 1000 pulses. Due to the limited test duration for HIPEP at 20 J compared to PTFE at similar energy, the corresponding points for HIPEP do not appear to follow the same linear trend as PTFE. Figure 7 highlights the previous observations on impulse bit and lifetime of HIPEP compared to PTFE. HIPEP impulse bits are typically about 90-99% of the value measured for PTFE for a given initial energy, resulting in a 10% reduction in the HIPEP data. Also, at each discharge energy the lifetime for the HIPEP samples is up to 60% less than PTFE.

4. ANALYSIS AND DISCUSSION

Further details and discussion concerning the results presented in the previous section are provided here. We begin with a brief discussion of the mass loss during testing and the resulting specific impulse for each propellant. Discussion of the observed difference in lifetime of the two propellants in the EPTX device configuration follow. Comparison of these key metrics between the two propellants are a focus in this section.

4.1. SPECIFIC IMPULSE

One of the most commonly reported performance metrics for in-space propulsion devices is the specific impulse, or I_{sp}. This quantity is expressed in seconds and describes the efficiency at which the device can generate thrust per unit mass of propellant. In this work, I_{sp} is obtained by

$$I_{sp} = \frac{I_{total}}{mg} \tag{1}$$

where I_{total} is the sum of all impulse bit measurements for a given trial and g is the acceleration due to gravity. In a previous work, the ablation mass m was investigated in a similar device [26]. The same propellant sample preparation procedures were followed in this work, and similar mass losses were measured during short duration tests. In general, ablation mass increases in a linear fashion as a function of discharge energy. For PTFE, the ablation mass at 5 J is 35.3 µg/pulse which yields a specific ablation of ~7 µg/J. For the other, higher energy levels, the specific ablation is on average a constant ~6.3 µg/J. HIPEP ablation exhibits similar scaling, but at a specific ablation rate that is much greater than PTFE. At 5 J, the ablation mass of HIPEP is on average 106.8 µg/pulse or ~21 µg/J, which is about three times that of PTFE. The specific ablation of HIPEP decreases to about 12.5 μg/J at the higher discharge energy levels tested. This is roughly twice that of PTFE. Because the measured impulse bits at all energy levels are nearly identical between the two propellants, the higher mass ablated per pulse results in a specific impulse for HIPEP that is significantly lower than for PTFE. The I_{sp} of both propellants were calculated using Eq. (1) for the short-duration (100 pulse) test trials and the results are presented in Figure 8. The measurement error for HIPEP (ϵ_H) specific impulse is ±50 s based on mass loss measurement error of ±35 μg/pulse [26] and impulse measurement error of ±20 μN-s. For PTFE, the measurement error (ϵ_P) is ±30 s. These errors are shown as representative error bars in Figure 8.

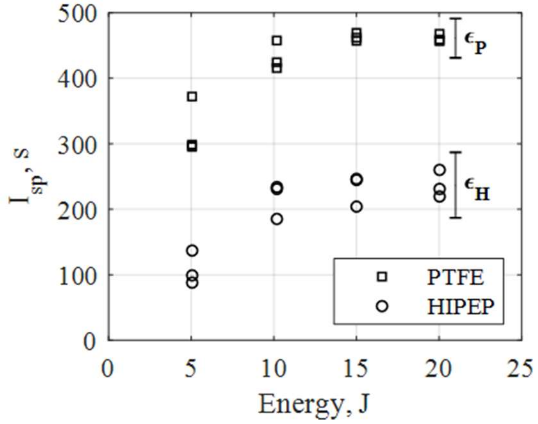

Figure 8: Specific impulse as a function of energy for each short-duration test for each propellant. Representative error bars are shown for HIPEP ($\boldsymbol{\epsilon_H}$) and PTFE ($\boldsymbol{\epsilon_P}$).

Because of the increased ablation mass relative to stored energy, the specific impulse at 5 J is reduced for both propellants. For PTFE, the average I_{sp} at 5 J is ~320 s compared to >400 s at the higher energy levels. HIPEP specific impulse at 5 J is on average

~100 s, but is typically above 200 s at 10, 15, and 20 J. The reduced specific impulse at 5 J relative to a mostly constant value for other energies indicates this device may be operating in a different mode at low energy. One option is that a charring phenomenon observed in APPTs using PTFE as propellant at low energy is reducing the specific impulse. In the case of current density over the propellant surface below some threshold, excessive carbonization (i.e. charring) of the PTFE occurs and leads to non-uniform ablation [31, 32]. It is possible that this non-uniformity may translate to non-uniform heating of the ablated material and thus a lower average exhaust velocity and specific impulse. Alternatively, at the low energy level, the energy available for the arc discharge may be too low to sustain a breakdown across the entire gap, yielding an incomplete current channel that can not dissipate the electrical energy efficiently. Though the EPTX device is not optimized as a thruster, its performance is near to that of other similar devices. The measured I_{sp} for PTFE at 10 J or above in this work is comparable to other coaxial geometry APPTs using PTFE as propellant. For example, the IL (University of Illinois) coaxial PPT was measured to have specific impulse of 500-600 s operating with a stored energy of 7.5 J/pulse [10, 29]. Various configurations of the ablative Z-pinch PPT, which possesses a geometry similar to the EPTX, exhibited specific impulse in the range of ~300-600 s [19]. On average, over the three higher energy levels, the specific impulse for PTFE is calculated to be ~450 s, compared to ~225 s for HIPEP. The measured impulse bits between propellants was virtually identical but the ablation mass for HIPEP was significantly greater. This leads to the conclusion that much of the additional mass ablated when operating on HIPEP did not appreciably contribute to increasing the impulse bit, but rather that it was expelled at a low average velocity. This may be due to one or both of the following phenomena. Additional mass ablated while operating on HIPEP could require significantly more energy to heat to a temperature required to achieve an exhaust velocity similar to PTFE. Or a large portion of the additional mass ablated could be liberated after the discharge is complete (late time ablation), ejected in the form of low speed vapor and macroparticles that generate little to no additional contribution to the impulse bit. Evidence of late time ablation for HIPEP has been confirmed but not thoroughly quantified in a previous work [28, 33].

4.2. PROPELLANT SAMPLE LIFETIME

The main driving factor in end-of-life for this device configuration is the ratio of stored electrical energy to exposed propellant surface area, or the energy density (J/mm^2). At beginning-of-life, the propellant sample inner diameter is the nominal 6.35 mm and energy density is at a maximum. Each pulse of the device ablates a portion of the inner wall of the propellant cavity, increasing the inner diameter and exposed propellant surface area. Assuming that this ablation occurs uniformly along the azimuthal and axial directions, the final diameter, d_2 may be determined by

$$d_2 = \sqrt{d_1^2 + \frac{4m}{\pi \rho l}} \tag{2}$$

where d_1 is the initial inner diameter of the propellant sample, l is the sample length, ρ is the density of the propellant, and m is the total mass loss over the course of the test trial. Comparison of d_2 calculated by Eq. (2) with measured inner diameter showed excellent agreement to within 0.2 mm for PTFE. Measurements for inner diameter of HIPEP samples were complicated by the flexibility of the material, but predictions for d_2 are typically 1-10% greater than for PTFE due to the increased HIPEP mass loss, m, and lower HIPEP density, ρ. The ratio of stored energy to propellant surface area reaches a minimum threshold at end-of-life, making the ignition of a discharge difficult or impossible. Based on calculations and measurements of PTFE sample inner diameters, the threshold for this behavior is 20-60 mJ/mm^2. The threshold for HIPEP is similar. Based on the predicted value of d_2 the threshold is 20-50 mJ/mm^2. The specific value of the energy density threshold described here is likely dependent on the energy of the igniter used to trigger the arc discharge and the overall geometry of the setup. In the present work, the igniter has a stored energy of ~40 mJ and is not adjustable. Future designs utilizing HIPEP as propellant in an APPT are likely to use a similar method and must be designed to expend all propellant before reaching the threshold for igniting a discharge.

In Figure 6, a clear distinction in test duration is observed between propellants. Long-duration tests with PTFE at each energy level yielded more total pulses than for each test with HIPEP. For instance, at 5 J, the end-of-life for a HIPEP sample occurred after 793 pulses, only 39% of the 2,000 pulses for a sample of PTFE. While this is the largest difference in the testing performed, the HIPEP lifetime at 10 and 15 J is only 43% and 86% of PTFE, respectively. The difference in lifetime is caused by two major differences in the propellant materials. First, the density of HIPEP is only 1.8 g/cm^3 compared to 2.2 g/cm^3 for PTFE. Thus, even for constant propellant consumption rate (i.e., equal μg/pulse) between propellants, the change in inner diameter would still be greater for HIPEP. Second, as discussed in Section 4.1, at a given energy the ablation rate for HIPEP is typically twice that of PTFE. Together, the higher ablation rate and lower propellant density of HIPEP serve to significantly reduce that propellant's overall lifetime relative to PTFE.

4.3. THRUST MODE

The impulse bit of a coaxial geometry APPT is typically dominated by electrothermal acceleration of the working fluid, as opposed to electromagnetic. Computation of the electromagnetic contribution to impulse (I_{EM}) is entirely dependent on the inductance gradient per unit length, L', of the discharge channel. The electromagnetic contribution may be calculated as [10]

$$I_{EM} = \frac{1}{2} L' \int I^2 \, dt \tag{3}$$

where I is the current flowing through the thruster-capacitor circuit. In a previous work [26], we measured I in a device of similar geometry and identical electrical circuit for each of the energy levels presented in this work. In the present work, the measured current at each energy is within a few percent of the waveforms presented in the previous work. By numerical integration of those waveforms at each energy level, we obtain a minimum value of 14 A-s/J at 5 J increasing to 20 A-s/J at 20 J. This value is almost purely dependent on energy, as variation between the PTFE and HIPEP propellants at each energy level is at most 1 A-s/J. Typically for coaxial PPTs, the inductance gradient term in Eq. (3) is calculated using the result obtained for the magnetoplasmadynamic (MPD) thruster [10]

$$L' = \frac{\mu_0}{2\pi} \left[\ln\left(\frac{r_a}{r_c}\right) + \frac{3}{4} \right] \tag{4}$$

In Eq. (4) r_a is the inner radius of the annular electrode (here, the nozzle/cathode) and r_c is the outer radius of the central rod electrode. Derivation of Eq. (4) considers both pumping (radial) and blowing (axial) components of the Lorentz force, which are present in MPD thrusters and coaxial PPTs [34]. In the propellant cavity of the EPTX device, the force is entirely directed in the radial direction and thus has no axial or blowing component. For this case, the axial inductance gradient is simplified to

$$L' = \frac{\mu_0}{4\pi} \tag{5}$$

which has a constant value of 0.1 μH/m. Note that the result in Eq. (5) is obtained by assuming that the axial pumping force is balanced by the gradient of gas pressure in the arc region. In the EPTX device the z-pinch force creates a high pressure region at the core of the arc region and a low pressure region at the propellant wall. Thus, the pressure gradient is directed toward the core of the arc and is able to balance the pumping component of Lorentz force. Substituting values for inductance gradient and current integral values into Eq. (3) we calculate that the electromagnetic contribution to the impulse bit is in the range of 0.7-1.0 μN-s/J, or about 3-5% of the total impulse measured in this work. This very low fraction confirms the assumption that the EPTX device is dominated by the electrothermal contribution to measured impulse. Because the thrust mode of the device is electrothermal, the specific impulse depends strongly on the ablation mass of the propellant, and very weakly on electric circuit parameters. HIPEP ablates more readily than PTFE, but impulse does not increase, yielding reduced specific impulse despite similar parameters calculated for the arc discharge circuit [26].

5. CONCLUSIONS

A compact thrust stand of inverted pendulum design was used to measure the impulse of an electrothermal APPT. This device was operated using both PTFE and an electric solid propellant, HIPEP, as propellant. The impulse bit for PTFE was around 100 μN-s for 5 J of initial stored energy and it increased by ~30 μN-s per Joule of additional stored energy. The impulse bit for HIPEP was typically 95-99% of PTFE, exhibiting similar trends at each of the four energy levels tested (5, 10, 15, and 20 J). The device used in this work was not designed as an optimized APPT, so the specific impulse for PTFE is roughly 450 s. This is just at the bottom of the range of other coaxial APPTs tested using PTFE. The ablated mass of HIPEP for a given discharge energy is typically double that of PTFE and, as a result, the calculated specific impulse is approximately half that of the thruster operating on PTFE. In the present work, we have found that the additional ablated mass does not increase the measured impulse when compared with the thruster operating on PTFE under identical testing conditions. These new insights and combined understanding of the propellant ablation, thermochemistry, and propulsion performance can help guide future design of pulsed electric devices using this propellant. In the early pulses of a test (< 10 pulses), impulse measurements are typically up to 30% greater than the mean impulse. Though the additional total impulse imparted during this region of test is not significant, it is unclear how much propellant mass is expelled during these early pulses. For the hygroscopic HIPEP material, it could be an amount of absorbed moisture is evaporated during these pulses due to high transient heating. This evaporation could skew mass loss measurements, and potentially bias calculated specific impulse.

ACKNOWLEDGMENTS

M.S. Glascock would like to graciously thank the NASA Space Technology Research Fellowship program for funding his graduate research via grant NNX15AP31H. This work is a large part of that research and would not be possible without the support from this program. Additionally, the authors wish to thank DSSP for providing the HIPEP material in custom-made form for our research, as well as numerous discussions on the nuances of HIPEP operation and handling.

REFERENCES

[1] Sawka, W. N., and McPherson, M., "Electrical Solid Propellants: A Safe, Micro to Macro Propulsion Technology," *49th Joint Propulsion Conference*, AIAA Paper 2013-4168, San Jose, CA, 2013.

[2] Sawka, W. N., U.S. Patent for a "Controllable Digital Solid State Cluster Thrusters for Rocket Propulsion and Gas Generation," No. 7958823 B2 and 8464640; June 14, 2011 and June 18, 2013.

[3] Dulligan, M., U.S. Patent for a "Electrically Controlled Extinguishable Solid Propellant Motors," No. 7788900B2; September 7, 2010.

[4] Chung, K., Rozumov, E., Kaminsky, D., Buescher, T., Manship, T., Valdivia, A., Cook, P., and Anderson, P., "Development of Electrically Controlled Energetic Materials," *ECS Transactions,* Vol. 50, No. 40, 2013, pp. 59-66.

[5] Grix, C., and Sawka, W. N., U.S. Patent for a "Family of Modifiable High Performance Electrically Controlled Propellants and Explosives," No. 8888935B2; November 18, 2011.

[6] Sawka, W. N., and Grix, C., U.S. Patent for a "Family of Metastable Intermolecular Composites Utilizing Energetic Liquid Oxidizers with Nanoparticle Fuels in Sol-Gel Polymer Network," No. 8317953B2; November 27.

[7] Baird, J. K., Lang, J. R., Hiatt, A. T., and Frederick, R. A., "Electrolytic Combustion in the Polyvinyl Alcohol Plus Hydroxylammonium Nitrate Solid Propellant," *Journal of Propulsion and Power,* Vol. 33, No. 6, 2017, pp. 1589-1590.

[8] Hiatt, A. T., and Frederick, R. A., "Laboratory Experimentation and Basic Research Investigation Electric Solid Propellant Electrolytic Characteristics," *52nd AIAA/SAE/ASEE Joint Propulsion Conference*, AIAA Paper 2016-4935, Salt Lake City, UT, 2016.

[9] Sawka, W. N., and Grix, C., U.S. Patent for a "Electrode Ignition and Control of Electrically Ignitable Materials," No. 8857338B2; October 14.

[10] Burton, R. L., and Turchi, P. J., "Pulsed Plasma Thruster," *Journal of Propulsion and Power,* Vol. 14, No. 5, 1998, pp. 716-735.

[11] Gatsonis, N. A., Lu, Y., Blandino, J., Demetriou, M. A., and Paschalidis, N., "Micropulsed Plasma Thrusters for Attitude Control of a Low-Earth-Orbiting CubeSat," *Journal of Spacecraft and Rockets,* Vol. 53, No. 1, 2016, pp. 57-73.

[12] Keidar, M., Zhuang, T., Shashurin, A., Teel, G., Chiu, D., Lukas, J., Haque, S., and Brieda, L., "Electric Propulsion for Small Satellites," *Plasma Physics and Controlled Fusion,* Vol. 57, No. 1, 2015, pp. 1-10.

[13] Bushman, S., and Burton, R. L., "Heating and Plasma Properties in a Coaxial Gasdynamic Pulsed Plasma Thruster," *Journal of Propulsion and Power,* Vol. 17, No. 5, 2001, pp. 959-966.

[14] Cheng, L., Wang, Y., Ding, W., Ge, C., Yan, J., Li, Y., Li, Z., and Sun, A., "Experimental Study on the Discharge Ignition in a Capillary Discharge Based Pulsed Plasma Thruster," *Physics of Plasma,* Vol. 25, No. 9, 2018.

[15] Wang, Y., Ding, W., Cheng, L., Yan, J., Li, Z., Wang, J., and Wang, Y., "An Investigation of Discharge Characteristics of an Electrothermal Pulsed Plasma Thruster," *IEEE Transactions on Plasma Science,* Vol. 45, No. 10, 2017, pp. 2715-2724.

[16] Aoyagi, *et al.*, "Total Impulse Improvement of Coaxial Pulsed Plasma Thruster for Small Satellite," *Vacuum,* Vol. 83, No. 1, 2008, pp. 72-76.

[17] Edamitsu, T., and Tahara, H., "Experimental and Numerical Study of an Electrothermal Pulsed Plasma Thruster for Small Satellites," *Vacuum,* Vol. 80, No. 11, 2006, pp. 1223-1228.

[18] Miyasaka, T., Asato, K., Sakaguchi, N., and Ito, K., "Optical Measurements of Unsteady Phenomena on Coaxial Pulsed Plasma Thrusters," *Vacuum,* Vol. 88, 2013, pp. 52-57.

[19] Markusic, T. E., Polzin, K. A., Choueiri, E. Y., Keidar, M., Boyd, I. D., and Lepsetz, N., "Ablative Z-Pinch Pulsed Plasma Thruster," *Journal of Propulsion and Power,* Vol. 21, No. 3, 2005, pp. 392-400.

[20] Keidar, M., Boyd, I. D., and Beilis, I. I., "Electrical Discharge in the Teflon Cavity of a Coaxial Pulsed Plasma Thruster," *IEEE Transactions on Plasma Science,* Vol. 28, No. 2, 2000, pp. 376-385.

[21] Keidar, M., Boyd, I. D., and Beilis, I. I., "Model of an Electrothermal Pulsed Plasma Thruster," *Journal of Propulsion and Power,* Vol. 19, No. 3, 2003, pp. 424-430.

[22] Ruchti, C. B., and Niemeyer, L., "Ablation Controlled Arcs," *IEEE Transactions on Plasma Science,* Vol. PS-14, No. 4, 1986, pp. 423-434.

[23] Schönherr, T., Komurasaki, K., and Herdrich, G., "Propellant Utilization Efficiency in a Pulsed Plasma Thruster," *Journal of Propulsion and Power,* Vol. 29, No. 6, 2013, pp. 1478-1487.

[24] Seeger, M., Tepper, J., Christen, T., and Abrahamson, J., "Experimental Study on PTFE Ablation in High Voltage Circuit-Breakers," *Journal of Physics D: Applied Physics,* Vol. 39, No. 23, 2006, pp. 5016-5024.

[25] Wang, W., Kong, L., Geng, J., Wei, F., and Xia, G., "Wall Ablation of Heated Compound-Materials into Non-Equilibrium Discharge Plasmas," *Journal of Physics D: Applied Physics,* Vol. 50, No. 7, 2017.

[26] Glascock, M. S., Rovey, J. L., and Polzin, K. A., "Electric Solid Propellant Ablation in an Arc Discharge," *Journal of Propulsion and Power*, 2019, pp. 1-10, Online July 2019.

[27] Glascock, M. S., Rovey, J. L., Williams, S., and Thrasher, J., "Plume Characterization of Electric Solid Propellant Pulsed Microthrusters," *Journal of Propulsion and Power,* Vol. 33, No. 4, 2017, pp. 870-880.

[28] Glascock, M. S., "Characterization of Electric Solid Propellant Pulsed Microthrusters," M.S. Thesis, Missouri University of Science and Technology, 2016.

[29] Wilson, M. J., Bushman, S., and Burton, R. L., "A Compact Thrust Stand for Pulsed Plasma Thrusters," *25th International Electric Propulsion Conference*, ERPS Paper IEPC-97-122, Cleveland, OH, 1997.

[30] Polk, J. E., Pancotti, A., Haag, T., King, S., Walker, M. L. R., Blakely, J., and Ziemer, J., "Recommended Practice for Thrust Measurement in Electric Propulsion Testing," *Journal of Propulsion and Power,* Vol. 33, No. 3, 2017, pp. 539-555.

[31] Keidar, M., Boyd, I. D., Antonsen, E. L., Burton, R. L., and Spanjers, G. G., "Optimization Issues for a Micropulsed Plasma Thruster," *Journal of Propulsion and Power,* Vol. 22, No. 1, 2006, pp. 48-55.

[32] Keidar, M., Boyd, I. D., Antonsen, E. L., Gulczinski III, F. S., and Spanjers, G. G., "Propellant Charring in Pulsed Plasma Thrusters," *Journal of Propulsion and Power,* Vol. 20, No. 6, 2004, pp. 978-984.

[33] Glascock, M. S., Rovey, J. L., Williams, S., and Thrasher, J., "Observation of Late-Time Ablation in Electric Solid Propellant Pulsed Microthrusters," *52nd AIAA/SAE/ASEE Joint Propulsion Conference*, AIAA Paper 2016-4845, Salt Lake City, UT, 2016.

[34] Jahn, R. G., *Physics of Electric Propulsion*, New York: McGraw-Hill, 1968.

IV. SPECIFIC IMPULSE OF ELECTRIC SOLID PROPELLANT IN AN ELECTROTHERMAL ABLATION-FED PULSED PLASMA THRUSTER

Matthew S. Glascock,

Missouri University of Science and Technology, Rolla, MO 65409

Joshua L. Rovey,

University of Illinois at Urbana-Champaign, Urbana IL 61801

and

Kurt A. Polzin

NASA Marshall Space Flight Center, Huntsville, AL

ABSTRACT

Electric solid propellants are advanced solid chemical rocket propellants that can be controlled (ignited, throttled, and extinguished) through the application and removal of an electric current. Recent work has focused on application of this propellant in an electrothermal ablation-fed pulsed plasma thruster. In this paper, impulse bit measurements in such devices fed by either the electric solid propellant or a traditional state-of-the-art propellant, polytetrafluoroethylene, are expanded upon. It is demonstrated that a surface layer in the hygroscopic electric solid propellant is rapidly ablated over the first few discharges of the device, which correspondingly decreases specific impulse relative to the traditional polytetrafluoroethylene propellant. Correcting these data by subtracting the early discharge ablation mass loss measurements yields a corrected electric solid propellant specific impulse of approximately 300 s. As the test duration increases to a large number of discharges, and the initial mass loss is a reduced fraction of the total, the

effect of absorbed water in the propellant is decreased and the specific impulse without any corrections approaches the corrected 300 s value.

1. INTRODUCTION

This decomposition is a highly exothermic process that generates hot gas at a burn rate that can be throttled by varying the applied current. Removal of the voltage and current extinguishes the reaction, which may be restarted by reapplication of electric power [2]. Because this reaction is only induced by electric current, ESPs are not susceptible to accidental ignition by spark, impact, or open flame. These characteristics are extremely beneficial compared to traditional solid rocket propellants, which are not throttleable, toggleable, or insensitive to external ignition. The advent of ESPs expands the potential applications for solid propellants that were previously infeasible.

Development of ESPs began in the 1990’s with the design of an automobile air bag inflator propellant (ABIP) using materials safe for unprotected human contact (i.e., “green” materials). This ABIP was ammonium nitrate-based and was later repurposed for use in other areas, including rocket propulsion. Shortly thereafter, “ASPEN,” the first digitally controlled extinguishable solid propellant, was developed[3]. This propellant featured additives with the ammonium nitrate base to lower melting point and increase electrical conductivity[2]. The material exhibited performance metrics comparable to that of previous solid rocket propellants, but major problems existed with the repeatability of ignition. Further development for gas-generation applications led to a special family of electrically controlled energetic materials which may be mixed to yield solid, liquid, or gel form propellants, all of which are electrically ignitable[4, 5]. Some mixtures are flame-sensitive and explosive, some insensitive to flame and sustainable, and some are insensitive and extinguishable like the ESPs. One particular formula with high specific impulse and electrical conductivity is known as the high performance electric propellant, or HIPEP[1, 6], which is not sensitive to open flame, spark, or impact, and is extinguishable. In this solid energetic material, the ionic liquid oxidizer hydroxyl-ammonium nitrate (HAN) is dissolved and cross-linked in polyvinyl alcohol (PVA), forming a gel that is hardened by baking. The resulting rubbery solid HIPEP exhibits a pyroelectric behavior unique to energetics. When direct current electric power is applied, a proton transfer reaction between hydroxyl-ammonium and nitrate is promoted, and the level of nitric acid rapidly rises in the material eventually triggering ignition of the propellant. This exothermic, gas-generating reaction may be harnessed in a solid rocket motor to generate on demand thrust using electric power.

HIPEP's pyroelectric behavior may facilitate a dual mode propulsion system using the solid propellant. The first mode is a high thrust chemical mode where direct current electric power is applied to incite pyroelectric gas generation. This gas is expanded through a nozzle to generate thrust like any typical solid rocket motor. The duration of each chemical mode activation is determined by the duration that electric power is supplied. The inventors of this propellant and collaborating groups have reported on this mode of operation[7-9]. Using a second circuit connected to the motor in parallel with the pyroelectric circuit, this solid rocket may also be operated in a high specific impulse (I_{sp}) electric mode. One promising electric mode circuit configuration is based upon a pulsed electric propulsion device known as the coaxial ablation-fed pulsed plasma thruster (APPT).

Pulsed plasma thrusters[10] (PPTs) have been in use since the first orbital flight of an electric propulsion device in 1964. PPTs offer repeatable impulse bits with higher exhaust velocities than can be achieved using chemical thrusters. Ablating polytetrafluoroethylene (PTFE) in the discharge to yield a working fluid, APPT's have the added benefit of inert propellant storage with no pressure vessel requirements. PPT's typically fulfill secondary propulsion needs such as station-keeping and attitude control on spacecraft, but have recently garnered more attention as a main propulsion for small spacecraft[11, 12]. Broadly, PPT's may be classified as either rectangular or coaxial geometry[10]. Coaxial geometry APPT's, like that of the PPT-4[13], electrothermal PPT[14-18], or ablative z-pinch PPT[19], begin with a central and a downstream electrode and may have a conical-shaped discharge channel between the electrodes. The central or upstream electrode is typically cylindrical and positively charged (anode) while the downstream electrode is ring-shaped. Solid propellant fills the space between electrodes and may be fed from the side through the conical dielectric comprising the walls of the discharge channel. Most commonly this solid propellant is the inert polymer PTFE, which is the state-of-the-art propellant for APPTs. A capacitor or bank of capacitors is charged to a few kilovolts, with that voltage applied across the electrodes. The main arc discharge is initiated by an igniter, which is always located in or near the cathode in a PPT. The igniter generates a surface flashover discharge to create a seed plasma, initiating the main arc discharge. Radiation from this high temperature arc discharge heats the surface of the solid propellant, causing ablation of gaseous propellant species, further fueling the arc. The coaxial PPT is a device dominated by electrothermal acceleration mechanisms, with the energy of the arc heating the gas to yield high exit velocities through gas-dynamic acceleration. Ablation processes are at the core of APPT operation, and thus many studies on the ablation of PTFE exist in literature[20-25].

The aforementioned dual mode device combining a solid chemical rocket motor mode with an electric coaxial APPT mode remains conceptual. Research on the use of HIPEP and other ESPs for gas-generation and chemical mode applications with long (>1 ms) timescales is ongoing and separate from the present work. Current efforts by the authors are focused on understanding the behavior of the HIPEP material in the proposed APPT electric mode. Our recent work has compared the ablation of HIPEP with that of traditional PTFE tested in ablation-fed arc discharge devices[26-28]. At high temperatures and over long (~ms) time-scales, it is known that HIPEP undergoes a thermal decomposition process, while PTFE evaporates after depolymerization. However, ablation-controlled arc discharges occur on much shorter timescales, as the discharge current has a period of less than 10 μs. The specific ablation (μg/J) of HIPEP was measured to be roughly twice that of PTFE, and this difference was attributed to differences in the thermal and chemical properties between the materials[26]. Plume measurements of HIPEP-fueled pulsed microthrusters[27] indicate electron temperatures (1-2 eV) and densities (10^{11}-10^{14} cm^{-3}) of the weakly ionized plasma that are comparable to PTFE-fueled APPTs. The measured exhaust velocities are comparable for microthrusters operating HIPEP or PTFE. Further, it has been shown that the fraction of late-time ablation mass is similar between propellants. Estimates from high-speed imagery of a pulsed HIPEP microthruster suggest that up to 50% of the mass ablated may be attributed to low-speed macroparticles ejected after the main current pulse[28].

Our most recent work investigated the performance of HIPEP in an electrothermal APPT device, where propellant material is ablated during a high current, short duration (~10 μs) arc discharge and accelerated by predominantly electrothermal mechanisms. The impulse bit (impulse-per-pulse) operating on PTFE and HIPEP was measured using an inverted pendulum thrust stand for both short and long-duration tests at stored energy levels ranging from 5-20 J. Results indicated that the impulse bit was nearly identical between propellants regardless of energy level, with HIPEP impulse bits typically 5% less than those for PTFE. Impulse bits at 5 J were ~100 μN-s and increased linearly by ~30 μN-s/J up to ~550 μN-s at 20 J. Measured mass loss for HIPEP was double that of PTFE, resulting in a calculated specific impulse of 225 s for HIPEP compared to 450 s for PTFE. However, it was postulated that because the first few pulses on HIPEP resulted in impulse bits that were typically 10-30% greater than the average over the first 100 pulses, that absorbed moisture or other surface impurities could be affecting mass loss (and thus specific impulse) measurements during those pulses. In the present work we investigate this behavior in greater detail. Very short duration tests are conducted to quantify the early-pulse mass loss, and the mass loss measurements in long-duration tests are closely examined for both PTFE and HIPEP propellant to identify long-term trends in the calculated specific impulse. We discuss the role of moisture absorbed by the hygroscopic HIPEP in mass loss measurements and specific impulse calculations, as well as its impact on future thruster designs.

2. EXPERIMENTAL APPARATUS

2.1. HIGH PERFORMANCE ELECTRIC PROPELLANT

HIPEP is a HAN-based solution solid manufactured by Digital Solid State Propulsion (DSSP) using “green” ingredients and processes free of harmful fumes. HIPEP has a chemical composition of 75% HAN oxidizer (an inorganic ionic liquid), 20% polyvinyl alcohol (PVA) fuel binder, and 5% ammonium nitrate. It is mixed in standard chemical glassware, with only gloves and safety glasses needed for protection, and cured at 35°C/95°F. It is initially a liquid and poured into a mold, curing to form a rubbery solid with density ~1.8 g/cm^3 and the appearance and texture of a soft pencil eraser. Our previous work has shown that HIPEP ablates more readily than PTFE in an ablation-fed arc, which we have shown that it is attributable to the differences in the thermodynamic properties of the solid propellant. Specifically, the decreased thermal degradation temperature and energy required to evolve propellant vapor lends to increased ablation of HIPEP relative to PTFE[26].

The solid HIPEP material is hygroscopic and gradually absorbs moisture from a typical laboratory atmosphere (~50% rel. hum.), eventually causing the propellant to become completely liquid. To mitigate absorption of moisture, HIPEP samples are handled and measured only in a dry-air glovebox kept at 5% relative humidity. The material is stored only in a vacuum or dry-air environment. Further, the test samples undergo a vacuum drying process wherein samples were kept at $<5\times10^{-2}$ torr for at least 24 h. After this time, samples have reached steady state and the measured mass is within 0.26% of the dry mass[26]. A Sartorius QUINTIX125D-1S dual range semi-micro balance was used to measure the mass of propellant samples before and after testing. In the selected range, this balance has a capacity of 60 g and can be read down to an increment of 0.01 mg. The factory reported repeatability of the balance is 0.02 mg. For measurements reported here the typical variation in measurement was ±0.03 mg.

2.2. COMPACT THRUST STAND

Testing was conducted in Electric Propulsion Facility 1 (affectionately named the "Burton chamber") at the University of Illinois Electric Propulsion Lab. This facility is approximately 1000 L in volume and achieves a base pressure of $\sim 2\times 10^{-5}$ torr. Housed in this facility is the UIUC compact thrust stand, which was designed for accurate measurement of thrust and impulse bit in the micro- and milli-Newton range[29]. The stand is of an inverted-pendulum design with a footprint of only 20x39 cm and 50 kg thruster mass capacity. Two modes of stand operation allow for constant thrust force measurement in the range of 1-10 mN and impulsive measurements in the range of 0.1-3.0 mN-s. In the present work the stand was operated in impulsive measurement mode to quantify the impulse-per-pulse, or impulse bit, of a pulsed plasma device. Thrust stand calibration is performed using a method similar to the one described in Polk, *et al.*,[30] for impulsive measurements using an inverted-pendulum thrust stand. A remotely actuated impact hammer delivers an impulse of typically 100-1400 μN-s to the stand. The hammer directly strikes a piezo-electric force transducer, which measures the force imparted as a function of time. Integration of this signal yields the impulse imparted to the stand. Each strike of the hammer generates oscillatory motion of the thrust stand, which is measured by a linear variable differential transformer (LVDT). The integrated force signals and associated stand response measurements are then combined to establish a calibration curve of stand response as a function of known impulse which may be used to determine a single impulse bit within ±20 μN-s. Further details and a sample calibration curve may be found in a recent previous publication[31].

2.3. ELECTRIC PROPELLANT THRUSTER EXPERIMENT

The electric propellant thruster experiment (EPTX) used in this work has geometry similar to that of a coaxial electrothermal APPT. Figure 2 details the geometry of the device. It should be noted that this device was originally used primarily to study the mass ablation of the propellants and not as a thruster[26]. The device was designed to facilitate removal and replacement of small propellant tube samples and is not optimized for performance. More recently, the device was modified with the addition 15° conical nozzle shape in the stainless steel cathode in an attempt to utilize thermal energy imparted to the plasma by the arc discharge. A circular stainless steel rod serves as the anode (positive) upstream and the assembly is housed in a nonconductive PEEK body. The propellant tube sample has length 12 mm and inner diameter 6.35 mm. During operation, up to ~2.3 kV is supplied between the anode and cathode, and breakdown is held off by vacuum. The device is triggered by a surface discharge igniter embedded in the nozzle of the cathode as shown in Figure 2. A capacitor discharge ignition (CDI) circuit creates a low energy surface discharge between the tungsten wire tips. Electrons from this discharge are accelerated to the positively charged anode and sputter particles from it and the nearby propellant, triggering the main arc discharge in the cavity formed by the propellant tube inner wall and the anode end.

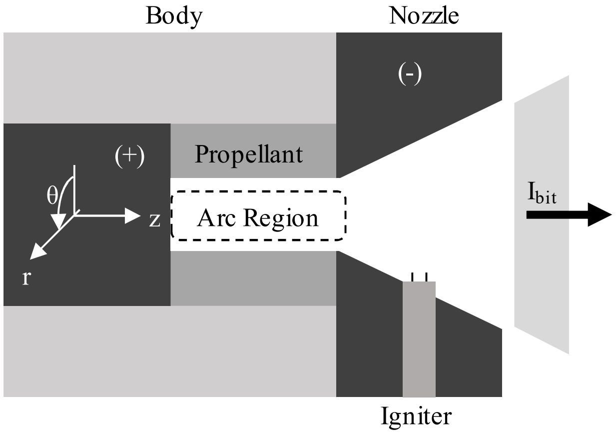

Figure 1: Diagram of the electric propellant thruster experiment.

During the main arc discharge high current flows between the anode and cathode, oscillating around zero with the same form of an underdamped inductance-capacitance-resistance series circuit possessing a period of a few microseconds. In this device, the Lorentz force is directed in the negative radial direction (pinching toward the *z*-axis) in the arc region. In the conical nozzle region, a radial component of current may give rise to a small electromagnetic thrust component, but the device is known to be primarily electrothermal. The energy that was initially stored in the capacitors is deposited in the plasma through resistive dissipation. This energy transiently heats the walls of the propellant cavity to well above the vaporization temperature and causes ablation of propellant at a rate of between ~30-300 μg/pulse, dependent upon the discharge energy. The gas generated by ablation is then further heated by the arc discharge to high temperatures on the order of a few eV. This mass of high temperature charged particles and neutrals is accelerated gas-dynamically via the nozzle to impart an impulse per pulse or impulse bit (I_{bit}). In the present work the device is triggered at a repetition rate of once per ~20 seconds. This low repetition rate means the propellant has time to cool before the next discharge is initiated.

3. EXPERIMENTAL APPROACH

We first summarize the significant findings from a previous experimental investigation to frame the approach used in the present work. In the previous work, short duration constant discharge energy test runs of 100 pulses were conducted in the EPTX device with both PTFE and HIPEP. The impulse bit was measured for testing at nominal discharge energy levels of 5, 10, 15 and 20 J. A representative impulse bit data set acquired during the course of one test on each propellant is shown in Figure 8a. These data have been normalized by the average impulse bit values for their respective 100 pulse sets.

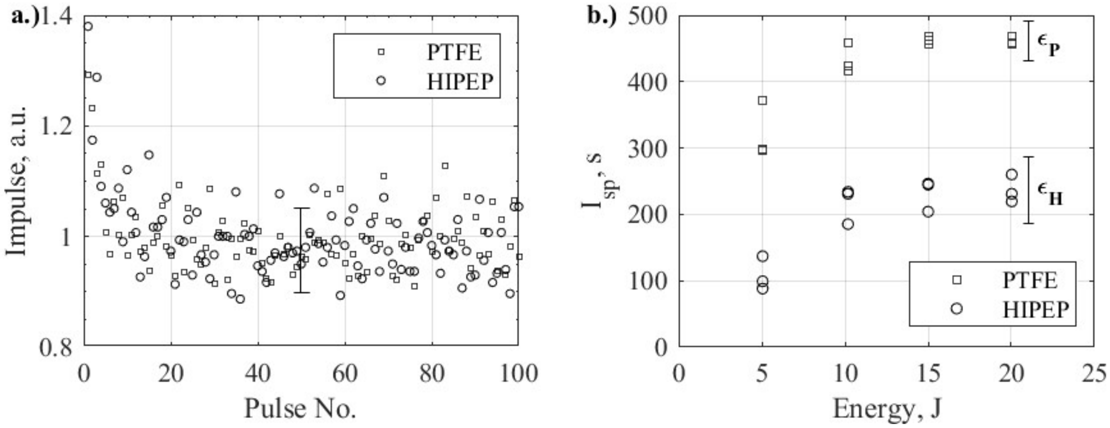

Figure 2: Summary of results from ref. [31]. a.) Impulse bit measurements over short duration tests representative of most trials and normalized by average impulse bit, and b.) Specific impulse as a function of energy over short-duration tests; representative error bars are shown for HIPEP ($\boldsymbol{\epsilon_H}$) and PTFE ($\boldsymbol{\epsilon_P}$).

We observe for both propellants that after a short initial transient the impulse bit stabilizes, varying about the mean and remaining roughly constant, within the error bars (±20 μN-s), for pulses 10-100. During the initial transient, the impulse bit for the first pulse of each test run is 30-40% greater than the average and decreases in each subsequent trial for pulses 2-10 until a rough steady state is achieved near the average value. This phenomenon of initially high and then decreasing impulse bits as the propellant surface is conditioned over the first few pulses has previously been observed in the literature for PTFE [16, 19].

The mass of each propellant sample was measured directly before and after a test run to determine the net ablation mass loss during each test. Special preparation procedures [26] were followed to evaporate absorbed moisture in the hygroscopic HIPEP material. In general, ablation mass increased in a linear fashion as a function of discharge energy. For PTFE, the ablation mass at 5 J was 35.3 μg/pulse which yielded a specific ablation of ~7 μg/J. For the other, higher energy levels, the specific ablation was on average a constant ~6.3 μg/J. HIPEP ablation exhibits similar scaling, but at a specific ablation rate that is much greater than PTFE. At 5 J, the ablation mass of HIPEP is on average 106.8 μg/pulse or ~21 μg/J, which is about three times that of PTFE. The specific ablation of HIPEP decreases to about 12.5 μg/J at the higher discharge energy levels tested. This is roughly twice that of PTFE. Also reported in the previous work was the average specific impulse, or I_{sp}. This quantity is expressed in seconds and is defined as the total impulse for a test run divided by the total weight of propellant expelled during the test. This is written as

$$I_{sp} = \frac{I_{total}}{mg} \tag{1}$$

where I_{total} is the sum of all impulse bit measurements for a given test run, m is the ablation mass loss during a given test run, and g_0 is the acceleration due to gravity. Since the measured impulse bits at all energy levels are nearly identical between the two propellants, the higher mass ablated per pulse results in a specific impulse for HIPEP that is significantly lower than for PTFE. Shown in Figure 8b are the average I_{sp} values calculated using Eq. (1) for both propellants over several short-duration (100 pulse) test trials. The measurement error for HIPEP (ϵ_H) specific impulse is ±50 s and for PTFE, the measurement error (ϵ_P) is ±30 s. These errors are shown as representative error bars in the figure. On average from 10-20 J, the specific impulse for PTFE is calculated to be ~450 s compared to ~225 s for HIPEP.

Two key observations in the above results influenced the present work. First, the increased impulse bit over pulses 1-10 indicated some form of propellant surface conditioning was occurring. Our initial hypothesis was that the ablation mass loss was also greater during these pulses, but we could not definitively test this hypothesis because only average mass loss data over the full 100 pulse duration of each test was available. Consequently, in the present work we performed very short duration tests of only 10 pulses to better quantify the early-pulse mass losses. The aim is to understand the mass loss during the early pulses for and gain further insight into the increased ablation of HIPEP relative to PTFE.

Finally, it was noted in our original tests that the 5 J energy level specific impulse values for both propellants are significantly decreased relative to the higher energy levels. While the exact cause of the reduction at the low energy is currently unknown, it is suspected that the stored energy is insufficient to sustain a uniform arc discharge in the given cavity geometry. As a result, the arc would be either incomplete or non-uniform, causing non-uniform wall ablation and heating of propellant in the cavity. Therefore, many of the observations in the present paper may only be valid for the 10-20 J energy range, and may not hold for lower energy discharges.

4. RESULTS

The EPTX was tested using PTFE and HIPEP as propellants. In addition to the short-duration tests consisting of 100 pulses each and long-duration tests to end-of-life, both of which were reported in Ref. [[31]], in the present work we conducted very-short-duration tests consisting of 10 pulses. In this section, we present the results of these very-short-duration tests and compare those results to the 100 pulse short duration test results. First, a typical short-duration test at a single initial energy value, and then the average impulse bit over the short-duration tests at each energy level for both propellants are presented. Finally, the trend of impulse bit over the long-duration tests and the average impulse bit-per-joule of initial stored energy over the test duration is presented.

Testing and sample preparation procedures for very-short-duration 10 pulse tests were identical to those of the short-duration (100-pulse) tests and earlier ablation mass tests[26]. Samples are stored in rough vacuum for 24 h directly prior to mass measurement allowing absorbed water to evaporate. The initial sample mass is measured directly after vacuum drying and before loading into the EPTX device. After testing and another 24 hours of post-test vacuum drying, the final mass is measured. The ablation mass loss for the trial is the difference between initial and final masses. Results for 10-pulse trials at each energy level are shown in Table 1 alongside the average mass loss measured for 100-

pulse trials. Also shown in the final column of Table 1 is the 10-pulse mass loss as a percent of the 100-pulse mass loss

Table 1: Ablation mass loss for short- and very-short-duration tests trials.

Propellant	Energy, J	10-pulse mass loss, mg	100-pulse mass loss, mg	10-pulse mass loss, %
PTFE	5.05	0.37	3.53	10.5%
	10.18	0.70	6.91	10.1%
	15.00	1.00	9.47	10.6%
	20.03	1.28	12.48	10.3%
HIPEP	5.05	5.82	10.68	50.7%
	10.18	6.42	13.33	48.2%
	15.00	6.02	18.43	32.7%
	20.03	6.14	26.06	23.6%

In Table 1 we observe at similar conditions that the mass loss for HIPEP is significantly greater than for PTFE. In 100-pulse tests, HIPEP mass loss is typically about twice that of PTFE. This is much greater in the 10-pulse tests, where the HIPEP mass loss is nearly six times that of PTFE. Second, while the mass loss of PTFE clearly increases with energy in 10-pulse trials, the same is not observed for HIPEP. Rather, the 10-pulse mass loss data for HIPEP appears to be independent of stored energy and is, on average, ~6 mg. Finally, we note that for all energy levels, the 10-pulse mass loss is 10-11% of the 100-pulse mass loss for PTFE. This result indicates that PTFE mass loss is roughly constant for both the 10-pulse and 100-pulse intervals. For HIPEP, the mass loss during 10-pulse tests is much greater than 10% in all cases, indicating that much of the mass lost during the 100-pulse tests was lost during the first 10 pulses.

5. ANALYSIS AND DISCUSSION

The phenomenon of initially high and then decreasing impulse bits over the first few pulses has previously been observed in the literature for PTFE fueled ablation-fed devices [16, 19]. The propellant surface is conditioned by the transient heating from the adjacent arc discharge resulting in the removal of impurities during those pulses. These impurities may be foreign particles on the surface acquired through handling or contact with a non-vacuum atmosphere. While PTFE is not porous or hygroscopic, it is expected that a small amount of moisture may reside on the surface as an impurity of the material before being subjected to the vacuum. These impurities add mass to the initial measurements, but evaporate or are expelled quickly during the first few pulses. In Table 1 we see that the first 10 pulses with PTFE exhibit a mass loss-per-pulse that is about 1% higher than the next 90 pulses. This indicates that the mass of impurities that are then expelled during propellant conditioning is quite small compared to the mass loss due to arc discharge ablation. Furthermore, a summation of the impulses in Figure 8a reveals that the sum total impulse for the first 10 pulses is about 10.8% of the sum total impulse for all 100 pulses. The additional mass (<1%) expelled due to surface impurities roughly translates to a relative increase of impulse (<1%) in the early pulses, indicating that on average the impurities are likely liberated by the arc discharge and accelerated to near the bulk plasma velocity.

As seen in Table 1 for HIPEP, the mass loss-per-pulse during pulses 1-10 is much greater than that of the 90 subsequent pulses. In the most extreme case, at 5 J, the mass lost in the first 10 pulses is more than 50% of the total mass loss over an entire 100 pulse test. However, using the data in Figure 8a, the sum total impulse for the first 10 pulses is only 10-11% of the sum total impulse from all 100 pulses. These combined observations indicate first that HIPEP not has more mass loss attributed to surface impurities (and thus more mass loss in earlier pulses) relative to PTFE. They also indicate that the average gas velocity of these first few pulses is significantly reduced because the impulse bit remains unchanged. Because HIPEP is extremely hygroscopic, we attribute this phenomenon to water absorbed into the propellant. The propellant preparation procedure appears to effectively remove a considerable amount of water (typically 5-6% propellant mass) by allowing it to slowly evaporate when exposed to vacuum conditions. It is possible that some water is able to absorb deeper into the fibers of the material, rather than just the surface. This deeply absorbed water would typically require a greater amount of time to evaporate in vacuum. The addition of thermal energy through arc discharge heating would greatly increases the evaporation rate and the commensurate mass loss rate. However, the fraction of early mass loss is significant and the vacuum drying process is sophisticated so we expect that a majority of the absorbed water is released during this preparation. Prior to drying, the absorbed water molecules may chemically react with the propellant resulting in a surface layer of unknown chemical composition and thickness. This layer of unknown chemical composition would not revert back to the original chemical composition of the propellant through a drying process. It is possible that this layer, which would be adjacent to the arc discharge for early pulses of a test, could ablate more readily than the standard propellant composition.

The mass loss measurement for HIPEP is skewed artificially high because of the very high mass loss rates in the early pulses. As a result, commensurate specific impulse calculations for the duration of the test are skewed lower. In the interest of reporting a specific impulse that is ideally achievable, we develop a simple method to correct the average mass lost data. Specifically, we subtract the mass loss and total impulse measured in first 10 pulses from results for 100-pulse mass loss and total impulse measurements, and then perform all the calculations to obtain the average mass loss-per-pulse and average corrected I_{sp} using those remaining 90 pulses from the 100-pulse test. The 100 pulse average I_{sp} values from Figure 8b and the and corrected values for HIPEP are shown in Figure 3.

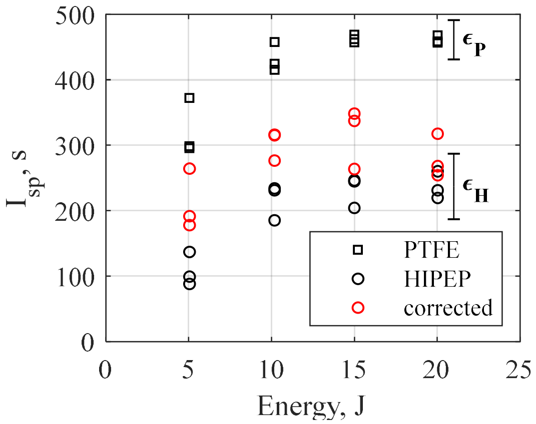

Figure 3: Specific impulse over short-duration trials, both raw and corrected for excess early mass loss.

In Figure 3 we observe that the corrected I_{sp} for HIPEP is greater than or equal to the previously measured values at each energy level. In fact, all but one corrected value at 20 J is greater than all of the previous results at that energy. This is the expected result, based upon the observation that a significant fraction sometimes constituting a majority of the mass is lost in early pulses. When we ignore this poor propellant utilization in early pulses, the overal specific impulse increases. At ≥10 J, the mean corrected I_{sp} is ~300 s, with the data scattered relatively uniformly about that value. As before, the mean corrected I_{sp} at the 5 J is reduced when compared to the higher energy data, with an average value of 211 s.

In the long-duration testing, the thruster was operated until the trigger pulse could no longer initiate a discharge[31]. As the number of discharges increase, the overall mass loss for an experimental data set will be larger and the initial mass loss for the first 10 pulses would become a decreasingly-small portion of the overall mass loss. Consequently, we expect that the average mass loss-per-pulse based on pre- and post-test mass measurements of the propellant will start to approach the corrected average mass loss-per-pulse obtained for pulses 11-100 of the 100-pulse tests. We can also use the same method (subtract from the data set the mass loss and total impulse measured in first 10 pulses) to correct the long-duration test data to quantify the effect of increased initial mass bits on calculated specific impulse.

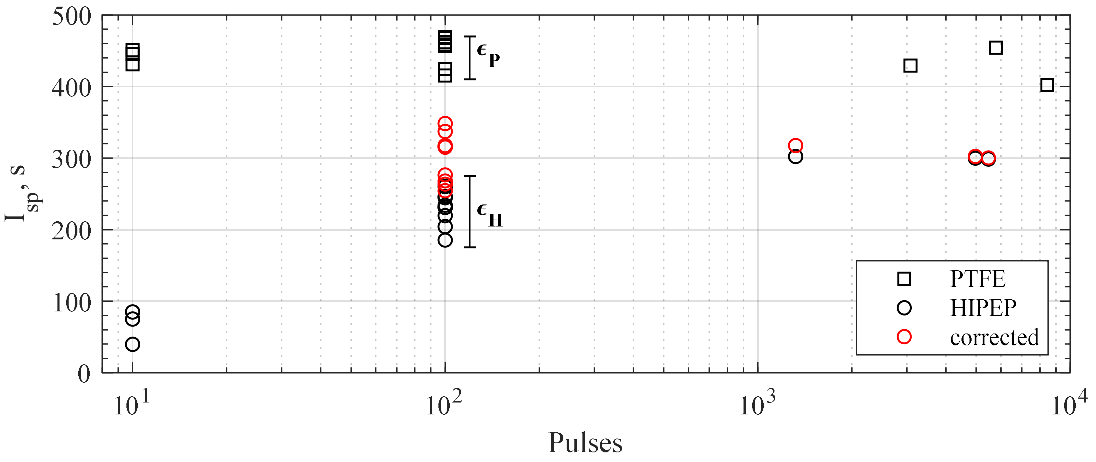

Figure 4: Specific impulse as a function of test duration, both raw values and corrected values.

In Figure 4 we present for both HIPEP and PTFE the raw average specific impulse values for the 10, 15, and 20 J pulse energies as a function of number of pulses in the test for the very-short (10 pulse), short (100 pulses), and long-duration (1000+ pulses) tests. Representative error bars for short-duration PTFE (ϵ_P) and HIPEP (ϵ_H) specific impulse calculations are shown. We also present in Figure 4 for HIPEP tests the corrected specific impulse for short- and long-duration tests.

We observe that the raw calculated specific impulse of HIPEP does indeed appear to asymptotically approach the corrected value as pulse number increases. In the long-duration tests (1,000+ pulses), we find that the corrected specific impulse for HIPEP is very similar to the raw calculated value. As an illustration of this, the longest duration test on HIPEP involved 5,474 pulses at 20 J. This resulted in an overall mass loss of 788 mg and the total impulse 2.31 N-s, which yeilds a raw average specific impulse of roughly 300 s. The typical mass loss for the very-short 10-pulse duration test conducted at 20 J was 6 mg and total impulse was approximately 5 mN-s. These values are both less than 1% of the long-duration test totals, limiting their overall influence on the average specific impulse calculated using the long-duration test data. As a check, applying the correction by removing contribution of the first 10 pulses to the overall mass loss and total impulse has minimal effect, with the corrected specific impulse remaining roughly 300 s.

6. CONCLUSION

We have presented impulse and total mass loss measurements for an electric solid propellant known as HIPEP tested for different numbers of pulses and compared this testing with data obtained under similar conditions for operation on PTFE. The average specific impulse for PTFE was calculated from the total mass loss and impulse measurements, and it was found to be relatively constant for a given discharge and not dependent on total pulses. This implied relatively constant surface conditions for PTFE. The HIPEP propellant is significantly different in that it is a hygroscopic material and absorbed water greatly affects the experimental results. Drying the material by exposure to vacuum allows much of the absorbed water to evaporate over about 24 h. However, there are residual effects from the water that was absorbed by the propellant. In a coaxial ablation-fed PPT, the result is vastly increased ablation mass loss in the first several arc discharges near the surface. The mass loss in these early pulses is up to 50% higher than later in the device lifetime, but the total impulse during these pulses is only 10% increased. These observations are attributed either to the evaporation of deeply absorbed water remaining in the propellant or a reaction of the propellant surface with absorbed water to form a surface layer that decomposes and ablates in the presence of a high-current discharge more readily than the HIPEP material exposed after the surface layer is removed. As a result, the average specific impulse for 100-pulses tests on HIPEP was only 225 s. Correcting these data by removing the contributions of the first ten pulses from the data set yielded an average specific impulse of 300 s. Increasing the test duration to thousands of pulses significantly diminished the effect early, high-mass-loss pulses had on the average specific impulse. In the long-term tests the average specific impulse is roughly the same as the value obtained from the 100-pulse tests when those data are corrected for the contributions of the first 10 pulses.

ACKNOWLEDGMENTS

M.S. Glascock would like to graciously thank the NASA Space Technology Research Fellowship program for funding his graduate research via grant NNX15AP31H. This work is a large part of that research and would not be possible without the support from this program. Additionally, the authors wish to thank DSSP for providing the HIPEP material in custom-made form for our research, as well as numerous discussions on the nuances of HIPEP operation and handling.

REFERENCES

[1] Sawka, W. N., and McPherson, M., "Electrical Solid Propellants: A Safe, Micro to Macro Propulsion Technology," *49th Joint Propulsion Conference*, AIAA Paper 2013-4168, San Jose, CA, 2013.

[2] Sawka, W. N., U.S. Patent for a "Controllable Digital Solid State Cluster Thrusters for Rocket Propulsion and Gas Generation," No. 7958823 B2 and 8464640; June 14, 2011 and June 18, 2013.

[3] Dulligan, M., U.S. Patent for a "Electrically Controlled Extinguishable Solid Propellant Motors," No. 7788900B2; September 7, 2010.

[4] Chung, K., Rozumov, E., Kaminsky, D., Buescher, T., Manship, T., Valdivia, A., Cook, P., and Anderson, P., "Development of Electrically Controlled Energetic Materials," *ECS Transactions,* Vol. 50, No. 40, 2013, pp. 59-66.

[5] Grix, C., and Sawka, W. N., U.S. Patent for a "Family of Modifiable High Performance Electrically Controlled Propellants and Explosives," No. 8888935B2; November 18, 2011.

[6] Sawka, W. N., and Grix, C., U.S. Patent for a "Family of Metastable Intermolecular Composites Utilizing Energetic Liquid Oxidizers with Nanoparticle Fuels in Sol-Gel Polymer Network," No. 8317953B2; November 27.

[7] Baird, J. K., Lang, J. R., Hiatt, A. T., and Frederick, R. A., "Electrolytic Combustion in the Polyvinyl Alcohol Plus Hydroxylammonium Nitrate Solid Propellant," *Journal of Propulsion and Power,* Vol. 33, No. 6, 2017, pp. 1589-1590.

[8] Hiatt, A. T., and Frederick, R. A., "Laboratory Experimentation and Basic Research Investigation Electric Solid Propellant Electrolytic Characteristics," *52nd AIAA/SAE/ASEE Joint Propulsion Conference*, AIAA Paper 2016-4935, Salt Lake City, UT, 2016.

[9] Sawka, W. N., and Grix, C., U.S. Patent for a "Electrode Ignition and Control of Electrically Ignitable Materials," No. 8857338B2; October 14.

[10] Burton, R. L., and Turchi, P. J., "Pulsed Plasma Thruster," *Journal of Propulsion and Power,* Vol. 14, No. 5, 1998, pp. 716-735.

[11] Gatsonis, N. A., Lu, Y., Blandino, J., Demetriou, M. A., and Paschalidis, N., "Micropulsed Plasma Thrusters for Attitude Control of a Low-Earth-Orbiting CubeSat," *Journal of Spacecraft and Rockets,* Vol. 53, No. 1, 2016, pp. 57-73.

[12] Keidar, M., Zhuang, T., Shashurin, A., Teel, G., Chiu, D., Lukas, J., Haque, S., and Brieda, L., "Electric Propulsion for Small Satellites," *Plasma Physics and Controlled Fusion,* Vol. 57, No. 1, 2015, pp. 1-10.

[13] Bushman, S., and Burton, R. L., "Heating and Plasma Properties in a Coaxial Gasdynamic Pulsed Plasma Thruster," *Journal of Propulsion and Power,* Vol. 17, No. 5, 2001, pp. 959-966.

[14] Cheng, L., Wang, Y., Ding, W., Ge, C., Yan, J., Li, Y., Li, Z., and Sun, A., "Experimental Study on the Discharge Ignition in a Capillary Discharge Based Pulsed Plasma Thruster," *Physics of Plasma,* Vol. 25, No. 9, 2018.

[15] Wang, Y., Ding, W., Cheng, L., Yan, J., Li, Z., Wang, J., and Wang, Y., "An Investigation of Discharge Characteristics of an Electrothermal Pulsed Plasma Thruster," *IEEE Transactions on Plasma Science,* Vol. 45, No. 10, 2017, pp. 2715-2724.

[16] Aoyagi, *et al.*, "Total Impulse Improvement of Coaxial Pulsed Plasma Thruster for Small Satellite," *Vacuum,* Vol. 83, No. 1, 2008, pp. 72-76.

[17] Edamitsu, T., and Tahara, H., "Experimental and Numerical Study of an Electrothermal Pulsed Plasma Thruster for Small Satellites," *Vacuum,* Vol. 80, No. 11, 2006, pp. 1223-1228.

[18] Miyasaka, T., Asato, K., Sakaguchi, N., and Ito, K., "Optical Measurements of Unsteady Phenomena on Coaxial Pulsed Plasma Thrusters," *Vacuum,* Vol. 88, 2013, pp. 52-57.

[19] Markusic, T. E., Polzin, K. A., Choueiri, E. Y., Keidar, M., Boyd, I. D., and Lepsetz, N., "Ablative Z-Pinch Pulsed Plasma Thruster," *Journal of Propulsion and Power,* Vol. 21, No. 3, 2005, pp. 392-400.

[20] Keidar, M., Boyd, I. D., and Beilis, I. I., "Electrical Discharge in the Teflon Cavity of a Coaxial Pulsed Plasma Thruster," *IEEE Transactions on Plasma Science,* Vol. 28, No. 2, 2000, pp. 376-385.

[21] Keidar, M., Boyd, I. D., and Beilis, I. I., "Model of an Electrothermal Pulsed Plasma Thruster," *Journal of Propulsion and Power,* Vol. 19, No. 3, 2003, pp. 424-430.

[22] Ruchti, C. B., and Niemeyer, L., "Ablation Controlled Arcs," *IEEE Transactions on Plasma Science,* Vol. PS-14, No. 4, 1986, pp. 423-434.

[23] Schönherr, T., Komurasaki, K., and Herdrich, G., "Propellant Utilization Efficiency in a Pulsed Plasma Thruster," *Journal of Propulsion and Power,* Vol. 29, No. 6, 2013, pp. 1478-1487.

[24] Seeger, M., Tepper, J., Christen, T., and Abrahamson, J., "Experimental Study on PTFE Ablation in High Voltage Circuit-Breakers," *Journal of Physics D: Applied Physics,* Vol. 39, No. 23, 2006, pp. 5016-5024.

[25] Wang, W., Kong, L., Geng, J., Wei, F., and Xia, G., "Wall Ablation of Heated Compound-Materials into Non-Equilibrium Discharge Plasmas," *Journal of Physics D: Applied Physics,* Vol. 50, No. 7, 2017.

[26] Glascock, M. S., Rovey, J. L., and Polzin, K. A., "Electric Solid Propellant Ablation in an Arc Discharge," *Journal of Propulsion and Power*, 2019, pp. 1-10, Online July 2019.

[27] Glascock, M. S., Rovey, J. L., Williams, S., and Thrasher, J., "Plume Characterization of Electric Solid Propellant Pulsed Microthrusters," *Journal of Propulsion and Power,* Vol. 33, No. 4, 2017, pp. 870-880.

[28] Glascock, M. S., "Characterization of Electric Solid Propellant Pulsed Microthrusters," M.S. Thesis, Missouri University of Science and Technology, 2016.

[29] Wilson, M. J., Bushman, S., and Burton, R. L., "A Compact Thrust Stand for Pulsed Plasma Thrusters," *25th International Electric Propulsion Conference*, ERPS Paper IEPC-97-122, Cleveland, OH, 1997.

[30] Polk, J. E., Pancotti, A., Haag, T., King, S., Walker, M. L. R., Blakely, J., and Ziemer, J., "Recommended Practice for Thrust Measurement in Electric Propulsion Testing," *Journal of Propulsion and Power,* Vol. 33, No. 3, 2017, pp. 539-555.

[31] Glascock, M. S., Rovey, J. L., and Polzin, K. A., "Impulse Measurements of Electric Solid Propellant in an Electrothermal Ablation-Fed Pulsed Plasma Thruster," *2019 Joint Propulsion Conference*, AIAA Paper 2019, Indianapolis, IN, 2019.

SECTION

3. CONCLUSIONS AND RECOMMENDATIONS

3.1. CONCLUSIONS

HIPEP appears to behave similarly and offers similar impulse bit compared to PTFE in an APPT, but ablates more mass leading to reduced specific impulse. At high temperatures and over long (~ms) time-scales, it is known that HIPEP undergoes a thermal decomposition process, while PTFE evaporates after depolymerization. However, APPT arcs occur on much shorter timescales, as the discharge current has a period of less than 10 μs. A fundamental ablation-fed arc study showed that HIPEP ablates over twice the specific ablation (mass loss per pulse per energy per pulse) of PTFE. This difference is due to the fundamental thermochemistry of the HIPEP and consitutent species. An APPT performance investigation found that the impulse bit (impulse-per-pulse) of a HIPEP-fueled coaxial APPT laboratory thruster is 100±20 μN-s with 5 J initially stored energy. This impulse bit increased linearly with stored energy by about 30 μN-s/J up to 575±20 μN-s at 20 J. Tests with PTFE showed little change (<10%) in impulse bit between propellants, but a significant reduction of specific impulse. Using the same device, HIPEP specific impulse was measured to be 225 s, which was only 50% of PTFE specific impulse. This performance reduction is due to the previously observed doubled specific ablation of HIPEP. Water absorbed by the hygroscopic HIPEP greatly affects these mass loss and specific impulse measurements. In early pulses, this absorbed water is rapidly evaporated by the arc discharge and the mass loss is exceptionally high, leading to artificially reduced specific impulse. However, even after the additionally absorbed water mass evaporates, the specific impulse reaches a maximum value of only 300 s compared to 450 s for PTFE. This suggests that the fundamental thermochemistry of HIPEP restricts the specific impulse achievable in an APPT to about 2/3 of that possible with the state-of-the-art propellant. However, because the material is shown to operate on the same ablation principles that have been established for PTFE, performance enhancements historically applied to PTFE APPTs should be applied to future HIPEP APPTs with confidence.

3.2. RECOMMENDATIONS

While HIPEP offers similar impulse bit compared to PTFE, the reduced specific impulse and engineering problems caused by its hygroscopic nature severely detract from its application to the APPT alone. Fortunately, HIPEP has the potential for application to multimode propulsion which is not possible using PTFE propellant. The system flexibility and adaptability offered by multimode propulsion may in itself be adequate justification for continued development of a HIPEP-fueled multimode device. Further, research has shown that a multimode system can offer propellant mass savings over a system using separate propellants even if the performance in each mode is reduced [15]. The currently demonstrated performance of HIPEP in the electric (APPT) mode is 300 s compared to 200 s in the chemical (solid rocket motor, SRM) mode. This small gap is not likely to offer enough advantage in a multimode system to justify the added complexity compared to simply selecting one mode or the other. It would seem then, that there are two potential avenues for future research on the HIPEP material. The first focuses on further improving the performance of HIPEP in the APPT mode by thruster improvements and demonstrating electric mode performance that is sufficiently high. The second would focus on alterations in propellant formulation to decrease the ablation mass, and thereby increase performance in electric (potentially both) modes, and address the issues caused by absorption of water.

The above results suggest that the same methods shown in literature to increase specific impulse of PTFE-fueled APPTs would also increase specific impulse in HIPEP APPTs. While coaxial APPTs typically possess lower specific impulse compared to rectangular geometry thrusters, specific impulses in the range of 600-700 s have been measured in a coaxial APPT in the literature [16, 17]. The EPTX device presented in Papers III and IV of this dissertation perhaps more closely resembles the ablative z-pinch pulsed plasma thruster (AZPPT) investigated using PTFE propellant [18]. Some configurations of the AZPPT were measured to have specific impulse over 600 s. Assuming these devices were to operate like the EPTX has been shown to operate, the specific impulse performance of HIPEP in these devices could be expected to be ~450 s. Nominally, an SRM+APPT multimode system with HIPEP propellant could then feasibly achieve 200 s in the SRM chemical mode and 450 s in the APPT electric mode. For orbit-raising maneuvers utilizing multimode propulsion, an optimum electric mode specific impulse can be found for maximum payload mass delivered per day of flight time. This optimum electric mode specifc impulse is always at least a factor of two greater than the chemical mode specific impulse [19, 20]. The HIPEP SRM+APPT multimode concept nominally meets this criteria for propellant mass savings for orbit-raising maneuvers and thus merits further investigation.

In the ablation mass quantification of HIPEP relative to PTFE, two major factors in the increased HIPEP ablation were identified. The first is the inherent thermochemistry of HIPEP and, specifically, the thermal decomposition temperature. HIPEP decomposes and evolves vapor at 470 K compared to the 600 K evaporation temperature of PTFE. It is conceivable that an altered propellant formulation may be able to increase the decomposition temperature of HIPEP. However, it is not currently known what effect this could have on the pyroelectric (and thus chemical mode) behavior. The second factor in increased HIPEP ablation was the absorption of water from the atmosphere. Removal of absorbed water would increase APPT performance, but may also adversely affect propellant stability. However, at long test durations, the impact of the absorbed water on overall performance was basically negligible. Further, the propellant has been flown in space previously by taking measures to seal the material from water absorption before launch. From an engineering persepective, it may be most practical to simply accept the minor performance hit incurred by small amounts of water absorbed rather than try to remove water from the propellant completely.

BIBLIOGRAPHY

[1] Burton, R. L., and Turchi, P. J., "Pulsed Plasma Thruster," *Journal of Propulsion and Power,* Vol. 14, No. 5, 1998, pp. 716-735.

[2] Gatsonis, N. A., Lu, Y., Blandino, J., Demetriou, M. A., and Paschalidis, N., "Micropulsed Plasma Thrusters for Attitude Control of a Low-Earth-Orbiting Cubesat," *Journal of Spacecraft and Rockets,* Vol. 53, No. 1, 2016, pp. 57-73.

[3] Keidar, M., Zhuang, T., Shashurin, A., Teel, G., Chiu, D., Lukas, J., Haque, S., and Brieda, L., "Electric Propulsion for Small Satellites," *Plasma Physics and Controlled Fusion,* Vol. 57, No. 1, 2015, pp. 1-10.

[4] Sawka, W. N., and McPherson, M., "Electrical Solid Propellants: A Safe, Micro to Macro Propulsion Technology," *49th Joint Propulsion Conference*, AIAA, San Jose, CA, 2013.

[5] Sawka, W. N., U.S. Patent for a "Controllable Digital Solid State Cluster Thrusters for Rocket Propulsion and Gas Generation," No. 7958823 B2 and 8464640; June 14, 2011 and June 18, 2013.

[6] Dulligan, M., U.S. Patent for a "Electrically Controlled Extinguishable Solid Propellant Motors," No. 7788900B2; September 7, 2010.

[7] Chung, K., Rozumov, E., Kaminsky, D., Buescher, T., Manship, T., Valdivia, A., Cook, P., and Anderson, P., "Development of Electrically Controlled Energetic Materials," *ECS Transactions,* Vol. 50, No. 40, 2013, pp. 59-66.

[8] Grix, C., and Sawka, W. N., U.S. Patent for a "Family of Modifiable High Performance Electrically Controlled Propellants and Explosives," No. 8888935B2; November 18, 2011.

[9] Sawka, W. N., and Grix, C., U.S. Patent for a "Family of Metastable Intermolecular Composites Utilizing Energetic Liquid Oxidizers with Nanoparticle Fuels in Sol-Gel Polymer Network," No. 8317953B2; November 27.

[10] Rovey, J. L., Lyne, C. T., Mundahl, A. J., Rasmont, N., Glascock, M. S., Wainwright, M. J., and Berg, S. P., "Review of Chemical-Electric Multimode Space Propulsion," *2019 Joint Propulsion Conference*, AIAA, Indianapolis, IN, 2019.

[11] Baird, J. K., Lang, J. R., Hiatt, A. T., and Frederick, R. A., "Electrolytic Combustion in the Polyvinyl Alcohol Plus Hydroxylammonium Nitrate Solid Propellant," *Journal of Propulsion and Power,* Vol. 33, No. 6, 2017, pp. 1589-1590.

[12] Hiatt, A. T., and Frederick, R. A., "Laboratory Experimentation and Basic Research Investigation Electric Solid Propellant Electrolytic Characteristics," *52nd AIAA/SAE/ASEE Joint Propulsion Conference*, AIAA, Salt Lake City, UT, 2016.

[13] Sawka, W. N., and Grix, C., U.S. Patent for a "Electrode Ignition and Control of Electrically Ignitable Materials," No. 8857338B2; October 14.

[14] Digital Solid State Propulsion, L., "Mpm-7 Datasheet," https://dssptech.com/propellant-products.

[15] Donius, B. R., and Rovey, J. L., "Ionic Liquid Dual-Mode Spacecraft Propulsion Assessment," *Journal of Spacecraft and Rockets,* Vol. 48, No. 1, 2011, pp. 110-123.

[16] Burton, R., and Bushman, S., "Probe Measurements in a Coaxial Gasdynamic Ppt," *35th AIAA/ASME/SAE/ASEE Joint Propulsion Conference*, AIAA, Los Angeles, CA, 1999.

[17] Wilson, M. J., Bushman, S., and Burton, R. L., "A Compact Thrust Stand for Pulsed Plasma Thrusters," *25th International Electric Propulsion Conference*, ERPS, Cleveland, OH, 1997.

[18] Markusic, T. E., Polzin, K. A., Choueiri, E. Y., Keidar, M., Boyd, I. D., and Lepsetz, N., "Ablative Z-Pinch Pulsed Plasma Thruster," *Journal of Propulsion and Power,* Vol. 21, No. 3, 2005, pp. 392-400.

[19] Berg, S. P., and Rovey, J. L., "Assessment of Multimode Spacecraft Micropropulsion Systems," *Journal of Spacecraft and Rockets,* Vol. 54, No. 3, 2017, pp. 592-601.

[20] Oh, D. Y., Randolph, T., Kimbrel, S., and Martinez-Sanchez, M., "End-to-End Optimization of Chemical-Electric Orbit-Raising Missions," *Journal of Spacecraft and Rockets,* Vol. 41, No. 5, 2004, pp. 831-839.

VITA

Matthew Scott Glascock grew up in the little-known town of West Plains, Missouri, just 90 miles down the road from Missouri University of Science and Technology. He graduated from the high school there (that's right, a Zizzer) in 2010. That summer, he attended a brief camp at Missouri University of Science and Technology, beginning a fruitful and enjoyable nine year tenure. He graduated Magna Cum Laude with a Bachelor of Science in Aerospace Engineering in May 2014. Shortly thereafter, he continued into graduate school and was awarded a Master of Science in Aerospace Engineering in December 2016.

For many years prior, he desired to see the research through to completion of a Ph.D. degree in Aerospace Engineering. He completed this dissertation in the summer of 2019 and received his Ph.D. in Aerospace Engineering in December of 2019 from Missouri University of Science and Technology. After graduation, Matt continued working in the field of spacecraft propulsion by working for Froberg Aerospace, a startup in Champaign, IL.